Published for SISSA by Springer

Received: October 20, 2025
Accepted: December 17, 2025
Published: February 23, 2026

Entanglement Hamiltonian for the massless Dirac field on a segment with an inhomogeneous background

Erik Tonni[a] **and Stefano Trezzi**[b]

[a] *SISSA and INFN Sezione di Trieste, via Bonomea 265, 34136, Trieste, Italy*
[b] *Departament de Física Quàntica i Astrofísica, Institut de Ciències del Cosmos, Universitat de Barcelona, Martí i Franquès 1, E-08028 Barcelona, Spain*

E-mail: etonni@sissa.it, strezzi@icc.ub.edu

Abstract: We study the entanglement Hamiltonian of an interval for the free massless Dirac field in an inhomogeneous background on a finite segment and in the ground state. We consider a class of metrics that are Weyl equivalent to the flat metric through a Weyl factor that depends only on the spatial coordinate, with the same boundary condition imposed at both endpoints of the segment. The explicit form of the entanglement Hamiltonian is written as the sum of a local and a bilocal term. The weight function of the local term allows us to study a contour function for the entanglement entropies. For the model obtained from the continuum limit of the rainbow chain, the analytic expressions are compared with exact numerical results from the lattice, showing an excellent agreement.

Keywords: Boundary Quantum Field Theory, Field Theories in Lower Dimensions, Lattice Quantum Field Theory, Scale and Conformal Symmetries

ArXiv ePrint: 2509.22182

https://doi.org/10.1007/JHEP02(2026)224

Contents

1 Introduction **1**

2 Entanglement Hamiltonian of an interval in a segment **3**

3 Entanglement Hamiltonian in inhomogeneous backgrounds **12**

3.1 Generic background 12

3.2 Rainbow model 18

4 Entanglement Hamiltonian of a block in the rainbow chain **24**

5 Conclusions **39**

1 Introduction

The geometric bipartite entanglement between complementary spatial regions can be explored through the corresponding reduced density matrices or, equivalently, the corresponding entanglement Hamiltonians, which provide the modular Hamiltonian of the bipartition [1–3]. Consider a quantum system in a state characterised by its density matrix ρ and a geometric bipartition of its space identified by a region A and its complement B. By assuming that the Hilbert space $\mathcal{H}$ can be factorised accordingly, namely as $\mathcal{H} = \mathcal{H}_A \otimes \mathcal{H}_B$, the reduced density matrices of A and B are defined as $\rho_A \equiv \mathrm{Tr}_{\mathcal{H}_B}\rho$ and $\rho_B \equiv \mathrm{Tr}_{\mathcal{H}_A}\rho$ respectively, with the normalisation condition $\mathrm{Tr}_{\mathcal{H}_A}\rho_A = \mathrm{Tr}_{\mathcal{H}_B}\rho_B = 1$. Since ρ_A is hermitian and positive semidefinite, when the zero eigenvalue is not in its spectrum it can be written as $\rho_A \propto \mathrm{e}^{-K_A}$, where the hermitian operator K_A is the entanglement Hamiltonian of the region A. The spectrum of ρ_A, which is known as the entanglement spectrum, provides important quantities like the Rényi entropies $S_A^{(n)} \equiv \frac{1}{1-n}\log[\mathrm{Tr}_{\mathcal{H}_A}\rho_A^n]$, labelled by the integer $n \geqslant 2$ (the Rényi index), and the entanglement entropy $S_A \equiv -\mathrm{Tr}_{\mathcal{H}_A}(\rho_A \log \rho_A)$. The entanglement entropy can be obtained also from the Rényi entropies through the replica limit, i.e. the analytic continuation $S_A = \lim_{n\to 1} S_A^{(n)}$; hence these quantities are often called entanglement entropies. When ρ is a pure state, we have that $S_A^{(n)} = S_B^{(n)}$ and $S_A = S_B$. The entanglement Hamiltonian contains more information than the quantities obtained purely from the entanglement spectrum.

In quantum field theories, the analytic expression of the entanglement Hamiltonian in terms of the fundamental fields is known in very few cases. In a generic number of spacetime dimensions, these include the seminal result of Bisognano and Wichmann [4, 5], which holds for any relativistic quantum field theory in the vacuum when A is the half space $x > 0$, and states that K_A is proportional to the generator of the boosts in the x-direction. Focusing on a conformal field theory (CFT) in the vacuum, this fundamental result and the proper conformal map provide K_A when A is a spherical region [6, 7]. In a two-dimensional CFT, where the conformal symmetry is infinite dimensional, other explicit expressions can be found when A is an interval [8, 9]. A universal result for K_A is also known when the CFT is defined either on the half line with a conformally invariant boundary condition or on the segment with the same conformally invariant boundary condition imposed at both boundaries, hence the model is a boundary conformal field theory (BCFT), when A is an interval adjacent to

JHEP02(2026)224

Figure 1. Bipartition of the segment given by an interval A (red region) in a generic position. The same boundary condition is imposed at both endpoints of the segment.

the boundary [9, 10]. In these cases, the entanglement Hamiltonian K_A is a local operator. In particular, K_A is written as the integral over A of the energy density multiplied by a weight function that depends on the global geometry of the space, on the endpoints of A and on the state of the entire system. In this BCFT setup, K_A for an interval A adjacent to the boundary has been written explicitly also for a specific class of spatially inhomogeneous backgrounds where the background metric is Weyl equivalent to the flat metric through a Weyl factor that depends only on the spatial coordinate and is even about the centre of the segment [10]. When the underlying BCFT model is the free massless Dirac field, whose central charge is $c = 1$, this class of spatially inhomogeneous backgrounds has interesting applications. Indeed, it captures the continuum limit of the low energy excitations of some free fermionic systems around a varying energy scale. Some interesting examples of such models are the rainbow chain [11–15], the free Fermi gas in a harmonic trap [16–20] and an XXZ chain with a gradient [21]. Furthermore, these inhomogeneous backgrounds are also related to optical metrics [22–25], arising in the study of light propagation through media with a spatially varying refractive index. In this manuscript, the numerical checks are performed in the rainbow chain, where a volume law for the entanglement entropy is observed in the regime of large inhomogeneity for certain bipartitions.

A qualitatively different class of entanglement Hamiltonians is provided by the cases where K_A contains local and bilocal operators. All the examples where analytic expressions are known involve the massless Dirac field, and all of them are inspired by the case where A is the union of an arbitrary finite number of disjoint intervals in the line and the massless Dirac field is in its ground state [26]. In this class, we also find K_A of an interval A when the massless Dirac field is at finite temperature and on a circle [27, 28]. As for cases where the underlying model is not invariant under translations, it is worth mentioning K_A for the massless Dirac field in its ground state when A is either an interval in the half line [29] or the union of two equal intervals in the line at the same distance from a pointlike defect [30].

The main result of this manuscript is another example where K_A for the massless Dirac field is known analytically and it is made by a local and a bilocal term. We consider the BCFT model defined by the massless Dirac field in the segment where the same conformally invariant boundary condition is imposed at both endpoints. In the case where the whole system is in the ground state, we find the entanglement Hamiltonian K_A of an interval A in a generic position in the segment, not adjacent to the boundary (see figure 1, where A corresponds to the red region), for the class of spatially inhomogeneous backgrounds mentioned above.

Another quantity that we find worth investigating is the contour function for the entanglement entropies [31, 32]. This scalar function is a spatial density for the entanglement entropies constrained by additional requirements guaranteeing a proper behaviour of this quantity under

JHEP02(2026)224

local unitary transformations, subregion inclusions and possible symmetries [32]. Although the contour function for the entanglement entropies does not provide a complete characterisation of the bipartite entanglement like the entanglement Hamiltonian, it contains more information than the entanglement spectrum because its definition involves also the eigenvectors of K_A. In homogeneous CFT, some contour functions for the entanglement entropies have been written through the weight function of the local term in the corresponding entanglement Hamiltonian [8, 9, 32, 33]. In the inhomogeneous BCFT mentioned above, this observation has been applied to the bipartition in figure 1 when A is adjacent to the boundary [10].

In this manuscript, for the ground state of the inhomogeneous BCFT given by the massless Dirac field on the segment and the bipartition shown in figure 1, we study the contour function for the entanglement entropies provided by the weight function of the local term in the entanglement Hamiltonian. The entanglement entropies of A are computed by integrating this contour function, recovering the result of [15] obtained through the twist fields method [34].

A comparison with the exact numerical results obtained in a lattice model is performed for the rainbow chain. The rainbow chain [11] is an inhomogeneous free fermionic chain in a finite segment whose hopping coefficients depend on a single real and positive parameter in such a way that, for certain bipartitions, the entanglement entropy of a block obeys the volume law in the regime of large inhomogeneity [12–15]. The continuum limit of the rainbow chain provides the rainbow model in the continuum. The entanglement Hamiltonian in the rainbow chain and its continuum limit are investigated by employing the Peschel formula [3, 35] and the continuum limit procedure discussed in [36–39]. Our analysis is different from the numerical study performed in [10] for a block A adjacent to an endpoint of the segment, where only the local term occurs. The entanglement entropies and their contour functions in the rainbow chain for the bipartition in figure 1 are also explored. The analytic predictions in the continuum are obtained by specialising the aforementioned BCFT results for the entanglement Hamiltonian and the contour function for the entanglement entropies to the case of the rainbow model.

The outline of the paper is as follows. In section 2, focusing on the homogeneous background, we construct the entanglement Hamiltonian of the interval A and the corresponding contour function for the entanglement entropies. In section 3, these quantities are investigated in the specific class of spatially inhomogeneous backgrounds of interest. Within this class, the explicit expressions for the special case of the rainbow model are reported (see section 3.2). The rainbow chain is explored in section 4, where a continuum limit procedure is applied to the entanglement Hamiltonian of a block of contiguous sites and to the contour function for the entanglement entropies, finding a remarkable agreement with the corresponding analytic expressions in the rainbow model. Conclusions are drawn in section 5, where possible directions for future studies are also mentioned.

2 Entanglement Hamiltonian of an interval in a segment

In this section we discuss the entanglement Hamiltonian K_A of an interval A for the free massless Dirac field on a segment with the same boundary condition imposed at both its endpoints, when A is not adjacent to the boundary (see figure 1).

JHEP02(2026)224

The free massless Dirac field ψ on the infinite strip $\mathbb{S} \equiv [-L, L] \times \mathbb{R}$ of width $2L$, parameterised by the complex coordinate $z = x + \mathrm{i}t_{\mathrm{E}}$ (the Euclidean time $t_{\mathrm{E}} \in \mathbb{R}$ is related to the Lorentzian time t by $t = -\mathrm{i}t_{\mathrm{E}}$) with $x \in [-L, L]$, is described by the following two-dimensional Euclidean action

$$S[\psi] \propto \int_{\mathbb{S}} \left(\psi_2^* \overleftrightarrow{\partial_{\bar{z}}} \psi_2 + \psi_1^* \overleftrightarrow{\partial_z} \psi_1 \right) \mathrm{d}z \, \mathrm{d}\bar{z} \tag{2.1}$$

where ψ_1 and ψ_2 denote the left and right chiral components of the Dirac field, which become the antiholomorphic and holomorphic components of the field in Euclidean signature, respectively. We focus on the case where the same boundary condition is imposed at both boundaries of the strip $\mathbb{S}$. This model is a BCFT with central charge $c = 1$.

Since this model is a BCFT, it is convenient to introduce a conformal map sending the strip $\mathbb{S}$ onto the right half plane $\mathbb{H}_{\mathrm{R}}$, parameterised by the complex coordinate $\hat{z} = \hat{x} + \mathrm{i}\hat{t}_{\mathrm{E}}$, with $\hat{x} \geqslant 0$ and $\hat{t}_{\mathrm{E}} \in \mathbb{R}$. The boundary conditions on $\mathbb{S}$ are obtained from the one imposed at the boundary of $\mathbb{H}_{\mathrm{R}}$. The conformal map that will be employed in our analysis also depends on the bipartition of the segment $[-L, L]$, which is determined by an interval in a generic position, and will be discussed below (see (2.11)).

Considering the massless Dirac field $\hat{\psi}$ on the half line parameterised by the real coordinate $\hat{x} \geqslant 0$, the vanishing of the energy flow through the boundary is imposed to guarantee the global energy conservation [40–42], and this condition is satisfied for either

$$\hat{\lambda}_1\big|_{\hat{x}=0} = \mathrm{e}^{\mathrm{i}\alpha_{\mathrm{v}}} \, \hat{\lambda}_2\big|_{\hat{x}=0} \qquad\qquad \alpha_{\mathrm{v}} \in [0, 2\pi) \tag{2.2}$$

or

$$\hat{\chi}_1\big|_{\hat{x}=0} = \mathrm{e}^{-\mathrm{i}\alpha_{\mathrm{a}}} \, \hat{\chi}_2^*\big|_{\hat{x}=0} \qquad\qquad \alpha_{\mathrm{a}} \in [0, 2\pi) \tag{2.3}$$

for any value of $\hat{t}_{\mathrm{E}} \in \mathbb{R}$, where the components of the Dirac field have been denoted by $\hat{\lambda}_j$ and $\hat{\chi}_j$ to distinguish the two cases. The boundary conditions (2.2) or (2.3) provide two different models that are called the vector phase and the axial phase respectively. Indeed, at quantum level, either the charge or the helicity is conserved [43]. In particular, the charge is conserved in the vector phase, while the helicity is conserved in the axial phase.

In order to shorten the forthcoming expressions, following [29], we find it convenient to treat the boundary conditions (2.2) and (2.3) in a unified way. This is done by introducing the antiholomorphic field $\hat{\psi}_1$ and the holomorphic field $\hat{\psi}_2$, which correspond to $\hat{\lambda}_1$ and $\hat{\lambda}_2$ in the vector phase and to $\hat{\chi}_1^*$ and $\hat{\chi}_2$ in the axial phase, respectively. In terms of the fields $\hat{\psi}_1$ and $\hat{\psi}_2$, the boundary conditions (2.2) and (2.3) read

$$\hat{\psi}_1(-\mathrm{i}\hat{t}_{\mathrm{E}}) = \mathrm{e}^{\mathrm{i}\alpha} \, \hat{\psi}_2^*(\mathrm{i}\hat{t}_{\mathrm{E}}) \qquad\qquad \alpha \in [0, 2\pi) \tag{2.4}$$

where $\alpha = \alpha_{\mathrm{v}}$ in the vector phase and $\alpha = \alpha_{\mathrm{a}}$ in the axial phase.

Consider the bipartition of the half line determined by the interval $\hat{A} \equiv [\,\hat{a}, \hat{b}\,]$, which is not adjacent to the boundary for $\hat{a} > 0$. When the massless Dirac field is in its ground state, the entanglement Hamiltonian of this bipartition reads [29]

$$\widehat{K}_{\hat{A}} = 2\pi \int_{\hat{a}}^{\hat{b}} \hat{\beta}_{\mathrm{loc}}(\hat{x}) \, \widehat{\mathcal{E}}(\hat{x}) \, \mathrm{d}\hat{x} + 2\pi \int_{\hat{a}}^{\hat{b}} \hat{\beta}_{\mathrm{biloc}}(\hat{x}) \, \widehat{T}^{(\alpha)}_{\mathrm{biloc}}(\hat{x}, \hat{x}_{\mathrm{c}}) \, \mathrm{d}\hat{x} \tag{2.5}$$

JHEP02(2026)224

where the local operator $\widehat{\mathcal{E}}(\hat{x})$ is the normal ordered version of the energy density on the half line, namely

$$\widehat{\mathcal{E}}(\hat{x}) \equiv \frac{\mathrm{i}}{2} :\Big[\Big((\partial_{\hat{x}}\hat{\psi}_1^*)\,\hat{\psi}_1 - \hat{\psi}_1^*\,(\partial_{\hat{x}}\hat{\psi}_1)\Big)(\hat{x}) - \Big((\partial_{\hat{x}}\hat{\psi}_2^*)\,\hat{\psi}_2 - \hat{\psi}_2^*\,(\partial_{\hat{x}}\hat{\psi}_2)\Big)(\hat{x})\Big]: \tag{2.6}$$

and the bilocal operator is defined as follows

$$\widehat{T}^{(\alpha)}_{\text{biloc}}(\hat{x},\hat{y}) \equiv \frac{\mathrm{i}}{2}\left\{ e^{\mathrm{i}\alpha} :\Big[\,\hat{\psi}_1^*(\hat{y})\,\hat{\psi}_2(\hat{x}) + \hat{\psi}_1^*(\hat{x})\,\hat{\psi}_2(\hat{y})\Big]: - e^{-\mathrm{i}\alpha} :\Big[\,\hat{\psi}_2^*(\hat{y})\,\hat{\psi}_1(\hat{x}) + \hat{\psi}_2^*(\hat{x})\,\hat{\psi}_1(\hat{y})\Big]:\right\}. \tag{2.7}$$

This bilocal operator is evaluated at $\hat{y} = \hat{x}_{\text{c}}$ in (2.5), where $\hat{x}_{\text{c}} \in \hat{A}$ is the point conjugate to $\hat{x}$, given by

$$\hat{x}_{\text{c}}(\hat{x}) \equiv \frac{\hat{a}\,\hat{b}}{\hat{x}}\,. \tag{2.8}$$

In the entanglement Hamiltonian (2.5), the weight function of the local term is

$$\hat{\beta}_{\text{loc}}(\hat{x}) = \frac{(\,\hat{b}^2 - \hat{x}^2\,)(\,\hat{x}^2 - \hat{a}^2\,)}{2(\,\hat{b} - \hat{a}\,)(\hat{a}\,\hat{b} + \hat{x}^2)} \tag{2.9}$$

while the weight function of the bilocal term reads

$$\hat{\beta}_{\text{biloc}}(\hat{x}) = \frac{\hat{\beta}_{\text{loc}}(\hat{x}_{\text{c}})}{\hat{x} + \hat{x}_{\text{c}}} = \frac{\hat{a}\,\hat{b}\,(\,\hat{b}^2 - \hat{x}^2\,)(\,\hat{x}^2 - \hat{a}^2\,)}{2(\,\hat{b} - \hat{a}\,)\,\hat{x}\,(\,\hat{a}\,\hat{b} + \hat{x}^2\,)^2}\,. \tag{2.10}$$

In a neighbourhood of the endpoints of the interval, the expansion of the weight function of the local term in (2.9) is $\hat{\beta}_{\text{loc}}(\hat{x}) = \hat{x} - \hat{a} + O((\hat{x}-\hat{a})^2)$ as $\hat{x} \to \hat{a}$ and $\hat{\beta}_{\text{loc}}(\hat{x}) = \hat{b} - \hat{x} + O((\hat{b}-\hat{x})^2)$ as $\hat{x} \to \hat{b}$, hence $\hat{\beta}_{\text{loc}}(\hat{x})$ satisfies the behaviour expected from the Bisognano-Wichmann result; while the asymptotic behaviours for the weight function of the bilocal term in (2.10) are given by $\hat{\beta}_{\text{biloc}}(\hat{x}) = \frac{\hat{b}}{\hat{a}(\hat{a}+\hat{b})}(\hat{x}-\hat{a}) + O((\hat{x}-\hat{a})^2)$ as $\hat{x} \to \hat{a}$ and $\hat{\beta}_{\text{biloc}}(\hat{x}) = \frac{\hat{a}}{\hat{b}(\hat{a}+\hat{b})}(\hat{b}-\hat{x}) + O((\hat{b}-\hat{x})^2)$ as $\hat{x} \to \hat{b}$.

In terms of the complex coordinates z and $\hat{z}$ parameterising $\mathbb{S}$ and $\mathbb{H}_{\text{R}}$ respectively, we employ the following holomorphic map sending $\mathbb{S}$ onto $\mathbb{H}_{\text{R}}$

$$\hat{w}(z) \equiv \hat{a}\,\frac{\tan\left[\frac{\pi(z+L)}{4L}\right]}{\tan\left[\frac{\pi(a+L)}{4L}\right]} \equiv \frac{\hat{a}}{a_L}\,z_L \tag{2.11}$$

where $\hat{w}(z) \in \mathbb{H}_{\text{R}}$ and the parameter a corresponds to the first endpoint of the interval A in the segment. This map satisfies $\hat{w}(a) = \hat{a}$ with $\hat{a} > 0$, and in the last step it is written through the shorthand notation given by

$$z_L \equiv \tan\left[\frac{\pi(z+L)}{4L}\right] \qquad a_L \equiv \tan\left[\frac{\pi(a+L)}{4L}\right] \qquad b_L \equiv \tan\left[\frac{\pi(b+L)}{4L}\right]. \tag{2.12}$$

The conformal map (2.11) sends the segment having $\text{Im}(z) = 0$ in $\mathbb{S}$ onto the half line having $\text{Im}(\hat{z}) = 0$ in $\mathbb{H}_{\text{R}}$; hence the image of the second endpoint of A is real and reads

$$\hat{b} \equiv \hat{w}(b) = \frac{\hat{a}}{a_L}\,b_L\,. \tag{2.13}$$

JHEP02(2026)224

The inverse and the first derivative of the map in (2.11) are given respectively by

$$z(\hat{w}) = \frac{4L}{\pi} \arctan\left(\frac{a_L}{\hat{a}}\,\hat{w}\right) - L \qquad \hat{w}'(z) = \frac{\hat{a}}{a_L}\,\frac{\pi}{4L\,\left(\cos\left[\frac{\pi(z+L)}{4L}\right]\right)^2}\,. \tag{2.14}$$

Other conformal maps relating a strip and the half plane have been employed e.g. in [9, 10, 15, 44] to explore the bipartite entanglement in critical systems with a boundary.

A vertical line in $\mathbb{S}$ parameterised by $x_0 + \mathrm{i}\,t_{\mathrm{E}} \in \mathbb{S}$ with $x_0 \in [-L, L]$ and $t_{\mathrm{E}} \in \mathbb{R}$, is mapped by (2.11) onto a circular arc whose endpoints are $\hat{z} = \pm\mathrm{i}\,\hat{w}(0)$, where $\hat{w}(0) = \hat{a}/a_L$ is positive. The circle supporting this arc is given by $(\hat{x} - C_0)^2 + \hat{t}_{\mathrm{E}}^2 = R_0^2$ with $\hat{x} \geqslant 0$ and

$$C_0 \equiv \frac{\hat{w}(x_0)^2 - \hat{w}(0)^2}{2\,\hat{w}(0)} \qquad R_0 \equiv \frac{\hat{w}(x_0)^2 + \hat{w}(0)^2}{2\,\hat{w}(0)}\,. \tag{2.15}$$

In particular, the central vertical line corresponding to x_0 is mapped onto the half circle in $\mathbb{H}_{\mathrm{R}}$ centred at the origin $\hat{z} = 0$ with radius equal to $\hat{w}(0)$. As a further consequence, the left and right boundaries of $\mathbb{S}$, corresponding to $x_0 = -L$ and $x_0 = L$ respectively, are mapped onto the vertical segment given by $\hat{z} = \mathrm{i}\,\hat{t}_{\mathrm{E}}$ with $-\hat{w}(0) < \hat{t}_{\mathrm{E}} < \hat{w}(0)$ and onto its complement on the boundary of $\mathbb{H}_{\mathrm{R}}$, respectively. Another property of the conformal map (2.11) is that the image of a horizontal segment in the strip $\mathbb{S}$ made by the points $x + \mathrm{i}\,\hat{t}_{\mathrm{E},0}$ is the half circle $\hat{x}^2 + (\hat{t}_{\mathrm{E}} - C_1)^2 = R_1^2$ centred on the boundary of $\mathbb{H}_{\mathrm{R}}$, where

$$C_1 \equiv \frac{\hat{w}(L + \mathrm{i}\,\hat{t}_{\mathrm{E},0}) + \hat{w}(-L + \mathrm{i}\,\hat{t}_{\mathrm{E},0})}{2} \qquad R_1 \equiv \frac{\left|\hat{w}(L + \mathrm{i}\,\hat{t}_{\mathrm{E},0}) - \hat{w}(-L + \mathrm{i}\,\hat{t}_{\mathrm{E},0})\right|}{2}\,. \tag{2.16}$$

The conformal map (2.11) and the boundary condition (2.2) or (2.3) imposed at the boundary of $\mathbb{H}_{\mathrm{R}}$ provide the boundary conditions at the boundaries of $\mathbb{S}$. In particular, from the second expression in (2.14), we find

$$\hat{w}'(z)^{-1/2}\Big|_{z=-L+\mathrm{i}t_{\mathrm{E}}} = \sqrt{\frac{4L\,a_L}{\pi\,\hat{a}}}\,\cosh\left(\frac{\pi\,t_{\mathrm{E}}}{4L}\right) \qquad \bar{\hat{w}}'(\bar{z})^{-1/2}\Big|_{\bar{z}=-L-\mathrm{i}t_{\mathrm{E}}} = \sqrt{\frac{4L\,a_L}{\pi\,\hat{a}}}\,\cosh\left(\frac{\pi\,t_{\mathrm{E}}}{4L}\right) \tag{2.17}$$

and

$$\hat{w}'(z)^{-1/2}\Big|_{z=L+\mathrm{i}t_{\mathrm{E}}} = -\mathrm{i}\sqrt{\frac{4L\,a_L}{\pi\,\hat{a}}}\,\sinh\left(\frac{\pi\,t_{\mathrm{E}}}{4L}\right) \qquad \bar{\hat{w}}'(\bar{z})^{-1/2}\Big|_{\bar{z}=L-\mathrm{i}t_{\mathrm{E}}} = \mathrm{i}\sqrt{\frac{4L\,a_L}{\pi\,\hat{a}}}\,\sinh\left(\frac{\pi\,t_{\mathrm{E}}}{4L}\right) \tag{2.18}$$

which are real and purely imaginary, respectively. Since the conformal weights of the antiholomorphic field ψ_1 and of the holomorphic field ψ_2 are $(0, \frac{1}{2})$ and $(\frac{1}{2}, 0)$ respectively [45, 46], under the holomorphic map $z \mapsto \hat{w}(z)$ they transform as $\hat{\psi}_1(\bar{\hat{w}}) = \bar{\hat{w}}'(\bar{z})^{-1/2}\,\psi_1(\bar{z})$ and $\hat{\psi}_2(\hat{w}) = \hat{w}'(z)^{-1/2}\,\psi_2(z)$. By combining these transformations with (2.17) and (2.18), the boundary conditions (2.2) and (2.3) are mapped respectively into

$$\lambda_1(-L - \mathrm{i}\,t_{\mathrm{E}}) = \mathrm{e}^{\mathrm{i}\alpha_{\mathrm{v}}}\,\lambda_2(-L + \mathrm{i}\,t_{\mathrm{E}}) \qquad \lambda_1(L - \mathrm{i}\,t_{\mathrm{E}}) = -\mathrm{e}^{\mathrm{i}\alpha_{\mathrm{v}}}\,\lambda_2(L + \mathrm{i}\,t_{\mathrm{E}}) \tag{2.19}$$

in the vector phase and into

$$\chi_1(-L - \mathrm{i}\,t_{\mathrm{E}}) = \mathrm{e}^{-\mathrm{i}\alpha_{\mathrm{a}}}\,\chi_2^*(-L + \mathrm{i}\,t_{\mathrm{E}}) \qquad \chi_1(L - \mathrm{i}\,t_{\mathrm{E}}) = \mathrm{e}^{-\mathrm{i}\alpha_{\mathrm{a}}}\,\chi_2^*(L + \mathrm{i}\,t_{\mathrm{E}}) \tag{2.20}$$

JHEP02(2026)224

in the axial phase, for any $t_{\rm E} \in \mathbb{R}$. Although different signs occur in the two r.h.s.'s of (2.19), associated with the two boundaries of the strip, the two conditions in (2.19) are obtained from a single boundary condition characterising the vector phase in $\mathbb{H}_{\rm R}$, and in this sense they correspond to the same boundary condition imposed at both boundaries of $\mathbb{S}$.

The entanglement Hamiltonian K_A of the interval $A \equiv [a,b]$ in the segment $[-L,L]$ for the massless Dirac field with the same boundary condition imposed at both endpoints of the segment, given by either (2.19) or (2.20), is obtained from the entanglement Hamiltonian of the massless Dirac field on the half line (see (2.5)) and the transformation law of the fields involved in its expression. This gives

$$K_A = 2\pi \int_a^b \beta_{\rm loc}(x)\, \mathcal{E}(x)\, {\rm d}x + 2\pi \int_a^b \beta_{\rm biloc}(x)\, T^{(\alpha)}_{\rm biloc}(x, x_{\rm c})\, {\rm d}x \tag{2.21}$$

where the operators $\mathcal{E}(x)$ and $T^{(\alpha)}_{\rm biloc}(x,y)$ are defined respectively as (2.6) and (2.7) with the hatted fields replaced by the corresponding ones on the strip (without the hat, in our notation).

The weight function of the local term in (2.21) is obtained from the local term in the modular Hamiltonian (2.5) by employing the fact that the conformal dimension of the energy-momentum tensor is equal to 2. Thus, from (2.9) and (2.11), for this weight function we find

$$\beta_{\rm loc}(x) \equiv \frac{\hat\beta_{\mathbb{S},{\rm loc}}(\hat w(x))}{\hat w'(x)} = \frac{4L}{\pi}\Big[\cos\Big(\frac{\pi(x+L)}{4L}\Big)\Big]^2 \frac{(b_L^2 - x_L^2)(x_L^2 - a_L^2)}{2(b_L - a_L)(a_L\, b_L + x_L^2)} \tag{2.22}$$

where $\hat\beta_{\mathbb{S},{\rm loc}}(\hat x)$ is defined as $\hat\beta_{\rm loc}(\hat x)$ in (2.9) with $\hat b$ and $\hat a$ replaced by $\hat w(b)$ and $\hat w(a)$ respectively. In fact, $\hat\beta_{\mathbb{S},{\rm loc}}(\hat x) = \hat\beta_{\rm loc}(\hat x)$ because $\hat w(a) = \hat a$ and $\hat w(b) = \hat b$, from (2.11) and (2.13) respectively. In the last expression of (2.22), the notation introduced in (2.12) has been employed. The weight function (2.22) can be written more explicitly as follows

$$\beta_{\rm loc}(x) = \frac{2L}{\pi}\, \frac{\big[\sin\big(\frac{\pi b}{2L}\big) - \sin\big(\frac{\pi x}{2L}\big)\big]\,\big[\sin\big(\frac{\pi x}{2L}\big) - \sin\big(\frac{\pi a}{2L}\big)\big]}{\sin\big(\frac{\pi(b-a)}{2L}\big) + \big[\cos\big(\frac{\pi b}{2L}\big) - \cos\big(\frac{\pi a}{2L}\big)\big]\,\sin\big(\frac{\pi x}{2L}\big)}\,. \tag{2.23}$$

We remark that $\beta_{\rm loc}(a) = \beta_{\rm loc}(b) = 0$. The asymptotic behaviour of (2.22)–(2.23) close to the endpoints of A is the one expected from the Bisognano-Wichmann result, namely

$$\begin{aligned} &\beta_{\rm loc}(x) = (x-a) + O((x-a)^2) \qquad && x \to a \\ &\beta_{\rm loc}(x) = -(x-b) + O((x-b)^2) \qquad && x \to b\,. \end{aligned} \tag{2.24}$$

We find it worth anticipating here that in section 4 the weight function in (2.22)–(2.23) is obtained from exact numerical results for a homogeneous free fermionic chain in the segment through a continuum limit procedure (see the solid blue curves in figure 6 and in the top panels of figure 11).

It is instructive to consider some limiting regimes of the weight function in (2.22)–(2.23).

The limiting case where the interval is adjacent to the boundary is recovered by taking e.g. $b \to L$ in (2.22)–(2.23), finding the result of [10]

$$\lim_{b\to L} \beta_{\rm loc}(x) = \frac{2L}{\pi}\, \frac{\sin\big[\pi x/(2L)\big] - \sin\big[\pi a/(2L)\big]}{\cos\big[\pi a/(2L)\big]}\,. \tag{2.25}$$

JHEP02(2026)224

The well known parabolic profile occurring in the entanglement Hamiltonian of the interval in the infinite line [6, 7] is obtained in the limit $L \to +\infty$. Indeed, for (2.22)–(2.23) in this limiting regime we find $\beta_{\rm loc}(x) = \frac{(b-x)(x-a)}{b-a} + O(1/L^2)$.

The case of the interval in the half line studied in [29] can be recovered by first setting $a = \hat{a} - L$, $b = \hat{b} - L$ and $x = \hat{x} - L$ in (2.22)–(2.23) and then taking $L \to +\infty$. This gives $\beta_{\rm loc}(x) = \hat{\beta}_{\rm loc}(\hat{x}) + O(1/L^2)$ as $L \to +\infty$, i.e. the $O(1)$ term is (2.9), as expected.

In order to write the weight function of the bilocal term in (2.21), we have to introduce the point $x_{\rm c}(x) \in A$ conjugate to $x \in A$, which can be obtained from (2.8) through the inverse function $z(\hat{w})$ in (2.14) as follows

$$x_{\rm c}(x) = z(\hat{x}_{\rm c}) = \frac{4L}{\pi} \arctan(a_L\, \hat{b}/\hat{w}(x)) - L = \frac{4L}{\pi} \arctan(a_L\, b_L/x_L) - L \tag{2.26}$$

where it has been used that $\hat{x} = \hat{w}(x) = \hat{a}\, x_L/a_L$, from (2.11) and (2.13). By employing the notation defined in (2.12), the last expression in (2.26) can be written as

$$x_{{\rm c},L}(x) = \frac{a_L\, b_L}{x_L}\,. \tag{2.27}$$

From (2.26), notice that $x_{\rm c}(a) = b$, $x_{\rm c}(b) = a$, and $x_{\rm c}(0) = \frac{4L}{\pi} \arctan(a_L\, b_L) - L$.

There exists a special point $x_{\rm sc} \in A$ which is self-conjugate, meaning that it coincides with its conjugate point. It is determined by the condition $x_{\rm c}(x_{\rm sc}) = x_{\rm sc}$, which can be written by exploiting (2.27), finding

$$x_{{\rm sc},L}^2 = a_L\, b_L \tag{2.28}$$

where $x_{{\rm sc},L} \equiv \tan[\pi(x_{\rm sc} + L)/(4L)]$, according to (2.12). From (2.28), one obtains an explicit expression for the point $x_{\rm sc}$, namely $x_{\rm sc} = \frac{4L}{\pi} \arctan(\sqrt{a_L\, b_L}\,) - L$.

In the symmetric case, the centre of A coincides with the centre of the segment (i.e. $a = -b$ with $0 < b < L$) and, from (2.26) and (2.28), we find that $x_{\rm c}(x) = -x$ and $x_{\rm sc} = 0$ respectively.

The expression (2.26) in the limiting case of the interval in the half line can be explored as done above for $\beta_{\rm loc}(x)$, namely by setting $a = \hat{a} - L$, $b = \hat{b} - L$, $x = \hat{x} - L$ and $x_{\rm c} = \hat{x}_{\rm c} - L$ in (2.26) first, and then sending $L \to +\infty$. This gives $\hat{x}_{\rm c} \to \hat{a}\, \hat{b}/\hat{x}$ in this limit, as expected from the results reported in [29].

Finally, in the special case where A is adjacent to the boundary, namely when either $b \to L$ or $a \to -L$, for (2.26) we find that either $x_{\rm c}(x) \to L$ or $x_{\rm c}(x) \to -L$ respectively, for all $x \in A$.

The weight function of the bilocal term in (2.21) is obtained from the weight function (2.10), by employing the conformal map (2.11) and the fact that the chiral fermion field has conformal dimension equal to 1/2, and reads

$$\beta_{\rm biloc}(x) = \sqrt{\frac{\hat{w}'(x)}{\hat{w}'(x_{\rm c})}}\; \hat{\beta}_{\mathbb{S},{\rm biloc}}(\hat{w}(x)) = \frac{\cos\left[\frac{\pi(x_{\rm c}+L)}{4L}\right]}{\cos\left[\frac{\pi(x+L)}{4L}\right]}\, \frac{a_L\, b_L\, (b_L^2 - x_L^2)\, (x_L^2 - a_L^2)}{2\,(b_L - a_L)\, x_L\, (a_L\, b_L + x_L^2)^2} \tag{2.29}$$

where $\hat{w}'(x)$ is given in (2.14), $x_{\rm c}$ in (2.26) and $\hat{\beta}_{\mathbb{S},{\rm biloc}}(\hat{x})$ is defined as $\hat{\beta}_{\rm biloc}(\hat{x})$ in (2.10) with $\hat{b}$ and $\hat{a}$ replaced by $\hat{w}(b)$ and $\hat{w}(a)$ respectively. Similarly to (2.22), since the map (2.11) satisfies $\hat{w}(a) = \hat{a}$ and $\hat{w}(b) = \hat{b}$, we have that $\hat{\beta}_{\mathbb{S},{\rm biloc}}(\hat{x}) = \hat{\beta}_{\rm biloc}(\hat{x})$. In (2.29) it has been also

JHEP02(2026)224

used that $\frac{\pi(x+L)}{4L} \in (0, \frac{\pi}{2})$ for $x \in (-L, L)$. Notice that, in (2.29), $\hat{w}'(x)^{1/2}$ occurs because also the transformation of the volume element of the integral must be taken into account to get the bilocal term in (2.21). From (2.26) and (2.12), we observe that

$$\cos\left[\frac{\pi(x_{\rm c}+L)}{4L}\right] = \frac{x_L}{\sqrt{a_L^2\, b_L^2 + x_L^2}} \tag{2.30}$$

which leads us to write (2.29) in terms of the notation introduced in (2.12) as follows

$$\beta_{\rm biloc}(x) = \frac{a_L\, b_L\, (b_L^2 - x_L^2)(x_L^2 - a_L^2)}{2(b_L - a_L)\, \cos\left[\frac{\pi(x+L)}{4L}\right] \sqrt{a_L^2\, b_L^2 + x_L^2}\, (a_L\, b_L + x_L^2)^2}\,. \tag{2.31}$$

A more explicit form for the weight function given in (2.29) or (2.31) reads

$$\begin{aligned}\beta_{\rm biloc}(x) = {} & \frac{1}{\sqrt{\tan^2\left[\frac{\pi(a+L)}{4L}\right]\tan^2\left[\frac{\pi(b+L)}{4L}\right] + \tan^2\left[\frac{\pi(x+L)}{4L}\right]}}\, \frac{\tan\left[\frac{\pi(a+L)}{4L}\right]\tan\left[\frac{\pi(b+L)}{4L}\right]}{2\left(\tan\left[\frac{\pi(b+L)}{4L}\right] - \tan\left[\frac{\pi(a+L)}{4L}\right]\right)} \\ & \times \frac{\left(\tan^2\left[\frac{\pi(b+L)}{4L}\right] - \tan^2\left[\frac{\pi(x+L)}{4L}\right]\right)\left(\tan^2\left[\frac{\pi(x+L)}{4L}\right] - \tan^2\left[\frac{\pi(a+L)}{4L}\right]\right)}{\cos\left[\frac{\pi(x+L)}{4L}\right]\left(\tan\left[\frac{\pi(a+L)}{4L}\right]\tan\left[\frac{\pi(b+L)}{4L}\right] + \tan^2\left[\frac{\pi(x+L)}{4L}\right]\right)^2}\,.\end{aligned} \tag{2.32}$$

The weight functions (2.31) and (2.22) are related as follows

$$\beta_{\rm biloc}(x) = \frac{\pi}{4L}\, \frac{a_L\, b_L\, (1 + x_L^2)^{3/2}}{\sqrt{a_L^2\, b_L^2 + x_L^2}\, (a_L\, b_L + x_L^2)}\, \beta_{\rm loc}(x)\,. \tag{2.33}$$

We find it worth writing an equivalent form for this relation. By using the first equality both in (2.29) and in (2.10), we find that

$$\beta_{\rm biloc}(x) = \sqrt{\frac{\hat{w}'(x)}{\hat{w}'(x_{\rm c})}}\, \hat{\beta}_{\rm biloc}(\hat{w}(x)) = \sqrt{\frac{\hat{w}'(x)}{\hat{w}'(x_{\rm c})}}\, \frac{\hat{\beta}_{\rm loc}(\hat{a}\hat{b}/\hat{w}(x))}{\hat{w}(x) + \hat{a}\hat{b}/\hat{w}(x)} \tag{2.34}$$

where we can use that, from (2.11), (2.13) and (2.27), the following relation holds

$$\hat{w}(x_{\rm c}(x)) = \frac{\hat{a}\, b_L}{x_L} = \frac{\hat{b}\, a_L}{x_L} = \frac{\hat{a}\,\hat{b}}{\hat{w}(x)}\,. \tag{2.35}$$

From (2.22) we get $\hat{\beta}_{\rm loc}(\hat{w}(x_{\rm c})) = \hat{w}'(x_{\rm c})\, \beta_{\rm loc}(x_{\rm c})$ and, combining this relation with (2.34) and (2.35), we find

$$\beta_{\rm biloc}(x) = \sqrt{\hat{w}'(x)\, \hat{w}'(x_{\rm c})}\, \frac{\beta_{\rm loc}(x_{\rm c})}{\hat{w}(x) + \hat{w}(x_{\rm c})} = \frac{\sqrt{\hat{w}'(x)\, \hat{w}'(x_{\rm c})}}{\hat{a}/a_L}\, \frac{\beta_{\rm loc}(x_{\rm c})}{x_L + x_{{\rm c},L}}\,. \tag{2.36}$$

In the last expression of (2.36), by employing (2.12), (2.14) and (2.30), we observe that

$$\frac{\sqrt{\hat{w}'(x)\, \hat{w}'(x_{\rm c})}}{\hat{a}/a_L} = \frac{\pi}{4L}\, \frac{\sqrt{a_L^2\, b_L^2 + x_L^2}}{\sin\left[\frac{\pi(x+L)}{4L}\right]}\,. \tag{2.37}$$

JHEP02(2026)224

Finally, from (2.36) and (2.37), we conclude that (2.33) can be written as follows

$$\beta_{\text{biloc}}(x) = \frac{\pi}{4L} \frac{\sqrt{a_L^2\, b_L^2 + x_L^2}}{\sin\left[\frac{\pi(x+L)}{4L}\right]} \frac{\beta_{\text{loc}}(x_{\text{c}})}{x_L + x_{\text{c},L}} \tag{2.38}$$

whose structure is similar to the relation between the weight functions found in [29].

At the endpoints of A, the weight function in (2.29), (2.31) or (2.32) vanishes in a linear way; indeed, we have that $\beta_{\text{biloc}}(a) = \beta_{\text{biloc}}(b) = 0$ and

$$\beta_{\text{biloc}}(x) = \frac{\pi}{4L} \frac{\cos\left(\frac{\pi b}{2L}\right)}{\cos\left(\frac{\pi a}{2L}\right) \cos\left[\frac{\pi(b+a)}{4L}\right]} (x-a) + O\left((x-a)^2\right) \qquad x \to a \tag{2.39}$$

$$\beta_{\text{biloc}}\,(x) = \frac{\pi}{4L} \frac{\cos\left(\frac{\pi a}{2L}\right)}{\cos\left(\frac{\pi b}{2L}\right) \cos\left[\frac{\pi(b+a)}{4L}\right]} (b-x) + O\left((x-b)^2\right) \qquad x \to b\,. \tag{2.40}$$

Let us discuss the weight function $\beta_{\text{biloc}}(x)$ in (2.29), (2.31) or (2.32) in the same limiting regimes considered above for $\beta_{\text{loc}}(x)$.

When A is adjacent to the boundary [10], the entanglement Hamiltonian K_A becomes local. Indeed, considering $\beta_{\text{biloc}}(x)$ for any given x that does not coincide with the endpoints of A and taking its limit for either $b \to L$ or $a \to -L$, we find either $O(b-L)$ or $O(a+L)$ respectively.

Another limiting case where K_A becomes local corresponds to the interval A in the infinite line [6, 7]; indeed, $\beta_{\text{biloc}}(x) = \frac{\pi(b-x)(x-a)}{4L\,(b-a)} + O(1/L^2)$ as $L \to +\infty$.

Instead, a limiting regime where $\beta_{\text{biloc}}(x)$ remains non trivial corresponds to the case of the interval in the half line explored in [29], which can be recovered by applying the limiting procedure discussed above for $\beta_{\text{loc}}(x)$. Thus, setting $a = \hat{a} - L$, $b = \hat{b} - L$ and $x = \hat{x} - L$ in $\beta_{\text{biloc}}(x)$ first and then taking $L \to +\infty$ in the resulting expression, we find $\beta_{\text{biloc}}(x) = \hat{\beta}_{\text{biloc}}(\hat{x}) + O(1/L^2)$ as $L \to +\infty$, which is the weight function (2.10) of the bilocal term in the entanglement Hamiltonian of an interval $\hat{A} \equiv [\,\hat{a}, \hat{b}\,]$ in the half line, as expected.

As also done for the weight function of the local term, we anticipate that in section 4 the weight function of the bilocal term in (2.29), (2.31) or (2.32) agrees with the exact numerical results obtained for the homogeneous free fermionic chain on the segment (see the solid blue curves in figure 7 and in the bottom panels of figure 11).

The weight function of the local term in (2.22)–(2.23) allows us to evaluate the entanglement entropies for the setup that we are investigating. Indeed, following [9, 32, 33], let us introduce the contour function for the entanglement entropies as

$$C_A^{(n)}(x) \equiv \frac{c}{12}\left(1 + \frac{1}{n}\right) \frac{1}{\beta_{\text{loc}}(x)} \qquad x \in A \tag{2.41}$$

where the integer $n \geqslant 2$ is the Rényi index while the case $n = 1$ corresponds to the entanglement entropy, $c = 1$ for the massless Dirac field, and $\beta_{\text{loc}}(x)$ is the weight function of the local term given in (2.22)–(2.23). A candidate for the entanglement entropies of the interval A in the segment is obtained by integrating the contour function (2.41) over the interval $A_\epsilon \subsetneq A$, where $A_\epsilon \equiv [\,a+\epsilon\,, b-\epsilon\,]$, with $\epsilon \simeq 0^+$ defined as the UV cutoff [9, 47]. This

JHEP02(2026)224

integral can be performed by employing the definition of $\beta_{\rm loc}(x)$ in (2.22), finding

$$\mathcal{I}(r,s) \equiv \int_r^s \frac{\mathrm{d}x}{\beta_{\rm loc}(x)} = \int_{\hat{w}(r)}^{\hat{w}(s)} \frac{\mathrm{d}\hat{w}}{\hat{\beta}_{\mathbb{S},\rm loc}(\hat{w})} = \left(\log\left[\frac{(\hat{w}(y)-\hat{w}(a))\,(\hat{w}(y)+\hat{w}(b))}{(\hat{w}(b)-\hat{w}(y))\,(\hat{w}(y)+\hat{w}(a))} \right] \right)\Big|_{y=r}^{y=s}$$

$$= \log\left[\frac{(b_L-r_L)\,(b_L+s_L)\,(r_L+a_L)\,(s_L-a_L)}{(b_L+r_L)\,(b_L-s_L)\,(r_L-a_L)\,(s_L+a_L)} \right] \tag{2.42}$$

in terms of (2.11) and (2.12), where $a<r<s<b$. The expression for the Rényi entropies is obtained by first specialising (2.42) to the endpoints of A_ϵ and then expanding as $\epsilon \to 0^+$. By employing (2.11), this gives

$$\mathcal{I}(a+\epsilon\,, b-\epsilon) = 2\,\log\left[\frac{2}{\epsilon} \sqrt{\frac{\hat{w}(a)\,\hat{w}(b)}{\hat{w}'(a)\,\hat{w}'(b)}}\; \frac{\hat{w}(b)-\hat{w}(a)}{\hat{w}(a)+\hat{w}(b)} \right] + O(\epsilon) \tag{2.43}$$

$$= 2\,\log\left(\frac{8L}{\pi\,\epsilon}\,\sqrt{a_L\,b_L}\,\cos\left[\frac{\pi(a+L)}{4L}\right]\cos\left[\frac{\pi(b+L)}{4L}\right]\,\frac{b_L-a_L}{a_L+b_L} \right) + O(\epsilon)\,.$$

From (2.41) and (2.43), for the Rényi entropies of an interval A in the segment we find

$$S_A^{(n)} = \frac{n+1}{6\,n}\,\log\left(\frac{4L}{\pi\,\epsilon}\,\sqrt{\cos\left(\frac{\pi a}{2L}\right)\cos\left(\frac{\pi b}{2L}\right)}\;\frac{\sin\left[\frac{\pi(b-a)}{4L}\right]}{\cos\left[\frac{\pi(a+b)}{4L}\right]} \right) + O(1) \tag{2.44}$$

which is the result obtained in [15] by employing that $S_A^{(n)}$ can be expressed as the two-point function of branch-point twist fields [34] located at the endpoints of the interval A. We remark that the procedure employed above to obtain the entanglement entropies (2.44) is based on the contour function (2.41) and therefore it is different from the twist fields method.

It is instructive to consider (2.44) in some relevant limiting regimes.

In the limit $L \to +\infty$, the argument of the logarithm in (2.44) simplifies to $\frac{b-a}{\epsilon}$ and the Rényi entropies of an interval in the infinite line are recovered, as expected.

Another regime that is worth considering for the massless Dirac field corresponds to the interval in the half line, whose Rényi entropies have been discussed in [29]. This limit can be explored by setting $a=\hat{a}-L$, $b=\hat{b}-L$ and $x=\hat{x}-L$ in (2.44) first and then taking $L\to+\infty$, as done above for $\beta_{\rm loc}(x)$ and $\beta_{\rm biloc}(x)$. Following these steps, for the argument of the logarithm in (2.44) one obtains $2\sqrt{\hat{a}\,\hat{b}}\,(\hat{b}-\hat{a})/[(\hat{a}+\hat{b})\epsilon] + O(1/L^2)$; hence, the result obtained in [29] is recovered.

The limit of (2.44) as the interval A becomes adjacent to the boundary is more subtle because the regularisation procedure discussed in [9, 47] requires that $b+\epsilon<L$ and $a-\epsilon>-L$. However, by setting e.g. $b=L-\epsilon$ in (2.44) and expanding as $\epsilon\to0^+$, the leading term of the argument of the logarithm is $\sqrt{\frac{8L}{\pi\epsilon}\cos\left(\frac{\pi a}{2L}\right)}\,[1+O(\epsilon)]$; hence, the result obtained in [10] for the interval adjacent to the boundary is recovered (up to a factor of 2 in the definition of the UV cutoff).

We also find it insightful to introduce the following contour function for the entanglement entropies over the entire spatial segment

$$C_{A,B}^{(n)}(x) \equiv \frac{c}{12}\left(1+\frac{1}{n}\right)\frac{1}{|\beta_{\rm loc}(x)|} \qquad\qquad x\in A\cup B \tag{2.45}$$

JHEP02(2026)224

which becomes (2.41) when $x \in A$. A candidate for the entanglement entropies of B is obtained by integrating (2.45) in $B_\epsilon \subsetneq B$, where $B_\epsilon \equiv [-L\,, a-\epsilon\,] \cup [\,b+\epsilon\,, L\,]$. As a consistency check of (2.45), by employing (2.42) we find that $S_A^{(n)} = S_B^{(n)}$ at leading order when $\epsilon \to 0^+$ (in this computation it has been used that $\mathcal{I}(-L+\epsilon_0, L-\epsilon_0) \to 0$ as $\epsilon_0 \to 0^+$), as expected from the fact that the entire system is in a pure state. Notice that, while the identity $S_A^{(n)} = S_B^{(n)}$ is straightforward when the twist fields method is employed, it provides a non trivial consistency check when the entanglement entropies are obtained from their contour function.

3 Entanglement Hamiltonian in inhomogeneous backgrounds

In this section we extend the analysis of section 2 about the entanglement Hamiltonian and the contour function of the entanglement entropies to the specific class of spatially inhomogeneous backgrounds defined by (3.1). The expressions for these quantities for a generic background belonging to this class are given in section 3.1, while in section 3.2 they are specialised to the rainbow model, providing the predictions for the continuum limit of the numerical analysis in the rainbow chain, discussed in section 4.

3.1 Generic background

We consider the class of two-dimensional manifolds given by the strip $\mathbb{S}$ introduced in section 2 equipped with a metric of the following form

$$ds^2 = \mathrm{e}^{2\sigma(x)}\,\mathrm{d}t_{\mathrm{E}}^2 + \mathrm{d}x^2 = \mathrm{e}^{2\sigma(x)}\,(\mathrm{d}t_{\mathrm{E}}^2 + \mathrm{d}\tilde{x}^2) = \mathrm{e}^{2\sigma(x)}\,\mathrm{d}\zeta\,\mathrm{d}\bar{\zeta} \tag{3.1}$$

where we restrict to the cases having $\sigma(-x) = \sigma(x)$ and $\tilde{x}(x)$ is defined as follows

$$\tilde{x}(x) \equiv \int_0^x \mathrm{e}^{-\sigma(y)}\,\mathrm{d}y \qquad\qquad \tilde{x}'(x) = \mathrm{e}^{-\sigma(x)} \qquad\qquad \zeta \equiv \tilde{x} + \mathrm{i}\,t_{\mathrm{E}}\,. \tag{3.2}$$

Notice that $\tilde{x}(x)$ is an odd function. The inverse function of $\tilde{x}(x)$ will be denoted by $\tilde{f}$ in the following, namely $x = \tilde{f}(\tilde{x})$. The Ricci scalar of the metric in (3.1) is $\mathcal{R} = -2\,[\sigma'(x)^2 + \sigma''(x)]$. From the second equality in (3.1), notice that the Riemannian manifold that we are considering is conformally equivalent to the flat strip $\widetilde{\mathbb{S}}$, described by the coordinates $(\tilde{x}, t_{\mathrm{E}})$ in Euclidean signature and whose width is given by $2\tilde{L}$, with $\tilde{L} \equiv \tilde{x}(L)$.

The inhomogeneous backgrounds characterised by (3.1) occur in the continuum limit of one-dimensional free fermionic systems with a Fermi velocity that depends on the position, i.e. $v_{\mathrm{F}}(x) = J(x) = \mathrm{e}^{\sigma(x)}$ (see also the Hamiltonian (4.1)). This includes the rainbow chain [11–15] (see also [25, 48–54] and the discussions in section 3.2 and section 4), the Fermi gas trapped in a harmonic potential [16, 18, 19, 55–60], the gradient chain [54, 61–63] and other interesting models discussed e.g. in [20, 64]. Furthermore, the Lorentzian metrics obtained by setting $t = -\mathrm{i}t_{\mathrm{E}}$ in (3.1) are also called optical metrics [22–25] and they occur in the study of the light propagation in a medium with an inhomogeneous index of refraction.

We consider a free massless Dirac field on this curved background in Euclidean signature, whose action reads

$$S[\psi] \propto \int_{\mathbb{S}} \mathrm{e}^{\sigma}\Big(\,\psi_2^*\overset{\leftrightarrow}{\partial}_{\bar{\zeta}}\psi_2 + \psi_1^*\overset{\leftrightarrow}{\partial}_{\zeta}\psi_1\,\Big)\,\mathrm{d}\zeta\,\mathrm{d}\bar{\zeta}\,. \tag{3.3}$$

JHEP02(2026)224

The boundary conditions for the components of the Dirac field are obtained from the ones described in section 2 in the flat strip (see (2.19) and (2.20)) through the map $\tilde{x}(x)$ in (3.2) and the Weyl transformation in (3.1). Here the flat strip to consider is $\widetilde{\mathbb{S}}$, whose boundaries are parameterised by $\mp\tilde{L} + \mathrm{i}\, t_{\mathrm{E}}$ with $t_{\mathrm{E}} \in \mathbb{R}$. By performing the change of variable given by $\tilde{x}(x)$ in the boundary conditions (2.19) and (2.20) specified for $\widetilde{\mathbb{S}}$, where $\tilde{x}'(x)$ in (3.2) is real and positive, and considering the factors provided by the Weyl transformation, one finds that the boundary conditions supporting (3.3) are given by (2.19) and (2.20) also in the inhomogeneous case that we are considering.

The entanglement Hamiltonian $K_A^{(\sigma)}$ of an interval A in the segment at $t_{\mathrm{E}} = 0$ embedded in the strip $\mathbb{S}$ can be found from the entanglement Hamiltonian K_A in the flat strip $\widetilde{\mathbb{S}}$, given in (2.21), by adapting to this case the procedure that provides K_A from (2.5), discussed in section 2. The result is

$$K_A^{(\sigma)} = 2\pi \int_a^b \beta_{\mathrm{loc}}^{(\sigma)}(x)\, \mathcal{E}(x)\, \mathrm{d}x + 2\pi \int_a^b \beta_{\mathrm{biloc}}^{(\sigma)}(x)\, T_{\mathrm{biloc}}^{(\alpha)}(x, x_{\mathrm{c},\sigma})\, \mathrm{d}x \tag{3.4}$$

where the local operator $\mathcal{E}(x)$ and the bilocal operator $T_{\mathrm{biloc}}^{(\alpha)}(x,y)$ have the same form as the corresponding ones occurring in (2.21), with the fields in $\widetilde{\mathbb{S}}$ replaced by the corresponding fields in the curved manifold $\mathbb{S}$.

The weight function $\beta_{\mathrm{loc}}^{(\sigma)}(x)$ in the local term of (3.4) can be found by adapting to this case the calculation performed above to obtain (2.22), discussed in section 2. In particular, combining (2.22), (3.2) and the fact that the energy-momentum tensor has conformal dimension equal to 2, for the weight function $\beta_{\mathrm{loc}}^{(\sigma)}(x)$ we find

$$\beta_{\mathrm{loc}}^{(\sigma)}(x) \equiv \frac{\tilde{\beta}_{\mathrm{loc}}(\tilde{x}(x))}{\tilde{x}'(x)} = \mathrm{e}^{\sigma(x)}\, \frac{4\tilde{L}}{\pi} \left[\cos\!\left(\frac{\pi(\tilde{x} + \tilde{L})}{4\tilde{L}} \right) \right]^2 \frac{(\tilde{b}_L^2 - \tilde{x}_L^2)(\tilde{x}_L^2 - \tilde{a}_L^2)}{2(\tilde{b}_L - \tilde{a}_L)(\tilde{a}_L\, \tilde{b}_L + \tilde{x}_L^2)} \tag{3.5}$$

where $\tilde{\beta}_{\mathrm{loc}}(y)$ is defined as (2.22) with a, b and L replaced by $\tilde{a} \equiv \tilde{x}(a)$, $\tilde{b} \equiv \tilde{x}(b)$ and $\tilde{L} \equiv \tilde{x}(L)$ respectively through (3.2), and we have introduced

$$\tilde{x}_L \equiv \tan\!\left[\frac{\pi(\tilde{x}(x) + \tilde{L})}{4\tilde{L}} \right] \qquad \tilde{a}_L \equiv \tilde{x}_L\big|_{x=a} \qquad \tilde{b}_L \equiv \tilde{x}_L\big|_{x=b} \tag{3.6}$$

in terms of the notation defined in (2.12). By employing (2.23), (3.2) and (3.6), the weight function (3.5) can also be written in the following form

$$\beta_{\mathrm{loc}}^{(\sigma)}(x) = \mathrm{e}^{\sigma(x)}\, \frac{2\tilde{L}}{\pi}\, \frac{\left[\sin(\pi\tilde{b}/(2\tilde{L})) - \sin(\pi\tilde{x}/(2\tilde{L}))\right] \left[\sin(\pi\tilde{x}/(2\tilde{L})) - \sin(\pi\tilde{a}/(2\tilde{L}))\right]}{\sin(\pi(\tilde{b} - \tilde{a})/(2\tilde{L})) + \left[\cos(\pi\tilde{b}/(2\tilde{L})) - \cos(\pi\tilde{a}/(2\tilde{L}))\right] \sin(\pi\tilde{x}/(2\tilde{L}))}\,. \tag{3.7}$$

The weight function $\beta_{\mathrm{biloc}}^{(\sigma)}(x)$ in the bilocal term of (3.4) is obtained by adapting the calculation that gives (2.29). In order to write the result, let us first employ (2.26) and (3.6) to define

$$\tilde{x}_{\mathrm{c}}(x) \equiv \frac{4\tilde{L}}{\pi} \arctan\!\left(\frac{\tilde{a}_L\, \tilde{b}_L}{\tilde{x}_L} \right) - \tilde{L} \tag{3.8}$$

that provides the point $x_{\mathrm{c},\sigma}$ conjugate to x as follows

$$x_{\mathrm{c},\sigma}(x) = \tilde{f}(\tilde{x}_{\mathrm{c}}(x)) \tag{3.9}$$

JHEP02(2026)224

through the inverse function of $\tilde{x}(x)$, introduced in the text below (3.2). Notice that $x_{\mathrm{c},\sigma}(x) \in A$ when $x \in A$. Indeed, first one observes that $x_{\mathrm{c},\sigma}(a) = b$, $x_{\mathrm{c},\sigma}(b) = a$ and $\tilde{a}_L < \tilde{x}_L < \tilde{b}_L$ for $a < x < b$. This implies that the argument of the arctan in (3.8) belongs to $(\tilde{a}_L\,, \tilde{b}_L)$. Then, since both arctan and $\tilde{f}$ are monotonic functions, we have that $x_{\mathrm{c},\sigma}(x) \in A$ when $x \in A$. The self-conjugate point at $x = x_{\mathrm{sc},\sigma}$ is defined by the condition $x_{\mathrm{c},\sigma}(x_{\mathrm{sc},\sigma}) = x_{\mathrm{sc},\sigma}$, which is typically a transcendental equation, depending on $\sigma(x)$.

An interesting feature of (3.9) concerns the special case where A is in the centre of the segment, i.e. $a = -b$ with $0 < b < L$. In this case, since $\sigma(-x) = \sigma(x)$, we have that $\tilde{a} = -\tilde{b}$ and $\tilde{a}_L = 1\,/\,\tilde{b}_L$. Then, by using also the identity $\arctan[\cot(y + \pi/4)] = \pi/4 - y$ for $y \in (-\pi/4, \pi/4)$, for (3.8) we find that $\tilde{x}_{\mathrm{c}}(x) = -\tilde{x}$, which can be combined with the fact that $\tilde{f}$ is an odd function, finding that (3.9) for $a = -b$ simplifies to $x_{\mathrm{c},\sigma}(x)\big|_{a=-b} = -x$. Hence, in this symmetric configuration the self-conjugate point is the central point of the segment, namely $x_{\mathrm{sc},\sigma}\big|_{a=-b} = 0$.

The weight function $\beta^{(\sigma)}_{\mathrm{biloc}}(x)$ can be written in terms of (3.2) and (3.9) as follows

$$\beta^{(\sigma)}_{\mathrm{biloc}}(x) = \sqrt{\frac{\tilde{x}'(x)}{\tilde{x}'(x_{\mathrm{c},\sigma}(x))}}\;\tilde{\beta}_{\mathrm{biloc}}(\tilde{x}(x)) \tag{3.10}$$

being $\tilde{\beta}_{\mathrm{biloc}}(x)$ defined as (2.29) (see also the equivalent expressions in (2.31) and (2.32)) with a, b and L replaced by $\tilde{a}$, $\tilde{b}$ and $\tilde{L}$ respectively. More explicit expressions for the weight function (3.10) are obtained from either (2.29) or (2.31), finding respectively

$$\beta^{(\sigma)}_{\mathrm{biloc}}(x) = \mathrm{e}^{[\sigma(x_{\mathrm{c},\sigma})-\sigma(x)]/2}\;\frac{\cos\left[\frac{\pi(\tilde{x}_{\mathrm{c}}+\tilde{L})}{4\tilde{L}}\right]}{\cos\left[\frac{\pi(\tilde{x}+\tilde{L})}{4\tilde{L}}\right]}\;\frac{\tilde{a}_L\,\tilde{b}_L\,(\tilde{b}_L^2-\tilde{x}_L^2)(\tilde{x}_L^2-\tilde{a}_L^2)}{2(\tilde{b}_L-\tilde{a}_L)\,\tilde{x}_L\,(\tilde{a}_L\,\tilde{b}_L+\tilde{x}_L^2)^2} \tag{3.11}$$

$$= \frac{\mathrm{e}^{[\sigma(x_{\mathrm{c},\sigma})-\sigma(x)]/2}\;\tilde{a}_L\,\tilde{b}_L\,(\tilde{b}_L^2-\tilde{x}_L^2)(\tilde{x}_L^2-\tilde{a}_L^2)}{2(\tilde{b}_L-\tilde{a}_L)\,\cos\left[\frac{\pi(\tilde{x}+\tilde{L})}{4\tilde{L}}\right]\sqrt{\tilde{a}_L^2\,\tilde{b}_L^2+\tilde{x}_L^2}\,(\tilde{a}_L\,\tilde{b}_L+\tilde{x}_L^2)^2} \tag{3.12}$$

in terms of (3.6), (3.8) and (3.9).

The weight function $\beta^{(\sigma)}_{\mathrm{biloc}}(x)$ in (3.12) is related to $\beta^{(\sigma)}_{\mathrm{loc}}(x)$ in (3.5) as follows

$$\beta^{(\sigma)}_{\mathrm{biloc}}(x) = \mathrm{e}^{[\sigma(x_{\mathrm{c},\sigma})-3\sigma(x)]/2}\;\frac{\pi}{4\tilde{L}}\;\frac{\tilde{a}_L\,\tilde{b}_L\,(1+\tilde{x}_L^2)^{3/2}}{\sqrt{\tilde{a}_L^2\,\tilde{b}_L^2+\tilde{x}_L^2}\,(\tilde{a}_L\,\tilde{b}_L+\tilde{x}_L^2)}\;\beta^{(\sigma)}_{\mathrm{loc}}(x) \tag{3.13}$$

which becomes (2.33) when $\sigma(x)$ vanishes identically, as expected. Combining (3.10) and (2.38), the relation (3.13) can be written also as

$$\beta^{(\sigma)}_{\mathrm{biloc}}(x) = \mathrm{e}^{[\sigma(x_{\mathrm{c},\sigma})-\sigma(x)]/2}\;\frac{\pi}{4\tilde{L}}\;\frac{\sqrt{\tilde{a}_L^2\,\tilde{b}_L^2+\tilde{x}_L^2}}{\sin\left[\frac{\pi(\tilde{x}+\tilde{L})}{4\tilde{L}}\right]}\;\frac{\tilde{\beta}_{\mathrm{loc}}(\tilde{x}_{\mathrm{c}})}{\tilde{x}_L+\tilde{x}_{\mathrm{c},L}}$$

$$= \mathrm{e}^{-[\sigma(x_{\mathrm{c},\sigma})+\sigma(x)]/2}\;\frac{\pi}{4\tilde{L}}\;\frac{\sqrt{\tilde{a}_L^2\,\tilde{b}_L^2+\tilde{x}_L^2}}{\sin\left[\frac{\pi(\tilde{x}+\tilde{L})}{4\tilde{L}}\right]}\;\frac{\beta^{(\sigma)}_{\mathrm{loc}}(x_{\mathrm{c},\sigma})}{\tilde{x}_L+\tilde{x}_{\mathrm{c},L}} \tag{3.14}$$

JHEP02(2026)224

where the last expression has been obtained by using that, from the first equality in (3.5) evaluated in $x_{\mathrm{c},\sigma}$, we have

$$\tilde{\beta}_{\mathrm{loc}}(\tilde{x}(x_{\mathrm{c},\sigma})) = \mathrm{e}^{-\sigma(x_{\mathrm{c},\sigma})}\, \beta^{(\sigma)}_{\mathrm{loc}}(x_{\mathrm{c},\sigma}) \tag{3.15}$$

whose l.h.s. is $\tilde{\beta}_{\mathrm{loc}}(\tilde{x}_{\mathrm{c}})$ because $\tilde{x}(x_{\mathrm{c},\sigma}) = \tilde{x}_{\mathrm{c}}$, from (3.9).

By adapting the analysis of [54] to our setup, it could be worth introducing

$$\gamma^{(\sigma)}_{\mathrm{loc}}(x) \equiv \mathrm{e}^{-\sigma(x)}\, \beta^{(\sigma)}_{\mathrm{loc}}(x) \qquad\qquad \gamma^{(\sigma)}_{\mathrm{biloc}}(x) \equiv \mathrm{e}^{-[\sigma(x_{\mathrm{c},\sigma})-\sigma(x)]/2}\, \beta^{(\sigma)}_{\mathrm{biloc}}(x)\,. \tag{3.16}$$

For instance, in the case of the rainbow model, whose weight functions are discussed in section 3.2, the auxiliary weight functions (3.16) do not display a singular behaviour, unlike the corresponding weight functions.

The derivation of the entanglement entropies $S_A^{(n)}$ from their contour function that we discussed in section 2 for the homogeneous case can be straightforwardly adapted to the inhomogeneous background that we are investigating. Following [10], from the weight function $\beta^{(\sigma)}_{\mathrm{loc}}(x)$ reported in (3.5) or in (3.7), we introduce the contour function for the entanglement entropies given by

$$C^{(n)}_{A;(\sigma)}(x) \equiv \frac{c}{12}\left(1+\frac{1}{n}\right)\frac{1}{\beta^{(\sigma)}_{\mathrm{loc}}(x)} \qquad\qquad x \in A \tag{3.17}$$

where $c = 1$ for the massless Dirac field. By employing the expression of $\beta^{(\sigma)}_{\mathrm{loc}}(x)$ in (3.5) and the integral in (2.42), it is straightforward to observe that the integral occurring in the determination of the entanglement entropies from the contour function (3.17) reads

$$\mathcal{I}_{(\sigma)}(r,s) \equiv \int_r^s \frac{\mathrm{d}x}{\beta^{(\sigma)}_{\mathrm{loc}}(x)} = \int_{\tilde{x}(r)}^{\tilde{x}(s)} \frac{\mathrm{d}y}{\tilde{\beta}_{\mathrm{loc}}(y)} = \log\left[\frac{(\tilde{b}_L-\tilde{r}_L)\,(\tilde{b}_L+\tilde{s}_L)\,(\tilde{r}_L+\tilde{a}_L)\,(\tilde{s}_L-\tilde{a}_L)}{(\tilde{b}_L+\tilde{r}_L)\,(\tilde{b}_L-\tilde{s}_L)\,(\tilde{r}_L-\tilde{a}_L)\,(\tilde{s}_L+\tilde{a}_L)}\right] \tag{3.18}$$

where $a < r < s < b$ and we have defined $\tilde{r}_L \equiv \tilde{x}_L|_{x=r}$ and $\tilde{s}_L \equiv \tilde{x}_L|_{x=s}$, according to the notation introduced in (3.6). The entanglement entropies $S_A^{(n)}$ are obtained from (3.18), by setting $r = a+\epsilon$ and $s = b-\epsilon$ first and then expanding as $\epsilon \to 0^+$, as done in section 2 to obtain (2.44). At leading order, since $\tilde{r}_L = \tilde{a}_L + \tilde{x}'_L(a)\,\epsilon + O(\epsilon^2)$ and $\tilde{s}_L = \tilde{b}_L - \tilde{x}'_L(b)\,\epsilon + O(\epsilon^2)$, we find

$$\mathcal{I}_{(\sigma)}(a+\epsilon\,,b-\epsilon) = 2\,\log\left[\frac{2}{\epsilon}\sqrt{\frac{\tilde{a}_L\,\tilde{b}_L}{\tilde{x}'_L(a)\,\tilde{x}'_L(b)}}\;\frac{\tilde{b}_L-\tilde{a}_L}{\tilde{a}_L+\tilde{b}_L}\right] + O(\epsilon) \tag{3.19}$$

$$= 2\,\log\left(\frac{8\tilde{L}}{\pi\,\epsilon}\sqrt{\frac{\tilde{a}_L\,\tilde{b}_L}{\tilde{x}'(a)\,\tilde{x}'(b)}}\;\cos\left[\frac{\pi(\tilde{a}+\tilde{L})}{4\tilde{L}}\right]\,\cos\left[\frac{\pi(\tilde{b}+\tilde{L})}{4\tilde{L}}\right]\,\frac{\tilde{b}_L-\tilde{a}_L}{\tilde{a}_L+\tilde{b}_L}\right) + O(\epsilon)$$

where in the last step we also exploited that, from (3.6), we have

$$\tilde{x}'_L(x) = \frac{\pi\;\tilde{x}'(x)}{4\tilde{L}\left(\cos\left[\frac{\pi(\tilde{x}(x)+\tilde{L})}{4\tilde{L}}\right]\right)^2}\,. \tag{3.20}$$

JHEP02(2026)224

The entanglement entropies of the interval A in the segment for the massless Dirac field in the inhomogeneous background characterised by (3.1) and in its ground state are obtained from (3.17) by using (3.19), and read

$$S_A^{(n)} = \frac{n+1}{6\,n}\,\log\left(\frac{4\tilde{L}\,\mathrm{e}^{[\sigma(a)+\sigma(b)]/2}}{\pi\,\epsilon}\,\sqrt{\cos\left(\frac{\pi\,\tilde{a}}{2\tilde{L}}\right)\,\cos\left(\frac{\pi\,\tilde{b}}{2\tilde{L}}\right)}\,\frac{\sin\left[\frac{\pi(\tilde{b}-\tilde{a})}{4\tilde{L}}\right]}{\cos\left[\frac{\pi(\tilde{a}+\tilde{b})}{4\tilde{L}}\right]}\right) + O(1)\,. \tag{3.21}$$

Since this expression coincides with the result obtained in [15] through the twist fields method, this computation provides an important consistency check for (3.17).

In the case of the homogeneous segment, the contour function for the entanglement entropies on the entire segment has been introduced in (2.45), showing that it is consistent with the identity $S_A^{(n)} = S_B^{(n)}$ at leading order as $\epsilon \to 0^+$, as expected from the purity of the ground state. Similarly, in the inhomogeneous background characterised by (3.1), the contour function for the entanglement entropies on the entire segment can be defined through the weight function $\beta_{\rm loc}^{(\sigma)}(x)$ (see (3.5) or (3.7)) as

$$C^{(n)}_{A,B;(\sigma)}(x) \equiv \frac{c}{12}\left(1+\frac{1}{n}\right)\frac{1}{|\beta_{\rm loc}^{(\sigma)}(x)|} \qquad\qquad x \in A\cup B \tag{3.22}$$

that becomes (3.17) for $x \in A$. The expression (3.22) provides a contour function of the entanglement entropies for $x \in B$; hence, $S_B^{(n)}$ can be found by integrating over $B_\epsilon \equiv [-L\,, a-\epsilon\,]\cup[\,b+\epsilon\,, L\,]$. As a consistency check, by using the property $\sigma(-x)=\sigma(x)$ and the fact that $\mathcal{I}(-\tilde{L}+\epsilon_0, \tilde{L}-\epsilon_0) \to 0$ as $\epsilon_0 \to 0^+$, we verified that $S_A^{(n)} = S_B^{(n)}$ at leading order as $\epsilon \to 0^+$.

In the remaining part of this subsection, we explore some limiting regimes for the entanglement Hamiltonian, the contour functions and the entanglement entropies, by assuming that $\sigma(x)$ is independent of the parameters a, b and L.

First, we verify that the main results reported in section 2 are recovered when $\sigma(x)$ vanishes identically, as expected. From (3.2), one observes that $\tilde{x}(x)$ becomes simply x, hence any tilded quantity becomes the corresponding untilded one. For the weight function of the local term, this implies that (3.5) and (3.7) become (2.22) and (2.23) respectively. This tells us that, as for the contour function of the entanglement entropies, we have that (3.17) and (3.22) give (2.41) and (2.45) respectively. Considering the weight function of the bilocal term, in this limiting regime of homogeneous background, the expressions (3.11) and (3.12) simplify to (2.29) and (2.31) respectively. Finally, as for the entanglement entropies, it is straightforward to find that (3.21) becomes (2.44).

It is interesting to explore the behaviour of the weight functions $\beta_{\rm loc}^{(\sigma)}(x)$ and $\beta_{\rm biloc}^{(\sigma)}(x)$ close to the endpoints of A. First, by using (3.20) and (3.2), we observe that at the endpoints of A the following identities hold

$$\mathrm{e}^{\sigma(a)}\,\frac{4\tilde{L}}{\pi}\left[\cos\left(\frac{\pi(\tilde{a}+\tilde{L})}{4\tilde{L}}\right)\right]^2 \tilde{x}_L'(a) = \mathrm{e}^{\sigma(b)}\,\frac{4\tilde{L}}{\pi}\left[\cos\left(\frac{\pi(\tilde{b}+\tilde{L})}{4\tilde{L}}\right)\right]^2 \tilde{x}_L'(b) = 1\,. \tag{3.23}$$

Then, as for the expansion of (3.5) as $x \to a$ and $x \to b$, by employing (3.23) we find that

$$\beta_{\rm loc}^{(\sigma)}(x) = (x-a) + O((x-a)^2) \qquad\qquad x \to a \tag{3.24}$$

$$\beta_{\rm loc}^{(\sigma)}(x) = (b-x) + O((x-b)^2) \qquad\qquad x \to b \tag{3.25}$$

JHEP02(2026)224

which is the behaviour expected from the Bisognano-Wichmann theorem, for any $\sigma(x)$ in the class that we are considering. As for $\beta^{(\sigma)}_{\text{biloc}}(x)$, by combining the relation (3.13) with the expansions (3.24)–(3.25), we find respectively

$$\beta^{(\sigma)}_{\text{biloc}}(x) = \mathrm{e}^{[\sigma(b)-3\sigma(a)]/2}\,\frac{\pi}{4\tilde{L}}\,\frac{\tilde{b}_L\,(1+\tilde{a}_L^2)^{3/2}}{\tilde{a}_L(\tilde{a}_L+\tilde{b}_L)\,(1+\tilde{b}_L^2)^{1/2}}\,(x-a)+O((x-a)^2) \qquad x\to a \tag{3.26}$$

$$\beta^{(\sigma)}_{\text{biloc}}(x) = \mathrm{e}^{[\sigma(a)-3\sigma(b)]/2}\,\frac{\pi}{4\tilde{L}}\,\frac{\tilde{a}_L\,(1+\tilde{b}_L^2)^{3/2}}{\tilde{b}_L(\tilde{a}_L+\tilde{b}_L)\,(1+\tilde{a}_L^2)^{1/2}}\,(b-x)+O((x-b)^2) \qquad x\to b \tag{3.27}$$

where we have also used that $x_{\text{c},\sigma}(a)=b$ and $x_{\text{c},\sigma}(b)=a$ (see the text below (3.9)).

We find it worth concluding this discussion by considering two limiting regimes where the entanglement Hamiltonian becomes a local operator. They correspond to A adjacent to the boundary and to $L\to+\infty$ with the additional condition that $\tilde{L}_\infty$ diverges in this limit.

As for the former limiting case, considering e.g. the limit $b\to L$ in the weight function of the local term (see (3.5) and (3.7)) and of the bilocal term (see (3.11) and (3.12)), we find respectively

$$\beta^{(\sigma)}_{\text{loc}}(x) \;\to\; \mathrm{e}^{\sigma(x)}\,\frac{2\tilde{L}}{\pi}\,\frac{\sin[\pi\tilde{x}/(2\tilde{L})]-\sin[\pi\tilde{a}/(2\tilde{L})]}{\cos[\pi\tilde{a}/(2\tilde{L})]} \qquad\qquad \beta^{(\sigma)}_{\text{biloc}}(x) \;\to\; 0 \tag{3.28}$$

where the second result has been obtained by employing the fact that $x_{\text{c},\sigma}(x)\to L$ as $b\to L$ in (3.9). As for the entanglement entropies in this limit, the same considerations made in section 2 for the homogeneous case (see the text below (2.44)) can be adapted to the expression (3.21), finding the result of [10] (up to a factor of 2 in the definition of the UV cutoff), namely

$$S_A^{(n)} \;\to\; \frac{n+1}{12\,n}\,\log\!\left[\mathrm{e}^{\sigma(a)}\,\frac{8\,\tilde{L}}{\pi\,\epsilon}\,\cos\!\left(\frac{\pi\,\tilde{a}}{2\,\tilde{L}}\right)\right]+O(1)\,. \tag{3.29}$$

In the limit $L\to+\infty$, we have to distinguish between the two cases of divergent and finite $\tilde{L}_\infty$, where $\tilde{L}_\infty$ denotes the limiting value of $\tilde{L}$ as $L\to+\infty$. When $\tilde{L}_\infty$ diverges (like e.g. in the rainbow model discussed in section 3.2), by adapting to (3.5)–(3.7) and (3.11) and (3.12) the computation performed in section 2 for the homogeneous background, we obtain respectively

$$\beta^{(\sigma)}_{\text{loc}}(x) \;\to\; \mathrm{e}^{\sigma(x)}\,\frac{(\tilde{b}-\tilde{x})\,(\tilde{x}-\tilde{a})}{\tilde{b}-\tilde{a}} \qquad\qquad \beta^{(\sigma)}_{\text{biloc}}(x) \;\to\; 0 \tag{3.30}$$

where the second result is obtained by using that $x_{\text{c},\sigma}(x)\to\tilde{f}(\tilde{a}+\tilde{b}-\tilde{x})$ in (3.9). The entanglement entropies (3.21) in this limiting regime become

$$S_A^{(n)} \;\to\; \frac{n+1}{6\,n}\,\log\!\left(\mathrm{e}^{[\sigma(a)+\sigma(b)]/2}\,\frac{\tilde{b}-\tilde{a}}{\epsilon}\right)+O(1) \tag{3.31}$$

in agreement with the infinite volume limit of the expression found in [65] for this quantity on the circle (see e.g. [66–70] for further interesting related results). Instead, when $\tilde{L}_\infty$ is finite, the entanglement Hamiltonian remains non-local. Indeed, the limit of the weight functions in (3.5)–(3.7) and (3.11)–(3.12), of the contour function in (3.17) and of the entanglement entropies in (3.21) can be obtained simply by replacing $\tilde{L}$ with $\tilde{L}_\infty$ in the corresponding expressions.

JHEP02(2026)224

3.2 Rainbow model

In the following, the general results presented in section 3.1 are applied to the rainbow model [11–13], which is defined by the metric (3.1) with

$$\sigma(x) = -h|x| = -\lambda\,|x/L| \qquad\qquad \lambda \equiv hL \tag{3.32}$$

and by the action (3.3) in the vector phase (2.19) with $\alpha_{\text{v}} = 3\pi/2$, as discussed in section 4. The Ricci scalar of the metric given by (3.1) and (3.32) is $\mathcal{R}^{(\text{R})} = 4h\,\delta(x) - 2h^2$; hence, the curvature is constant and negative everywhere except for the point at $x = 0$, where a curvature singularity occurs, which corresponds to the black dot in figure 2. Various interesting features of the rainbow model have been explored e.g. in [10, 15, 25, 48–54].

Specialising (3.2) to (3.32), for the rainbow model we find that

$$\tilde{x}(x) = \int_0^x \mathrm{e}^{h|y|}\,\mathrm{d}y = \operatorname{sign}(x)\,\frac{\mathrm{e}^{h|x|}-1}{h} = L\,\operatorname{sign}(x/L)\,\frac{\mathrm{e}^{\lambda|x/L|}-1}{\lambda} = L\,R_\lambda(x/L) \tag{3.33}$$

where, in order to highlight that $\tilde{x}(x)/L$ is a function of x/L parameterised by λ, in the last step we have introduced

$$R_\lambda(y) \equiv \operatorname{sign}(y)\,\frac{\mathrm{e}^{\lambda|y|}-1}{\lambda} \qquad\qquad -1 \leqslant y \leqslant 1\,. \tag{3.34}$$

Hence, from the text below (3.5), we have that $\tilde{L} = L\,R_\lambda(1)$ for this model. Since $\operatorname{sign}(\tilde{x}) = \operatorname{sign}(x)$, the inverse of (3.33) reads

$$\tilde{f}(\tilde{x}) \equiv \frac{\operatorname{sign}(\tilde{x})}{h}\,\log(1+h|\tilde{x}|) = L\,\frac{\operatorname{sign}(\tilde{x}/L)}{\lambda}\,\log(1+\lambda\,|\tilde{x}/L|) = L\,\mathcal{R}_\lambda(\tilde{x}/L) \tag{3.35}$$

where $\mathcal{R}_\lambda$ denotes the inverse function of (3.34).

From (3.32) and (3.35), the Weyl factor in the intermediate expression of (3.1) specialised to the rainbow model becomes

$$\mathrm{e}^{-2h|x|} = \mathrm{e}^{-2\lambda\,|\mathcal{R}_\lambda(\tilde{x}/L)|} = \frac{1}{\left(1+h|\tilde{x}|\right)^2}\,. \tag{3.36}$$

The metric of Euclidean AdS_2 in Poincaré coordinates is $ds^2 = (R_{\text{AdS}}/y)^2\,(\mathrm{d}t_{\text{E}}^2 + \mathrm{d}y^2)$ with $y > 0$. Comparing this metric with (3.1) having the Weyl factor (3.36), it has been observed in [15] that, by introducing the manifold made by two copies AdS_2^+ and AdS_2^- of Euclidean AdS_2 corresponding to $y > 0$ and $y < 0$ respectively, the Euclidean manifold supporting the rainbow model can be seen as $\mathcal{P}_+ \cup \mathcal{P}_-$, being $\mathcal{P}_\pm \subsetneq \text{AdS}_2^\pm$ the two strips defined by first setting $R_{\text{AdS}} = 1/h$ and then considering $y \in (1/h\,, \mathrm{e}^{hL}/h]$ and $y \in [-\,\mathrm{e}^{hL}/h\,, -1/h)$ respectively.

By employing (3.33), the expressions (3.6) specialised to the rainbow model become

$$\tilde{x}_L = \tan\!\left[\frac{\pi}{4}\left(1 + \frac{R_\lambda(x/L)}{R_\lambda(1)}\right)\right] \qquad\qquad \tilde{a}_L \equiv \tilde{x}_L\big|_{x=a} \qquad \tilde{b}_L \equiv \tilde{x}_L\big|_{x=b} \tag{3.37}$$

which depend on the parameter λ through (3.34).

Consider the rainbow model in the ground state and the bipartition of the segment given by the interval A. Various features of the bipartite entanglement depend on the position of

JHEP02(2026)224

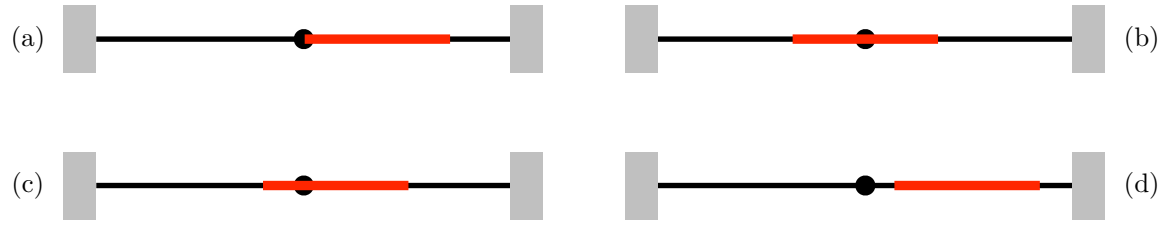

Figure 2. Bipartitions of the segment through an interval A (solid red line) not adjacent to the boundaries, when the middle point of the segment (black dot) plays a special role, like e.g. in the rainbow model.

A with respect to the singularity at $x = 0$ (corresponding to the black dot in figure 2), as discussed below. Since $\sigma(x)$ is an even function, we can consider $b > 0$ and $|a| \leqslant b$ without loss of generality. Thus, only four possibilities occur, and are shown in figure 2: (a) $a = 0$ and $b > 0$; (b) $a = -b$ with $b > 0$ (i.e. $x = 0$ is the middle point of A); (c) $a < 0 < b$ with $|a| \leqslant b$; (d) $0 < a < b$ (i.e. $0 \notin A$). Notice that, while for the entanglement Hamiltonian of A in the configurations (a), (c) and (d) the limit where A is adjacent to the boundary can be considered, recovering the corresponding result in [10], for the configuration (b) this limit is trivial because B vanishes.

As for the weight function of the local term, by using (3.32) and (3.33), we find that (3.5) and (3.7) specialised to the rainbow model give respectively

$$\beta^{(\mathrm{R})}_{\mathrm{loc}}(x) = \frac{2L\,R_\lambda(1)}{\pi\,\mathrm{e}^{\lambda|x/L|}}\left[\cos\left(\frac{\pi}{4}\left(1+\frac{R_\lambda(x/L)}{R_\lambda(1)}\right)\right)\right]^2 \frac{(\tilde b_L^2-\tilde x_L^2)(\tilde x_L^2-\tilde a_L^2)}{(\tilde b_L-\tilde a_L)(\tilde a_L\,\tilde b_L+\tilde x_L^2)} \tag{3.38}$$

and

$$\beta^{(\mathrm{R})}_{\mathrm{loc}}(x) = \frac{2L\,R_\lambda(1)}{\pi\,\mathrm{e}^{\lambda|x/L|}}\,\frac{\left[\sin(\pi\tilde b/(2\tilde L))-\sin(\pi\tilde x/(2\tilde L))\right]\left[\sin(\pi\tilde x/(2\tilde L))-\sin(\pi\tilde a/(2\tilde L))\right]}{\sin(\pi(\tilde b-\tilde a)/(2\tilde L))+\left[\cos(\pi\tilde b/(2\tilde L))-\cos(\pi\tilde a/(2\tilde L))\right]\sin(\pi\tilde x/(2\tilde L))} \tag{3.39}$$

where $\tilde x/\tilde L = R_\lambda(x/L)/R_\lambda(1)$. Thus, the ratio $\beta^{(\mathrm{R})}_{\mathrm{loc}}(x)/L$ is a function of x/L parameterised by a/L, b/L and λ, which provides the solid curves in figure 6 and in the top panels of figure 11.

The weight function for the bilocal term can be written by first introducing the position $x_{\mathrm{c,R}}$ of the point conjugate to a generic point x. From (3.33) and (3.35), we find that (3.8) and (3.9) specialised to the rainbow model give respectively

$$\frac{\tilde x_{\mathrm{c}}(x)}{L} \equiv R_\lambda(1)\left[\frac{4}{\pi}\arctan\left(\frac{\tilde a_L\,\tilde b_L}{\tilde x_L}\right)-1\right] \qquad x_{\mathrm{c,R}}(x) = L\,\mathcal{R}_\lambda(\tilde x_{\mathrm{c}}(x)/L) \tag{3.40}$$

hence also $x_{\mathrm{c,R}}(x)/L$ is a function of x/L parameterised by a/L, b/L and λ. The conjugate point $x_{\mathrm{c,R}}(x)$ in (3.40) provides the black solid curves in figure 4, figure 5, and figure 10.

By specialising (3.12) to the rainbow model and employing (3.40), we find that the weight function of the bilocal term in the rainbow model is

$$\beta^{(\mathrm{R})}_{\mathrm{biloc}}(x) = \frac{\mathrm{e}^{-\lambda(|x_{\mathrm{c,R}}/L|-|x/L|)/2}\;\tilde a_L\,\tilde b_L\,(\tilde b_L^2-\tilde x_L^2)(\tilde x_L^2-\tilde a_L^2)}{2(\tilde b_L-\tilde a_L)\,\cos\left[\frac{\pi}{4}\left(1+\frac{R_\lambda(x/L)}{R_\lambda(1)}\right)\right]\sqrt{\tilde a_L^2\,\tilde b_L^2+\tilde x_L^2}\;(\tilde a_L\,\tilde b_L+\tilde x_L^2)^2} \tag{3.41}$$

JHEP02(2026)224

whose r.h.s. is a function of x/L parameterised by a/L, b/L and λ. The analytic expression (3.41) provides the solid curves in all the panels of figure 7 and in the bottom panels of figure 11.

When the singular point $x = 0$ belongs to A (i.e. $a < 0 < b$), it is worth considering also its conjugate point $x_{\mathrm{c,R}}(0)$. From (3.40), by using that $\tilde{x}_L|_{x=0} = 1$, we find

$$\frac{x_{\mathrm{c,R}}(0)}{L} = \mathcal{R}_\lambda\left(\frac{4\,R_\lambda(1)}{\pi}\,\arctan(\tilde{a}_L\,\tilde{b}_L) - R_\lambda(1)\right) \tag{3.42}$$

which gives the vertical dash-dotted coloured lines in the bottom left panel of figure 7.

As for the auxiliary functions introduced in (3.16) for a generic $\sigma(x)$, in the special case of the rainbow model, from (3.32), they become respectively

$$\gamma^{(\mathrm{R})}_{\mathrm{loc}}(x) = \mathrm{e}^{h|x|}\,\beta^{(\mathrm{R})}_{\mathrm{loc}}(x) \qquad\qquad \gamma^{(\mathrm{R})}_{\mathrm{biloc}}(x) = \mathrm{e}^{h(|x_{\mathrm{c,R}}|-|x|)/2}\,\beta^{(\mathrm{R})}_{\mathrm{biloc}}(x)\,. \tag{3.43}$$

These auxiliary weight functions do not contain absolute values and are smooth over the entire segment, unlike $\beta^{(\mathrm{R})}_{\mathrm{loc}}(x)$ and $\beta^{(\mathrm{R})}_{\mathrm{biloc}}(x)$, which display isolated singular points. In particular, $\beta^{(\mathrm{R})}_{\mathrm{loc}}(x)$ exhibits a cusp singularity at $x = 0$, while $\beta^{(\mathrm{R})}_{\mathrm{biloc}}(x)$ typically displays such a singularity at both $x = 0$ and $x = x_{\mathrm{c,R}}(0)$, as a consequence of the bilocal nature of the bipartite entanglement in the setup that we are exploring. When $a = -b$ with $b > 0$ (see the top right panel of figure 2), since $x_{\mathrm{c,R}}(x) = -x$ we have that $\beta^{(\mathrm{R})}_{\mathrm{biloc}}(x) = \gamma^{(\mathrm{R})}_{\mathrm{biloc}}(x)$; hence $\beta^{(\mathrm{R})}_{\mathrm{biloc}}(x)$ is regular for this type of bipartition (see the solid curves in the top right panel of figure 7).

The contour function for the entanglement entropies in the rainbow model can be easily written by specialising (3.17) and (3.22) to the weight function in (3.38)–(3.39). We find

$$C^{(n)}_{A;(\mathrm{R})}(x) \equiv \frac{1}{12}\left(1+\frac{1}{n}\right)\frac{1}{\beta^{(\mathrm{R})}_{\mathrm{loc}}(x)} \qquad\qquad x \in A \tag{3.44}$$

in the interval A, while over the entire segment it reads

$$C^{(n)}_{A,B;(\mathrm{R})}(x) \equiv \frac{c}{12}\left(1+\frac{1}{n}\right)\frac{1}{|\beta^{(\mathrm{R})}_{\mathrm{loc}}(x)|} \qquad\qquad x \in A\cup B\,. \tag{3.45}$$

The contour function in (3.44) provides the solid curves in figure 8, and the contour function in (3.45) gives the solid curves in figure 12 and figure 13. From (3.38)–(3.39), it is straightforward to observe that $L\,C^{(n)}_{A;(\mathrm{R})}(x)$ and $L\,C^{(n)}_{A,B;(\mathrm{R})}(x)$ are functions of the dimensionless ratio x/L, parameterised by the dimensionless parameters a/L, b/L and $\lambda = hL$.

Finally, as for the entanglement entropies of the interval A in the rainbow model, by specialising (3.21) to this model through (3.32) and (3.33), we find

$$S^{(n)}_A = \frac{n+1}{6\,n}\,\log\left(\frac{4\tilde{L}\,\mathrm{e}^{-h(|a|+|b|)/2}}{\pi\,\epsilon}\,\sqrt{\cos\left(\frac{\pi\,\tilde{a}}{2\tilde{L}}\right)\cos\left(\frac{\pi\,\tilde{b}}{2\tilde{L}}\right)}\,\frac{\sin\left[\frac{\pi(\tilde{b}-\tilde{a})}{4\tilde{L}}\right]}{\cos\left[\frac{\pi(\tilde{a}+\tilde{b})}{4\tilde{L}}\right]}\right) + O(1) \tag{3.46}$$

which provides the solid curves in figure 9, once the $O(1)$ term has been specified, as discussed in section 4 (see (4.23)). The argument of the logarithm in (3.46) depends on the dimensionless quantities ϵ/L, a/L, b/L and $\lambda = hL$.

In the remaining part of this subsection, we describe some interesting limiting regimes of the analytic expressions for the rainbow model reported above. The limits where $h \to 0$

JHEP02(2026)224

(i.e. the limit of homogeneous background), where A becomes adjacent to the boundary, and where A is the interval in the line have been discussed in the final part of section 3.1 for a generic background, and it is straightforward to specialise the expressions derived there to the rainbow model, by using (3.32). In the following, we focus on the limit of large h, i.e. large λ when L is kept fixed, which is the most interesting limiting regime for the rainbow model.

In this limit of large inhomogeneity, let us first observe that (3.37) becomes

$$\tilde{x}_L = 1 + \frac{\pi}{2}\, r_\lambda(x/L) + \dots \qquad\qquad r_\lambda(y) \equiv \mathrm{sign}(y)\, \mathrm{e}^{-\lambda(1-|y|)} \qquad\qquad -1 \leqslant y \leqslant 1 \tag{3.47}$$

where $r_\lambda(x/L) \ll 1$, and the dots denote subleading terms. This observation allows us to write the weight function of the local term in (3.38) at large λ as

$$\beta^{(\mathrm{R})}_{\mathrm{loc}}(x) = \frac{\mathrm{e}^{\lambda(1-|x/L|)}}{h}\; \mathcal{Q}_{A,\lambda}(x/L) + \dots \tag{3.48}$$

where we have introduced the following ratio

$$\mathcal{Q}_{A,\lambda}(y) \equiv \frac{[r_\lambda(b/L) - r_\lambda(y)]\,[r_\lambda(y) - r_\lambda(a/L)]}{r_\lambda(b/L) - r_\lambda(a/L)}\,. \tag{3.49}$$

It is very instructive to specify this result to the types of bipartitions displayed in figure 2. We recall that these configurations, where $|a| \leqslant b$, correspond to all the possible choices because $\sigma(x)$ is an even function. In particular, in our analysis we will consider bipartitions of type (a) and (b) for $x \in A$ (see figure 6), and of type (c) for $x \in A \cup B$ (see figure 6 and figure 11). The behaviour of $\beta^{(\mathrm{R})}_{\mathrm{loc}}(x)$ for a configuration of type (d) is qualitatively the same as the one for type (a). When the singularity is contained in A (i.e. $a < 0 < b$) it is convenient to introduce the interval $A_0 \subsetneq A$ given by $A_0 \equiv (-|a|, |a|)$ when $|a| \leqslant b$, which is symmetric with respect to the origin. Let us denote by A_* the complement of A_0 in A that does not contain the entangling points, by B_* its mirror image with respect to the origin, namely $B_* \equiv \{-x \mid x \in A_*\}$, and by B_0 the complement of B_* in B that does not contain the entangling points. For a bipartition of type (a) and (d) in figure 2 we have $A_0 = \emptyset$, for type (b) we have $A_* = \emptyset$, whereas for type (c) we have both $A_0 \neq \emptyset$ and $A_* \neq \emptyset$. In particular, for type (c) these domains are given by $A_0 = (-|a|, |a|)$, $A_* = (|a|, b)$, $B_* = (-b, -|a|)$ and $B_0 = [-L, -b) \cup (b, L]$. The relevance of A_* and B_* is due to the fact that the limit of large h while L is kept fixed in (3.48) gives

$$|\beta^{(\mathrm{R})}_{\mathrm{loc}}(x)| = \frac{1}{h} + \dots \qquad\qquad x \in A_* \cup B_* \tag{3.50}$$

meaning that $\beta^{(\mathrm{R})}_{\mathrm{loc}}(x)$ displays a plateau in these regions. Since for a bipartition of type (b) we have that $A_* = \emptyset$, such a plateau does not occur in this case. In the ground state of the rainbow chain in the regime of large inhomogeneity, A_* and B_* play an important role, as discussed in section 4 (see figure 3).

Instead, an exponential behaviour in x occurs in this limit when $x \notin A_* \cup B_*$ and is not close to the endpoints of A. For instance, for a bipartition of type (b), we have $r_\lambda(a/L) = -r_\lambda(b/L)$ and $r_\lambda(x/L) < r_\lambda(b/L)$ for any $x \in A$; hence, from (3.48) one obtains

$$\beta^{(\mathrm{R})}_{\mathrm{loc}}(x) = \frac{\mathrm{e}^{h(b-|x|)}}{2\,h} + \dots \qquad\qquad a = -b \qquad\qquad x \in A_0\,. \tag{3.51}$$

JHEP02(2026)224

As for a bipartition of type (c), from (3.48) we get

$$\beta^{(\mathrm{R})}_{\mathrm{loc}}(x) = \frac{\mathrm{e}^{h(|a|-|x|)}}{h} + \dots \qquad a<0<b \qquad |a|<b \qquad x\in A_0 \tag{3.52}$$

and

$$|\beta^{(\mathrm{R})}_{\mathrm{loc}}(x)| = \frac{\mathrm{e}^{h(|x|-b)}}{h} + \dots \qquad a<0<b \qquad |a|<b \qquad x\in B_0\,. \tag{3.53}$$

We highlight the exponential behaviour of $\beta^{(\mathrm{R})}_{\mathrm{loc}}(x)$ in (3.51), (3.52) and (3.53) as $h\to+\infty$. Instead, in the cases given by the bipartitions of type (a) and (d) in figure 2, where $A_0=\emptyset$, such an exponential behaviour of $\beta^{(\mathrm{R})}_{\mathrm{loc}}(x)$ does not occur in A.

As for the conjugate point, assuming $|a|\neq|b|$ and taking $h\to+\infty$ in the first expression in (3.40), we find

$$\tilde{x}_{\mathrm{c}}(x) = \frac{1}{h}\Big[\,\mathrm{sign}(a)\,\mathrm{e}^{h|a|} + \mathrm{sign}(b)\,\mathrm{e}^{h|b|} - \mathrm{sign}(x)\,\mathrm{e}^{h|x|}\,\Big] + \dots \tag{3.54}$$

where (3.47) has been employed, and the dots denote subleading terms. By using (3.54) in the second expression in (3.40), the leading term of the conjugate point in this limit is

$$x_{\mathrm{c,R}}(x) = \mathrm{sign}(\tilde{x}_{\mathrm{c}}(x))\,\max\{|a|\,,|b|\,,|x|\} + \dots \tag{3.55}$$

which is independent of x when $x\in A$ and whose sign can be read from (3.54). For the symmetric configuration (i.e. $a=-b$ with $b>0$), we have that $x_{\mathrm{c,R}}(x)=-x$, as shown in the text below (3.9) for a generic inhomogeneous background belonging to the class (3.1) that we are considering.

In the large inhomogeneity regime, by using (3.47), for the weight function of the bilocal term in (3.41) we find that the leading term can be written in terms of (3.49) as

$$\beta^{(\mathrm{R})}_{\mathrm{biloc}}(x) = \frac{\pi}{4}\,\mathrm{e}^{-\lambda(|x_{\mathrm{c,R}}/L|-|x/L|)/2}\,\mathcal{Q}_{A,\lambda}(x/L) + \dots\,. \tag{3.56}$$

As done above for $\beta^{(\mathrm{R})}_{\mathrm{loc}}(x)$, in the following we specify this result to the types of bipartitions shown in figure 2. In particular, we will again consider bipartitions of type (a) and (b) for $x\in A$ (see figure 7), and of type (c) for $x\in A\cup B$ (see figure 7 and figure 11). The behaviour of $\beta^{(\mathrm{R})}_{\mathrm{biloc}}(x)$ for a configuration of type (d) is qualitatively the same as the one for type (a). In a bipartition of type (b), we find that (3.56) simplifies to

$$\beta^{(\mathrm{R})}_{\mathrm{biloc}}(x) = \frac{\pi}{8}\,\mathrm{e}^{-h(L-b)} + \dots \qquad a=-b \qquad x\in A_0 \tag{3.57}$$

which is independent of x, like (3.50). Remarkably, in the regime of large inhomogeneity, a plateau occurs in $\beta^{(\mathrm{R})}_{\mathrm{biloc}}(x)$ for the configuration where $\beta^{(\mathrm{R})}_{\mathrm{loc}}(x)$ does not display any plateau in A. However, the height of this plateau is exponentially suppressed as h grows. In all the other cases, $\beta^{(\mathrm{R})}_{\mathrm{biloc}}(x)$ has an exponential behaviour in x in this regime. For instance, considering the bipartitions of type (a), (c) and (d), where $|a|<b$ with $b>0$, we find that (3.56) simplifies to

$$|\beta^{(\mathrm{R})}_{\mathrm{biloc}}(x)| = \frac{\pi}{4}\,\mathrm{e}^{-h\,\alpha(x)} + \dots \qquad |a|<b \qquad b>0 \tag{3.58}$$

JHEP02(2026)224

where $\alpha(x) = (L - |x|) + \frac{1}{2}(b - |x|)$ for the bipartitions of type (a) and (d) in $x \in A_*$ and of type (c) in $x \in A_* \cup B_*$, while for a bipartition of type (c) in $x \in A_0$ and in $x \in B_0$ we have that $\alpha(x) = (L - |a|) + \frac{1}{2}(b - |x|)$ and $\alpha(x) = (L - |x|) - (|x| - b)$ respectively. Since $\alpha(x) > 0$ for any $x \in A$, we conclude that $\beta^{(\mathrm{R})}_{\mathrm{biloc}}(x)$ goes to zero as $h \to +\infty$ for $x \in A$. In a bipartition of type (b), where $A_* = \emptyset$, such an exponential behaviour in $x \in A$ does not occur for $\beta^{(\mathrm{R})}_{\mathrm{biloc}}(x)$, but it still vanishes as $h \to +\infty$ because the height of the plateau (3.57) is exponentially suppressed in h.

As for the auxiliary weight functions (3.43), from (3.48) and (3.56) we see that their expansions in the large h regime read

$$\gamma^{(\mathrm{R})}_{\mathrm{loc}}(x) = \frac{\mathrm{e}^{\lambda}}{h}\, \mathcal{Q}_{A,\lambda}(x/L) + \dots \qquad\qquad \gamma^{(\mathrm{R})}_{\mathrm{biloc}}(x) = \frac{\pi}{4}\, \mathcal{Q}_{A,\lambda}(x/L) + \dots \tag{3.59}$$

in terms of the ratio (3.49), which therefore determines the behaviour in x of both auxiliary weight functions in this regime.

As for the entanglement entropies for the rainbow model in (3.46), their limits for A adjacent to the right boundary and A in the line are obtained by specialising to (3.32) the expressions reported in (3.29) and (3.31) for a generic $\sigma(x)$, respectively. Some of them have been largely discussed in the literature on the rainbow chain [11–13, 15].

In the following, we consider the limit of (3.46) as $h \to +\infty$. When $|a| \neq |b|$, we find

$$S^{(n)}_A = \frac{(n+1)\, h}{12\, n}\, \max\{\, |b| - |a|\,, |a| - |b|\,\} - \frac{n+1}{6\, n}\, \log(h\, \epsilon) + \dots \tag{3.60}$$

where the dots denote subleading terms. Thus, for the bipartitions of type (a) and (d) in figure 2 the entanglement entropies $S^{(n)}_A$ display a scaling behaviour given by the length of A, namely a volume law. The Gibbs entropy S_{th} of a system of finite length ℓ coming from the Stefan-Boltzmann law for a two-dimensional CFT with central charge c is $S_{\mathrm{th}} = \pi\, c\, \ell/(3\beta)$ [71–73]. Comparing this result specialised to $c = 1$ and $\ell = b - a$ with S_A in the rainbow model for the bipartitions of type (a) and (d) obtained from (3.60), one finds the following effective (large) temperature [13]

$$T_{\mathrm{R}} = \frac{h}{2\pi}\,. \tag{3.61}$$

As for the bipartition of type (c), the scaling of $S^{(n)}_A$ in (3.60) is given by the length of A_*, i.e. by $b - |a| < b - a$; hence, (3.61) is obtained by comparing S_A with the Gibbs entropy of a system of effective length $\ell = b - |a|$. Instead, in the symmetric configuration where $|b| = |a|$ (i.e. the bipartition of type (b) in figure 2), while the result (3.60) still holds (the first term in the r.h.s. does not occur and only the term proportional to $\log(h\,\epsilon)$ remains), S_A does not scale as a length anymore, and therefore it cannot be interpreted as a thermal entropy.

We find it worth remarking that, since the entanglement entropies $S^{(n)}_A$ can be found from the contour function (3.44), these observations can be made also by employing the asymptotics given by (3.50), (3.51) and (3.52).

The analogy between the mixed state ρ_A obtained from the ground state of the rainbow model in the large h regime and the thermal state at effective temperature T_{R} given by (3.61) performed at the level of the density matrices allows us to refine the previous discussion.

JHEP02(2026)224

Indeed, by employing the above considerations about the behaviour of the weight functions $\beta^{(\mathrm{R})}_{\mathrm{loc}}(x)$ and $\beta^{(\mathrm{R})}_{\mathrm{biloc}}(x)$ as $h \to +\infty$ (see (3.48)–(3.52) and (3.56)–(3.58) respectively), for the entanglement Hamiltonian K_A (see (3.4) specialised to the rainbow model) in this regime we find $K_A = \frac{1}{T_{\mathrm{R}}} \int_A \mathcal{E}(x)\, \mathrm{d}x + \dots$ for the bipartitions of type (a) and (d) in figure 2, in terms of the energy density $\mathcal{E}(x)$ and the large effective temperature (3.61), where the dots denote subleading terms. Hence, in these cases the reduced density matrix becomes the density matrix of a thermal state. Instead, for the bipartitions of type (c), the expansion of K_A does not give $\frac{1}{T_{\mathrm{R}}} \int_{A_*} \mathcal{E}(x)\, \mathrm{d}x + \dots$, because of the exponential behaviour of $\beta^{(\mathrm{R})}_{\mathrm{loc}}(x)$ in $x \in A_0$ given by (3.52). Also for a bipartition of type (b) we find that ρ_A is not approximated by a thermal density matrix in the large inhomogeneity regime, since in this case $\beta^{(\mathrm{R})}_{\mathrm{loc}}(x)$ displays the exponential behaviour (3.51) over the entire interval A (except close to the entangling points, where a linear behaviour occurs). In all bipartitions of figure 2, the weight function $\beta^{(\mathrm{R})}_{\mathrm{biloc}}(x)$ is exponentially suppressed in h at large inhomogeneity, and therefore its contribution is negligible with respect to $\beta^{(\mathrm{R})}_{\mathrm{loc}}(x)$. Thus, the thermal behaviour at the effective temperature (3.61) for ρ_A in the regime of large inhomogeneity is determined by the local term of K_A, and it is observed only when $A_0 = \emptyset$, namely when S_A satisfies a proper volume law, which scales with the length of A.

4 Entanglement Hamiltonian of a block in the rainbow chain

In this section we explore the quantities discussed in the previous section for the rainbow chain, providing numerical checks of the analytic expressions reported in section 3.2.

Consider the class of inhomogeneous free fermionic chains characterised by the following Hamiltonian (see e.g. [11–13, 15, 25])

$$H = -\sum_{m \in \mathbb{M}} J_m (c^\dagger_m\, c_{m+1} + \mathrm{h.c.}) \tag{4.1}$$

where $c^\dagger_m$ and c_m are the usual creation and annihilation operators of a fermionic particle at the m-th site, $\mathbb{M}$ contains the discrete values labelling the sites of the chain and $J_m > 0$ are the hopping parameters characterising the inhomogeneity of the free fermionic chain. The models described by (4.1) in the continuum limit are related to the ones considered in section 3.1; indeed, in the continuum limit, the hopping parameters J_m provide the function $J(x) = \mathrm{e}^{\sigma(x)}$, where $\sigma(x)$ is the function occurring in the metric (3.1).

The rainbow chain [11–15] belongs to the class defined by (4.1); indeed, its Hamiltonian is

$$H = -\frac{J_0}{2}\, c^\dagger_{\frac{1}{2}} c_{-\frac{1}{2}} - \frac{J_0}{2} \sum_{m=\frac{1}{2}}^{L-\frac{3}{2}} \mathrm{e}^{-hm} \Big[c^\dagger_m\, c_{m+1} + c^\dagger_{-m}\, c_{-(m+1)} \Big] + \mathrm{h.c.} \tag{4.2}$$

where $J_0 > 0$ provides the energy scale, $h \geqslant 0$ is the parameter characterising the inhomogeneity of the hopping amplitudes and $2L$ is the total number of sites. The boundary conditions are given by the following requirements [13]

$$c_{\pm(L+1/2)} = 0\,. \tag{4.3}$$

JHEP02(2026)224

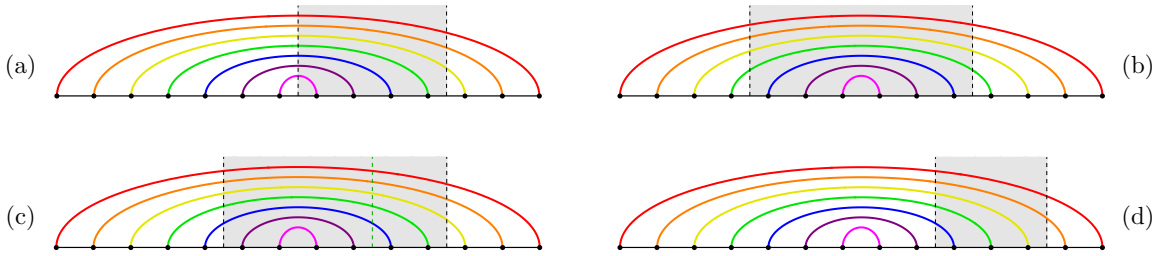

Figure 3. Rainbow state for the bipartitions in figure 2. The grey strip corresponds to A, and the vertical dashed green line identifies $A_* \subsetneq A$ for the configuration of type (c).

A Jordan-Wigner transformation brings (4.2) into the Hamiltonian of an inhomogeneous spin-$\frac{1}{2}$ XX chain. The case $h = 0$ corresponds to the homogeneous free fermionic chain in a segment made by $2L$ sites. In the regime of strong inhomogeneity, the ground state of (4.2) becomes a valence bond state (the rainbow state) that can be explored by applying the strong disorder renormalization group algorithm of Dasgupta and Ma [74] (see also [11, 12, 75]). In the XX version of the Hamiltonian, this valence bond state is constructed from singlets between the sites labelled by m and $-m$ carrying an energy proportional to $J_0\, \mathrm{e}^{-2mh}$, with $m = 1/2, \ldots, L - 1/2$ (see figure 3, where each coloured curve corresponds to a singlet). In the segment supporting the rainbow chain (4.2), we consider the bipartition given by a block A in generic position, made by L_A contiguous sites, and its complement B, containing $L_B = 2L - L_A$ sites. Notice that B is made by contiguous sites only when A is adjacent to one of the boundaries of the rainbow chain. In the strong inhomogeneity regime, the entanglement entropy S_A of a certain bipartition is obtained simply by counting the number of bonds having one endpoint in A and one in B. Hence, when A is adjacent to the boundary and it contains at most L sites, the entanglement entropy satisfies a volume law. This important feature is also observed for some configurations where the block A is not adjacent to the boundary, as discussed below in more detail (in particular, see the bipartitions of type (a) and (d) in figure 2 and figure 3). We remark that, while the entanglement entropy of a gapped lattice model in one spatial dimension characterised by local interactions and in its ground state always satisfies an area law [76], this behaviour is quite unusual in lattice models at the critical point. In the rainbow chain, which is a critical lattice model, the volume law is induced by the particular form of the hopping parameters.

For the bipartitions of the rainbow chain shown in figure 2, an illustrative representation of the rainbow state is displayed in figure 3, where the different colours of the singlets denote the different energies needed to break them. This valence bond structure holds in the asymptotic limit of large inhomogeneity $h \to +\infty$. In figure 3, the grey rectangle delimited by the vertical dashed black lines corresponds to the block A. The linear scaling of S_A in the regime of strong inhomogeneity is determined by the singlets having one endpoint in A and the other one in B. Hence, in the configurations of type (a) and (d) the entanglement entropy satisfies a genuine volume law. In the configuration of type (c), where the endpoints a and b of A are such that $a < 0 < b$ and $|a| < b$, it is worth identifying the block $A_* \subsetneq A$ (see the text above (3.50) and the vertical dashed green line in the bottom left panel of

JHEP02(2026)224

figure 3); indeed, S_A scales like the length L_{A_*} of A_*, which is $L_{A_*} < L_A$ and therefore we do not have a proper volume law scaling in this case. Also in the configuration of type (b) a volume law scaling does not occur because in this case all the singlets of the rainbow state have both their supporting sites either in A or in B; hence, the entanglement entropy of this bipartition vanishes in the regime of large inhomogeneity [11].

The weak inhomogeneity regime in the rainbow chain leads to study its continuum limit, which provides the rainbow model [13] (see section 3.2). This is done by first introducing the lattice spacing a and then taking the limit $\mathsf{a} \to 0$, $h \to 0$ and $L \to +\infty$, while h/a and $L\,\mathsf{a}$ are kept fixed; hence, $\lambda = hL$ is independent of the lattice spacing. The position in the segment is labelled by $x = \mathsf{a}\,m$. In this limiting procedure, it is convenient to rename h/a and $L\,\mathsf{a}$ as h and L respectively. Thus, in the continuum limit h and L have the dimensions of inverse length and length respectively. The two chiral fields $\psi_1(x)$ and $\psi_2(x)$ in the continuum limit are introduced as the slow varying modes of c_m expanded around $\pm k_{\mathrm{F}}$ at half filling $k_{\mathrm{F}} = \pi/(2\mathsf{a})$, namely

$$\frac{c_m}{\sqrt{\mathsf{a}}} \simeq \mathrm{e}^{\mathrm{i}\,k_{\mathrm{F}}\,x}\,\psi_1(x) + \mathrm{e}^{-\mathrm{i}\,k_{\mathrm{F}}\,x}\,\psi_2(x)\,. \tag{4.4}$$

Combining this expansion with the boundary conditions (4.3), in the continuum limit one finds the following boundary conditions at the endpoints of the segment [13]

$$\psi_2(\pm L) = \mp\mathrm{i}\,\psi_1(\pm L) \tag{4.5}$$

which couple the fields with different chirality at the boundaries. Comparing (4.5) with (2.19) and (2.20) at $t_{\mathrm{E}} = 0$, we observe that the boundary conditions of the rainbow model correspond to the case $\alpha_{\mathrm{v}} = 3\pi/2$ of the vector phase.

Since the fermionic model (4.2) is quadratic and its ground state is Gaussian, the crucial quantity to consider in order to explore the bipartite entanglement is the correlation matrix C in the ground state, whose generic element is $C_{m,n} \equiv \langle c_m^\dagger c_n \rangle$. This correlation matrix can be found by first writing (4.2) as $H = \sum_{m,n} H_{m,n}\, c_m^\dagger\, c_n$ with $H_{m,n} = J_m\,\delta_{n,m+\mathrm{sign}(m)} + J_n\,\delta_{m,n+\mathrm{sign}(n)}$, $J_m = -J_0\,\mathrm{e}^{-h\,|m|}/2$ and $m, n \in \{-(L-\frac{1}{2}), \dots, L-\frac{1}{2}\}$. Here, $\delta_{r,s}$ is the Kronecker delta, and $H_{m,n} = -J_0/2$ for either $(m,n) = (\frac{1}{2}, -\frac{1}{2})$ or $(m,n) = (-\frac{1}{2}, \frac{1}{2})$. In our numerical analysis (where the map $m \mapsto m + (L-\frac{1}{2}) + 1$ has been used in order to work with positive integers for the labels of the sites), we set $J_0 = 1$. The generic element of the ground state correlation matrix is obtained through the numerical diagonalisation of the matrix $H_{m,n}$ as $C_{m,n} = \sum_{q \in Q_0} v_q(m)\, v_q(n)$, where $v_q(m)$ is the real eigenvector associated with the eigenvalue $\mathcal{E}_q$ of $H_{m,n}$ and $Q_0 \equiv \{q \mid \mathcal{E}_q < 0\}$ (see e.g. [50]).

The entanglement entropy S_A and the Rényi entropies $S_A^{(n)}$ in the free fermionic chain (4.2) are obtained through the standard procedure [3, 35, 77–81]. In particular, one first constructs the reduced correlation matrix C_A by restricting the ground state correlation matrix C to the subsystem A, namely $(C_A)_{i,j} \equiv C_{i,j}$ for $i, j \in A$, and then computes the eigenvalues ζ_k of C_A numerically. This spectrum provides S_A and $S_A^{(n)}$ as

$$S_A = \sum_{k=1}^{L_A} f_1(\zeta_k) \qquad\qquad S_A^{(n)} = \sum_{k=1}^{L_A} f_n(\zeta_k) \tag{4.6}$$

JHEP02(2026)224

where

$$f_1(x) \equiv -x\log(x) - (1-x)\log(1-x) \qquad f_n(x) \equiv \frac{1}{1-n}\,\log\big[x^n + (1-x)^n\big] \tag{4.7}$$

that satisfy $f_n(x) \to f_1(x)$ as $n \to 1$; hence, $S_A^{(n)} \to S_A$ as $n \to 1$. The complementary region B is made by two disjoint blocks of contiguous sites when A is not adjacent to the boundary, and its entanglement entropies are obtained in the same way from the reduced correlation matrix C_B, whose generic element is $(C_B)_{i,j} \equiv C_{i,j}$ for $i, j \in B$.

A crucial role in our work is played by a specific construction of the contour functions for the entanglement entropy and the Rényi entropies that has been first proposed for the homogeneous free fermionic chain in [32]. These contour functions provide a more refined description of the bipartite entanglement with respect to the corresponding entanglement entropies. Indeed, also the eigenvectors $\phi_k(i)$ of the reduced correlation matrix C_A are involved in their construction and not only the eigenvalues ζ_k. Since the eigenvectors $\phi_k(i)$ of C_A are normalised by the condition $\sum_{i\in A} |\phi_k(i)|^2 = 1$ for every $1 \leqslant k \leqslant L_A$, it is natural to introduce

$$p_k(i) \equiv |\phi_k(i)|^2 \qquad i \in A \qquad 1 \leqslant k \leqslant L_A \tag{4.8}$$

which are often called mode participation functions [31] and allow us to write the entanglement entropies in (4.6) respectively as

$$S_A = \sum_{i\,\in\,A} \mathcal{C}_A(i) \qquad S_A^{(n)} = \sum_{i\,\in\,A} \mathcal{C}_A^{(n)}(i) \tag{4.9}$$

where $\mathcal{C}_A(i) \geqslant 0$ and $\mathcal{C}_A^{(n)}(i) \geqslant 0$ are the contour functions for the entanglement entropy and the Rényi entropies respectively. These contour functions can be written through (4.7) and the mode participation functions in (4.8) as follows

$$\mathcal{C}_A(i) \equiv \sum_{k=1}^{L_A} f_1(\zeta_k)\, p_k(i) \qquad \mathcal{C}_A^{(n)}(i) \equiv \sum_{k=1}^{L_A} f_n(\zeta_k)\, p_k(i) \qquad i \in A\,. \tag{4.10}$$

They provide information about the spatial structure of the bipartite entanglement between A and its complement. It is worth remarking that the construction of the contour functions for the entanglement entropies is highly non-unique. Despite the fact that some properties have been proposed [32], a complete list of properties characterising the contour functions in a unique way is still not available. Moreover, infinitely many contour functions can be written among the ones associated with mode participation functions $p_k(i)$ satisfying the condition $\sum_{i\in A} p_k(i) = 1$ with $p_k(i) \geqslant 0$. However, it is natural to expect that the most reasonable ones are constructed from the eigenvalues and the eigenvectors of the reduced correlation matrix. The definitions of the mode participation function and of the contour functions given in (4.8)–(4.10) for the block A can be adapted also to the subsystem B. One of the main results of this manuscript consists in providing numerical evidence that the continuum limit of the contour functions (4.10) with $p_k(i)$ given by (4.8) is related to the functions defined in (3.44) and (3.45) through the weight function of the local term of the entanglement Hamiltonian (see figure 8, figure 12 and figure 13). Some contour functions have been constructed also in harmonic lattices [31, 33, 82].

JHEP02(2026)224

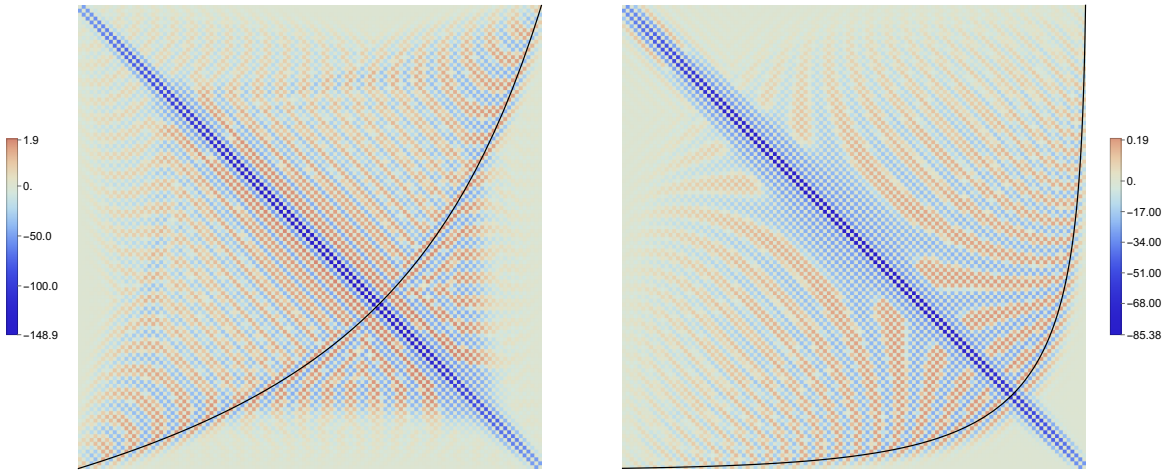

Figure 4. Elements of the matrix (4.12) characterising the entanglement Hamiltonian (4.11) of a block in the configuration of type (a) (see figure 2) with $a = 0$ and $b = 0.8\,L$, when the block has $L_A = 120$ sites in a rainbow chain made by $2L = 300$ sites, with either $\lambda = 0$ (left) or $\lambda = 5$ (right). The black solid curve indicates the position of the conjugate point (3.40).

The most complete description of the subsystem A is given by its reduced density matrix ρ_A or, equivalently, by the corresponding entanglement Hamiltonian $\mathcal{K}_A$, provided that ρ_A has non vanishing eigenvalues. For the rainbow chain (4.2) in its ground state, the entanglement Hamiltonian takes the following quadratic form

$$\mathcal{K}_A = \sum_{i,j\in A} K_{i,j}\, c_i^\dagger\, c_j \tag{4.11}$$

where the $L_A \times L_A$ matrix K is obtained from the reduced correlation matrix C_A through Peschel's formula [35]

$$K = \log(C_A^{-1} - \mathbf{1}) \tag{4.12}$$

which tells us that K and C_A have the same real eigenvectors $\phi_k(i)$. Hence, the matrix K can be written through its spectral representation as follows

$$K_{i,j} = \sum_{k=1}^{L_A} \varepsilon_k\, \phi_k(i)\, \phi_k(j) \tag{4.13}$$

where the single-particle entanglement energies ε_k read

$$\varepsilon_k \equiv \log(1/\zeta_k - 1) \qquad\qquad 1 \leqslant k \leqslant L_A \tag{4.14}$$

in terms of the eigenvalues ζ_k of C_A, which provide the entanglement entropies through (4.6).

We remark that, while the entanglement entropies (4.6) are fully determined by the eigenvalues ζ_k of C_A, both in the contour functions (4.10) and in the entanglement Hamiltonian matrix (4.12)–(4.13) also the eigenvectors $\phi_k(i)$ of C_A occur.

In figure 4 and figure 5 we show the elements of the matrix (4.12) characterising the entanglement Hamiltonian (4.11) in the case of a bipartition of type (a) and (c) respectively

JHEP02(2026)224

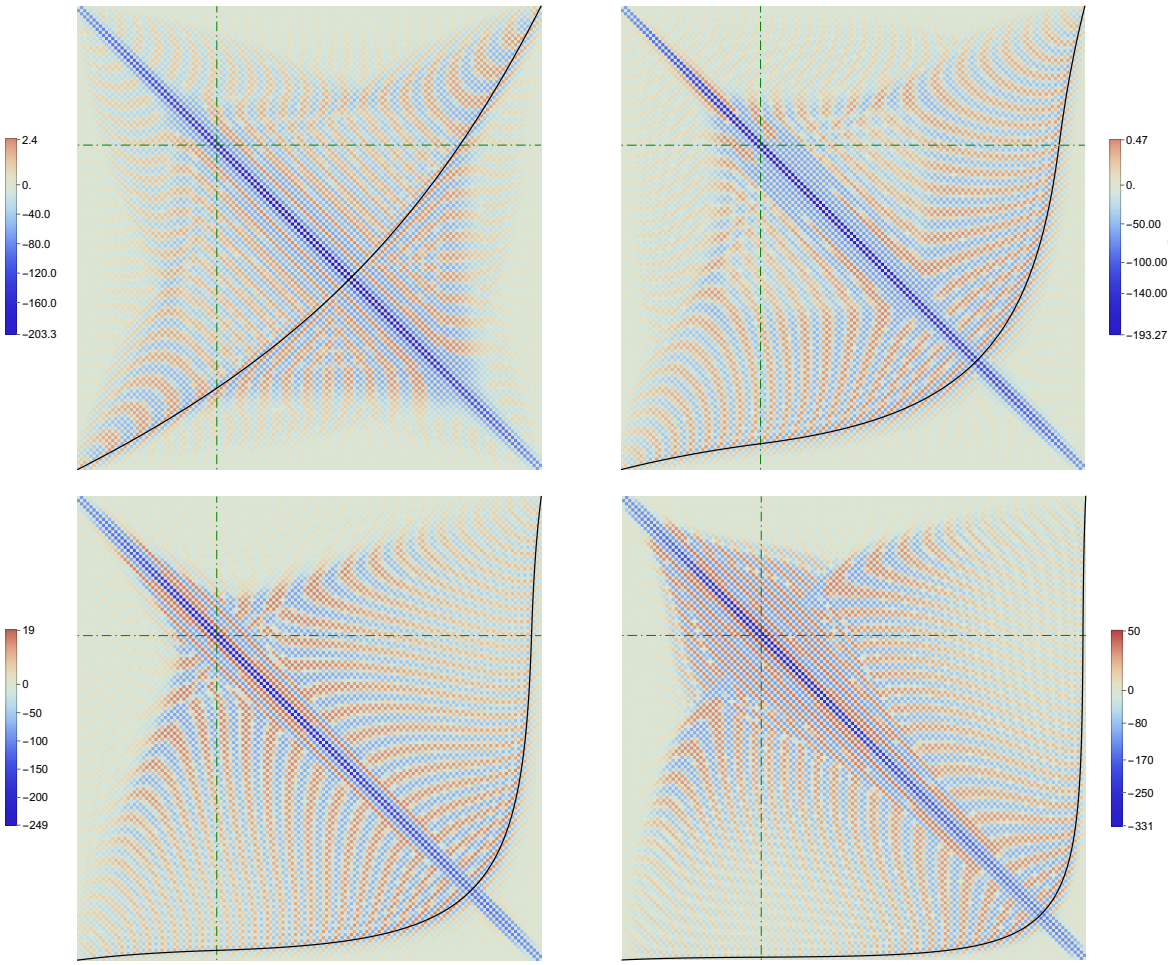

Figure 5. Elements of the matrix (4.12) characterising the entanglement Hamiltonian (4.11) of a block for a configuration of type (c) (see figure 2) with $a = -0.3\,L$ and $b = 0.7\,L$, when the block has $L_A = 150$ sites in a rainbow chain made by $2L = 300$ sites, with either $\lambda = 0$ (top left), $\lambda = 3$ (top right), $\lambda = 5$ (bottom left), or $\lambda = 7.5$ (bottom right). The black solid curve indicates the position of the conjugate point (3.40).

(see figure 2), for different values of the inhomogeneity parameter h (or λ equivalently, since L is kept fixed). The largest elements are located on the odd diagonals around the main diagonal. All the elements of the even diagonals, including the main diagonal, are zero. It is crucial to also understand the role played by the smaller matrix elements located away from the main diagonal in the continuum limit procedure. Indeed, they are essential to obtain the weight functions of both the local and non-local terms of the entanglement Hamiltonian in the continuum. However, their presence alone is not sufficient to determine whether the entanglement Hamiltonian in the continuum also contains non-local terms. This feature is encoded in the specific structure of the terms along all the odd diagonals away from the main diagonal [36, 37, 39]. For instance, the solid black curve indicates the position of the conjugate point in A given by (3.40), which nicely describes the front formed by the off-diagonal matrix elements. This front could indicate the occurrence of a bilocal term in the entanglement Hamiltonian. The dash-dotted green segments in figure 5 denote the position of the centre of

JHEP02(2026)224

the chain, which supports the singularity of the background in the continuum limit. This point plays a special role in the off-diagonal structure of the entries that becomes evident in the regime of large inhomogeneity, as shown in the bottom right panel of figure 5. The effect of the inhomogeneity in the rainbow chain on the matrix elements of K in (4.12) can be observed by comparing the two panels in figure 4 or the four panels in figure 5. The matrix in the left panel of figure 4 is qualitatively similar to the matrix occurring in the entanglement Hamiltonian of a block in a homogeneous chain of free fermions on the half line when the block is not adjacent to the boundary [39], i.e. when the first site of the block does not coincide with the first site of the infinite chain on the half line. As the inhomogeneity grows, the solid black curve (3.40) deforms towards the bottom right corner of the matrix plot until this front disappears. This can be seen from (3.55), which tells us that $x_{\mathrm{c,R}}(x) \to b$ in the large inhomogeneity limit for the bipartitions considered in figure 4 and figure 5.

In order to test numerically the weight functions $\beta^{(\mathrm{R})}_{\mathrm{loc}}(x)$ and $\beta^{(\mathrm{R})}_{\mathrm{biloc}}(x)$ obtained in section 3.2 for the rainbow model in the continuum (see (3.38)–(3.39) and (3.41) respectively) through the entanglement Hamiltonian matrix (4.12) specialised to the rainbow chain, we follow the procedure introduced in [36, 37, 39] for the homogeneous fermionic chain, that has been developed by building also on the results of [83, 84] about the thermodynamic limit of the diagonals of (4.12).

As for the weight function of the local term, let us introduce the combination of the matrix elements of (4.12) given by [36, 37]

$$\beta^{(\mathrm{R})}_{\mathrm{loc}}(i) = -\frac{1}{\pi} \sum_{p=0}^{p_{\max}} (-1)^p \, (2p+1) \, K_{i-p,i+p+1} \tag{4.15}$$

where the cutoff $p_{\max}$ corresponds to the maximal choice guaranteeing that both indices of $K_{i-p,i+p+1}$ belong to A, for each $i \in A$. In particular, $p_{\max}$ depends on i and is given by $p_{\max} \equiv \min\{\, i - m_a \,, m_b - (i+1) \,\}$, where m_a and m_b label the first and last site of the block A respectively (see also [39]). A slightly different combination of matrix elements reads

$$\beta^{(\mathrm{R})}_{\mathrm{loc}}(i) = -\frac{1}{2\pi} \sum_{j \in A} \sin[\pi(j-i)/2] \, (j-i) \, K_{i,j} \tag{4.16}$$

which involves the elements along the i-th row. In the case of the entanglement Hamiltonian of a block in harmonic chains, the results corresponding to different combinations of matrix elements have been compared in [38]. This analysis for the rainbow chain is too cumbersome to be reported here; hence we just provide the choice corresponding to the best agreement with the expressions in the continuum limit among the ones we have considered. In our numerical analysis, we have employed (4.15) in A and (4.16) in B, as discussed below.

In order to improve the agreement observed between the numerical data points and the corresponding analytic results, we find it convenient to introduce the following average

$$\bar{\beta}^{(\mathrm{R})}_{\mathrm{loc}}(i) \equiv \frac{\beta^{(\mathrm{R})}_{\mathrm{loc}}(i)}{2} + \frac{\beta^{(\mathrm{R})}_{\mathrm{loc}}(i+1) + \beta^{(\mathrm{R})}_{\mathrm{loc}}(i-1)}{4} \tag{4.17}$$

as done e.g. in eq. (53) of [39]. While this averaging does not provide a relevant improvement for (4.15) in A, it becomes important for (4.16) in B.

JHEP02(2026)224

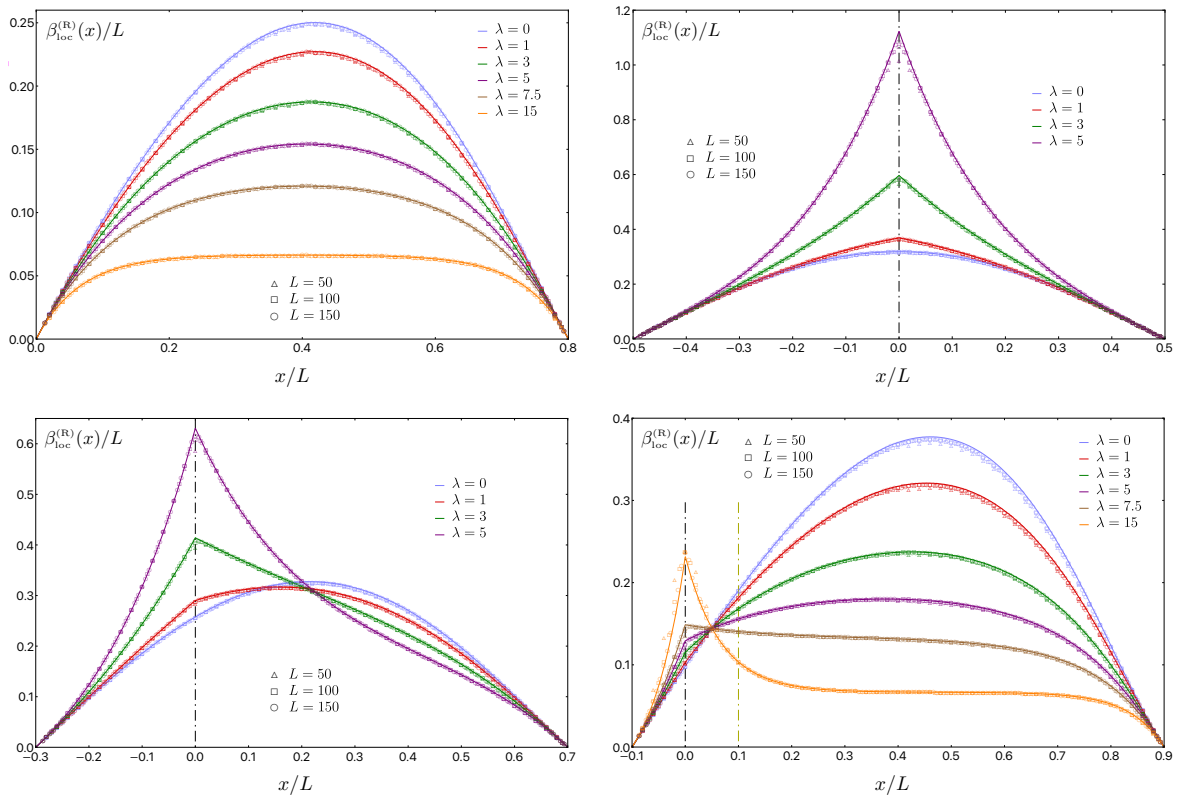

Figure 6. Weight function of the local term in A for the rainbow chain, obtained through (4.15) and (4.17), for a configuration of type (a) (top left), (b) (top right) and (c) (bottom panels). The solid lines correspond to the analytic expression for $\beta^{(\mathrm{R})}_{\mathrm{loc}}(x)$, given in (3.38)–(3.39). The vertical dash-dotted yellow line in the bottom right panel identifies A_*.

In figure 6 we compare the data points in A obtained numerically through (4.15) and (4.17) against the analytic expression for the weight function $\beta^{(\mathrm{R})}_{\mathrm{loc}}(x)$ reported in (3.38)–(3.39), which provides the solid lines. In the top left panel, top right panel and bottom panels, the bipartitions of type (a), (b) and (c) have been considered, respectively. The results corresponding to the bipartition of type (d) have not been reported because they are qualitatively analogous to the ones for a bipartition of type (a). As L increases, a remarkable agreement is observed between the data points obtained from the numerical calculations on the lattice and the corresponding analytic expression found in the continuum. The cusp of $\beta^{(\mathrm{R})}_{\mathrm{loc}}(x)$ at $x = 0$ is also nicely observed through the lattice data points. For large inhomogeneity, the convergence to the expected curve is faster away from the singularity and slower around the singularity (see e.g. the data points having $\lambda = 15$ in the bottom right panel of figure 6). When $a < 0 < b$, the vertical dash-dotted black line corresponds to $x = 0$, where, from (3.38), we find that

$$\frac{\beta^{(\mathrm{R})}_{\mathrm{loc}}(0)}{L} = \frac{R_\lambda(1)\,(\tilde{b}_L^2 - 1)(1 - \tilde{a}_L^2)}{\pi(\tilde{b}_L - \tilde{a}_L)(\tilde{a}_L\,\tilde{b}_L + 1)} \tag{4.18}$$

which becomes the global maximum of the solid curve at large λ, and diverges as $\lambda \to +\infty$.

JHEP02(2026)224

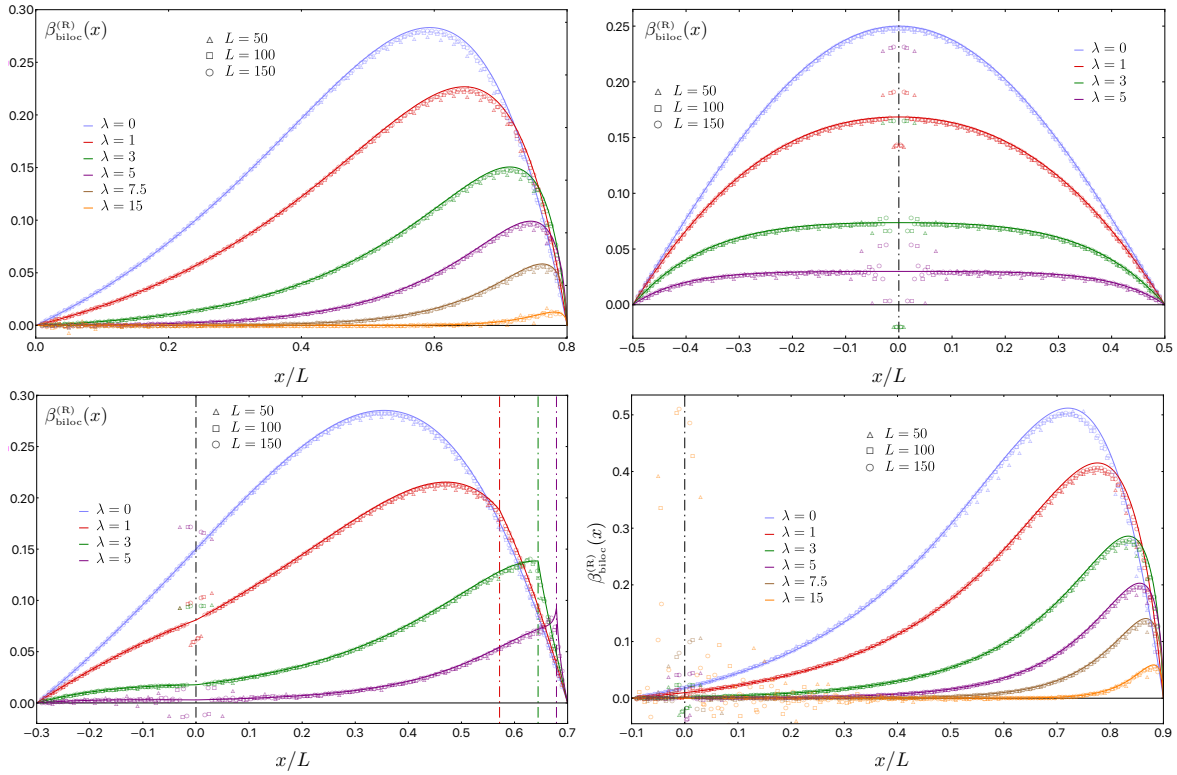

Figure 7. Weight function of the bilocal term in A for the rainbow chain, obtained from (4.19) and (4.20), for the same configurations considered in figure 6. The solid lines correspond to the analytic expression for $\beta^{(\mathrm{R})}_{\mathrm{biloc}}(x)$, given in (3.41). In the bottom left panel, the vertical dash-dotted coloured lines correspond to (3.42).

The most interesting feature to highlight in figure 6 is the plateau with height $1/h$ occurring in A_* (see the text above (3.50)) when λ is large. Although the expression (3.50) for the plateau is derived for $\lambda \to +\infty$, our numerical results for $\lambda = 15$ (see the top left and bottom right panels of figure 6) already display a plateau of height $1/h$ in a proper subset of A_*. We remind that A_*, which is identified by the vertical dash-dotted yellow line at $x = -a$ in the bottom right panel, is given by $A_* = (|a|, b)$ in the bottom panels, and by $A_* = (a, b)$ in the top left panel. Instead, $A_* = \emptyset$ in the top right panel. This plateau in the weight function of the local term combined with the contour function (3.44) explains the scaling of $S_A^{(n)}$ as the length of A_* (see the corresponding discussion in section 3.2, and figure 3). In the regime of large inhomogeneity, besides the plateau, the exponential behaviour discussed in section 3.2 for the analytic expressions is confirmed by the numerical data points. At any value of the inhomogeneity parameter, the linear behaviour of $\beta^{(\mathrm{R})}_{\mathrm{loc}}(x)$ close to the endpoints of A is nicely captured by the lattice data.

The case $\lambda = 0$ corresponds to the results obtained in section 2. Indeed, in figure 6 the weight function of the local term given in (2.22)–(2.23) has been employed (see the solid blue lines).

For the special case of A adjacent to the boundary, these observations have been made also in [10], where a different method has been used to obtain the data points for the rainbow

JHEP02(2026)224

chain. It would be insightful to compare in a more systematic way these two methods employed to study the weight function of the local term.

The weight function of the bilocal term found in section 3.2 for the rainbow model (see (3.41)) can be obtained through a continuum limit procedure similar to the one described above for the weight function of the local term. In particular, let us consider the combination of matrix elements introduced in [39], namely

$$\beta^{(\mathrm{R})}_{\mathrm{biloc}}(i) = \frac{1}{2\pi} \sum_{j \in A} \cos\big[\pi(j+i)/2\big]\, K_{i,j} \tag{4.19}$$

and also the corresponding average analogous to (4.17), namely

$$\bar{\beta}^{(\mathrm{R})}_{\mathrm{biloc}}(i) \equiv \frac{\beta^{(\mathrm{R})}_{\mathrm{biloc}}(i)}{2} + \frac{\beta^{(\mathrm{R})}_{\mathrm{biloc}}(i+1) + \beta^{(\mathrm{R})}_{\mathrm{biloc}}(i-1)}{4}\,. \tag{4.20}$$

This averaging plays a crucial role in obtaining a good agreement with the analytic expression (3.41) in the continuum, like the averaging (4.17) for (4.16) in the case of the local term.

In figure 7 we have reported the data points obtained from (4.19) and (4.20), for the same configurations considered in figure 6. As L increases, we observe a remarkable agreement between the numerical data points from the lattice and the solid curves provided by the analytic expression for $\beta^{(\mathrm{R})}_{\mathrm{biloc}}(x)$, given in (3.41). The vertical dash-dotted black line indicates the curvature singularity at $x = 0$ (see the text below (3.32)), whenever it is contained in A, while the vertical dash-dotted coloured lines in the bottom left panel correspond to $x = x_{\mathrm{c,R}}(0)$ (see (3.42)), which depends on λ. These lines also show the positions of the singular points of the weight functions. Indeed, because of the curvature singularity at $x = 0$ of the inhomogeneous background, the weight function $\beta^{(\mathrm{R})}_{\mathrm{biloc}}(x)$ exhibits a cusp singularity not only at $x = 0$ (like $\beta^{(\mathrm{R})}_{\mathrm{loc}}(x)$), but also at its conjugate point $x = x_{\mathrm{c,R}}(0)$, as a consequence of the bilocal nature of the bipartite entanglement in this setup. Notice that the weight functions are regular for the homogeneous background. Also the linear behaviour close to the entangling points (see (3.26)–(3.27)) is nicely captured by the numerical data points. However, the singular behaviour of $\beta^{(\mathrm{R})}_{\mathrm{biloc}}(x)$ at $x = 0$ is not captured by the lattice data points for the values of L that we have considered. Nonetheless, notice that the support of the oscillations around $x = 0$ decreases as L increases. We remark the vanishing of $\beta^{(\mathrm{R})}_{\mathrm{biloc}}(x)$ in the regime of large inhomogeneity, as shown in (3.58). For the bipartitions of type (b), where $a = -b$ with $b > 0$ (see the top right panel in figure 7), we have that $x_{\mathrm{c,R}}(0) = 0$, i.e. the two singular points coincide, and, as a consequence, $\beta^{(\mathrm{R})}_{\mathrm{biloc}}(x)$ is smooth at $x = 0$ (see the discussion below (3.43)). In this case, a plateau occurs in the regime of large inhomogeneity, whose height is given by (3.57).

The case $\lambda = 0$ corresponds to the results obtained in section 2. Indeed, the solid blue lines in figure 7 are obtained from the analytic expression of the weight function of the bilocal term given in (2.29), (2.31) or (2.32).

Besides the two weight functions $\beta^{(\mathrm{R})}_{\mathrm{loc}}(x)$ and $\beta^{(\mathrm{R})}_{\mathrm{biloc}}(x)$, we also find it worth exploring the contour functions of the entanglement entropies in the rainbow chain. We consider $\mathcal{C}_A(i)$ and $\mathcal{C}^{(n)}_A(i)$ in (4.10), and we compare the numerical data from the rainbow chain with the analytic expressions of $C^{(n)}_{A;(\mathrm{R})}(x)$ and $C^{(n)}_{A,B;(\mathrm{R})}(x)$, defined in (3.44) and (3.45) respectively.

JHEP02(2026)224

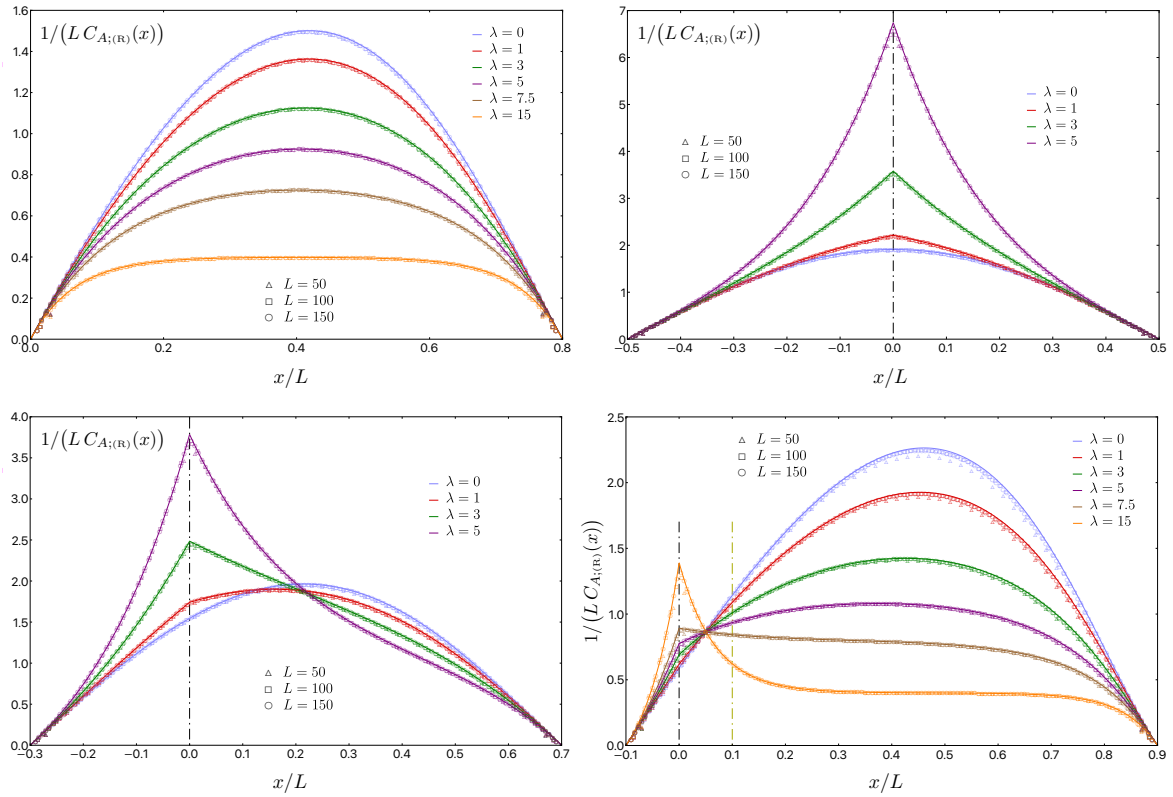

Figure 8. Contour function for the entanglement entropy in A for the rainbow chain, obtained from (4.10) and (4.21), for the same configurations considered in figure 6 and figure 7. The solid lines correspond to the analytic expression of $C_{A;(\mathrm{R})}(x)$, given by (3.44) for $n = 1$.

As done in (4.17) and (4.20) for the weight functions, also for the contour functions for the entanglement entropy and for the Rényi entropies in A it is worth introducing an averaging procedure that allows to obtain a more precise agreement with the analytic results in the continuum. In particular, we consider the combinations given respectively by

$$\bar{\mathcal{C}}_A(i) \equiv \frac{\mathcal{C}_A(i)}{2} + \frac{\mathcal{C}_A(i+1) + \mathcal{C}_A(i-1)}{4} \tag{4.21}$$

and

$$\bar{\mathcal{C}}_A^{(n)}(i) \equiv \frac{\mathcal{C}_A^{(n)}(i)}{2} + \frac{\mathcal{C}_A^{(n)}(i+1) + \mathcal{C}_A^{(n)}(i-1)}{4} \tag{4.22}$$

which can be extended to the complementary region B in a straightforward way.

In the case of the contour function for the entanglement entropy, the results of our numerical analysis for (4.10) and (4.21) in A are reported in figure 8, where the same configurations explored in figure 6 and figure 7 have been considered. Since the solid curves are proportional to those occurring in figure 6, the same qualitative observations can be easily adapted to this contour function. However, we find it worth highlighting the remarkable agreement between the analytic expressions (solid curves) and the numerical data points as L increases in this analysis. The case $\lambda = 0$ (solid blue lines and blue data points) provides the result (2.41) for the contour function in the homogeneous background. It is instructive to

JHEP02(2026)224

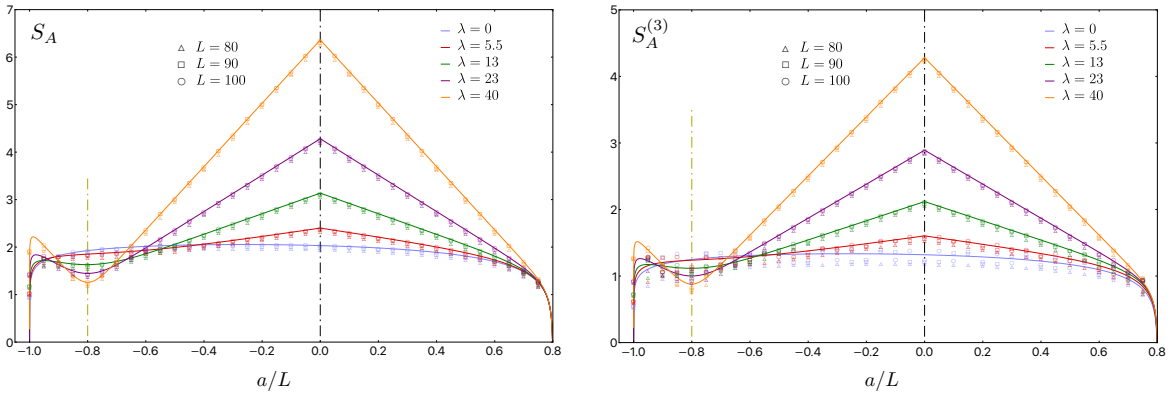

Figure 9. Entanglement entropy (left) and Rényi entropy with $n = 3$ (right) for the rainbow chain, obtained through (4.6). The solid lines are given by (3.46) combined with (4.23).

explain the features of the entanglement entropies through the behaviour of their contour functions $C^{(n)}_{A;(\mathrm{R})}(x)$ in (3.44). For instance, the logarithmic divergence in S_A originates from the behaviour of $\beta^{(\mathrm{R})}_{\mathrm{loc}}(x)$ close to the entangling points, which is given by (3.24) and (3.25).

The entanglement entropies in the rainbow chain have been largely explored in the literature [10–13, 15] through (4.6), extending the results obtained in homogeneous fermionic chains in the presence of boundaries (see e.g. [85–89]). In the rainbow model, by also employing the results of [90–93], it has been found [15] that the entanglement entropies of an interval A in a generic position are (3.46) with the $O(1)$ term given by the constant $\mathfrak{C}_n$ defined as follows

$$\mathfrak{C}_n \equiv \left(1+\frac{1}{n}\right)\left\{\frac{\log(2)}{6}+\int_0^\infty\left[\frac{n^2}{n^2-1}\left(\frac{1}{n\,\sinh(t/n)}-\frac{1}{\sinh(t)}\right)\frac{1}{\sinh(t)}-\frac{\mathrm{e}^{-2t}}{6}\right]\frac{\mathrm{d}t}{t}\right\}. \tag{4.23}$$

Our numerical results for the entanglement entropy and for the Rényi entropy with $n = 3$ in the rainbow chain (for $b = 0.8\,L$ and $a \in [-L, b)$) are reported in the left and right panel of figure 9 respectively, for various values of λ. The data points for $\lambda = 0$ are obtained in the homogeneous free fermionic chain, and the corresponding expressions in the continuum limit are discussed in section 2. The solid curves correspond to the analytic expressions for the rainbow model in the continuum, given by (3.46) and (4.23) with UV cutoff ϵ set to 1. The vertical dash-dotted black and yellow lines indicate $x = 0$ and $x = -b$ respectively. For the symmetric case where $a = -b$ with $b > 0$ (i.e. the configuration (b) in figure 2), we refer the reader to the results in [15]. In the regime of large inhomogeneity, agreement is found with (3.60). We remark that subleading oscillatory terms occur in the numerical data points for $S^{(n)}_A$ with $n \neq 1$, and are more visible for small values of λ, as also observed in [15]. It would be very interesting to find analytic expressions for these subleading oscillatory terms.

Since the system that we are considering is defined on a segment, both the interval A and its complement B have finite volume. Let us stress again that B is made by two disjoint blocks when A is separated from the boundaries of the segment. While in the previous analyses the various entanglement quantifiers have been considered only in A, in the following we explore them also in B. Since the purity of the ground state guarantees that $S^{(n)}_A = S^{(n)}_B$, it is not useful to consider the entanglement entropies of B. On the contrary, the other

JHEP02(2026)224

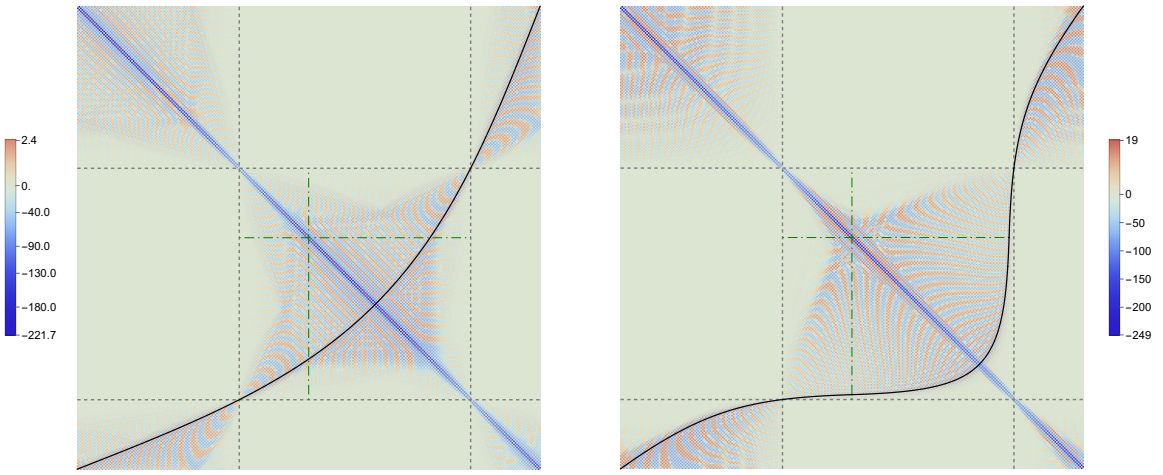

Figure 10. Matrix elements characterising the entanglement Hamiltonian of A and B (see (4.12) for A and the analogous formula for B, where C_A is replaced by C_B). The bipartition is a configuration of type (c) (see figure 2) with $a = -0.3\,L$ and $b = 0.7\,L$, and it is made by $L_A = L_B = 150$ sites. Here, either $\lambda = 0$ (left) or $\lambda = 5$ (right). The black solid curve indicates the position of the conjugate point (3.40). See also the top left and bottom left panel of figure 5, corresponding to the central block of the left and right panel respectively.

quantities that we investigated exhibit interesting properties in B. The contour functions for the entanglement entropies in B can be studied by replacing C_A with C_B (introduced in the text below (4.7)) in the analysis performed above for A. As for the weight functions (2.9) and (2.10) for the interval in the half line, which play a crucial role in our analysis and have been derived in [29] for the interval $\hat{A}$, it is not obvious that their extension to the complement of $\hat{A}$ in the half line (that is not connected) provides the correct weight functions for the entanglement Hamiltonian in this subsystem. In the following we provide some numerical evidence supporting this assumption.

In the numerical analyses of the entanglement quantifiers in A for the rainbow chain, we have always studied subsystems having $L_A \leqslant L$ because of the occurrence of vanishing eigenvalues when $L_A > L$. The same observation holds for B. Hence, in order to avoid vanishing eigenvalues in the entanglement spectrum either in A or in B, in the following we consider bipartitions having $L_A = L_B = L$.

Let us briefly discuss here the sign of the weight functions as x varies in the whole segment. The analytic expressions of $\beta^{(\mathrm{R})}_{\mathrm{loc}}(x)$ and $\beta^{(\mathrm{R})}_{\mathrm{biloc}}(x)$ (see (3.38)–(3.39) and (3.41) respectively) vanish only at the entangling points and they are positive in A and negative in B. The combinations of matrix elements introduced in (4.15)–(4.17) and in (4.19)–(4.20) allow us to explore the continuum limit of the weight functions of the local and bilocal term respectively. Since these combinations provide positive results, in the following the numerical data points from the rainbow chain are compared with $|\beta^{(\mathrm{R})}_{\mathrm{loc}}(x)|$ and $|\beta^{(\mathrm{R})}_{\mathrm{biloc}}(x)|$.

In figure 10 we show the elements of the matrices given by (4.12) for A and by the analogous formula for B, where C_A is replaced by C_B. The dashed grey lines separate the central block corresponding to A (shown in figure 4 and figure 5) from the other ones. The blocks corresponding to B are the ones whose elements are labelled by position indices that

JHEP02(2026)224

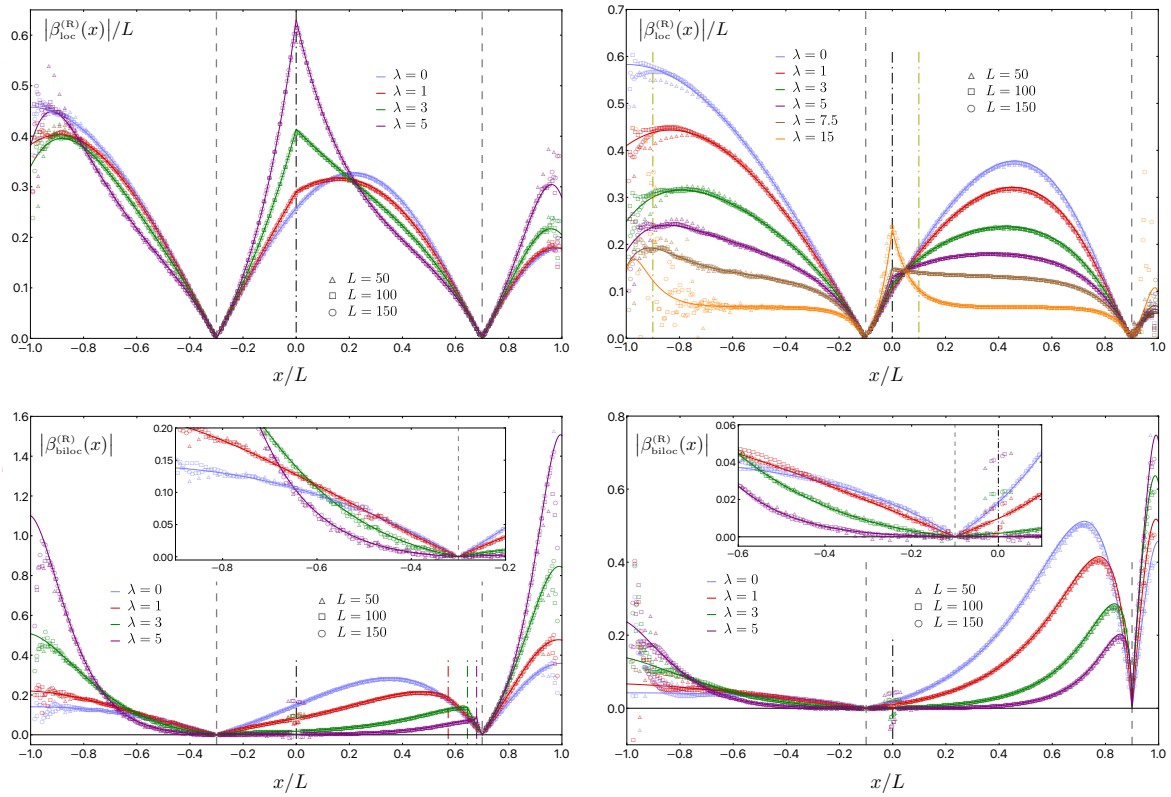

Figure 11. Weight functions of the local (top) and bilocal (bottom) term in $A \cup B$ for the rainbow chain, obtained by employing (4.15)–(4.17) and (4.19)–(4.20) respectively, also in B. The configurations (of type (c)) are the same ones considered in the bottom panels of figure 6 and figure 7. The solid lines correspond to the analytic expressions for $|\beta^{(\mathrm{R})}_{\mathrm{loc}}|/L$ and $|\beta^{(\mathrm{R})}_{\mathrm{biloc}}|$ (see (3.38)–(3.39) and (3.41) respectively). The insets zoom in on the region around the first entangling point.

both belong to B. The remaining blocks, whose elements have one index in A and the other one in B, have been filled with zeros. The dash-dotted green lines indicate the centre of the segment, where the singularity is located, like in figure 5. The choice of the bipartition and of the inhomogeneity parameter, described in the caption of figure 10, implies that the central block in the left and right panel coincides with the top left and bottom left panel of figure 5 respectively. As we saw for A in figure 4 and figure 5, also in B the largest elements are located on the odd diagonals around the main diagonal. The position of the conjugate point (3.40) corresponds to the black solid curve in figure 10, and it nicely captures a front of the off-diagonal matrix elements associated with A and with B. The effect of the inhomogeneity on the matrix elements of K in (4.12), both for A and for B, can be observed by comparing the two panels in figure 10. Note that, while for $x \in A$ the conjugate point (3.40) tends to b as the inhomogeneity grows, for $x \in B$ we have $x_{\mathrm{c,R}}(x) \to -x$ as $\lambda \to \infty$ (see (3.55) and figure 10).

Regarding the weight functions of the entanglement Hamiltonian, in figure 11 we have reported some results obtained by extending to B the expressions in (4.15)–(4.17) for the local term (top panels) and in (4.19)–(4.20) for the bilocal term (bottom panels), which have been previously employed for A. In particular, in the top panels, the best agreement

JHEP02(2026)224

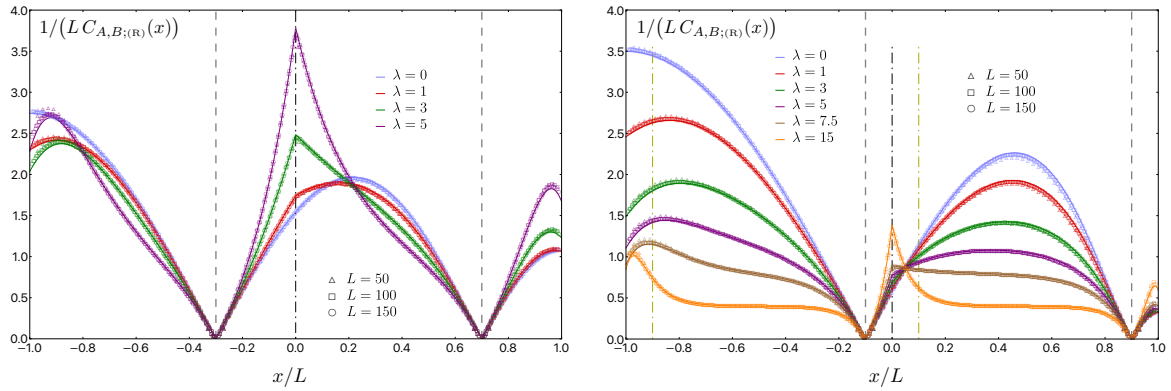

Figure 12. Contour function for the entanglement entropy in $A \cup B$ for the rainbow chain, obtained from (4.10) and (4.21) in A and their straightforward extension to B, for the configurations considered in figure 11. The results in A are the ones in the bottom panels of figure 8. The solid lines are provided by the analytic expression of $C_{A,B;(\mathrm{R})}(x)$, given by (3.45) for $n = 1$.

between the data points and the analytic predictions for the local term has been obtained by employing (4.15) with (4.17) in A and (4.16) with (4.17) in B. Notice that the configurations of type (c) (see figure 2) considered in the left and right panels of figure 11 are the same ones analysed in the bottom panels of figure 6 and figure 7; hence the same colour code has been adopted. The vertical dashed grey lines correspond to the entangling points at $x = a$ and $x = b$, while the vertical dash-dotted black line denotes the centre of the segment. The dash-dotted yellow lines in the top right panel identify A_* and B_*, and the coloured dash-dotted lines in the bottom left panel have been already introduced in the bottom left panel of figure 7. The solid lines in the top and bottom panels are given respectively by $|\beta^{(\mathrm{R})}_{\mathrm{loc}}|/L$ from (3.38)–(3.39) and by $|\beta^{(\mathrm{R})}_{\mathrm{biloc}}|$ from (3.41), which are functions of x/L. The curves and the data points for $\lambda = 0$ correspond to the homogeneous case considered in section 2. The agreement between the data points from the rainbow chain as L increases and the analytic curves for $|\beta^{(\mathrm{R})}_{\mathrm{loc}}|/L$ and $|\beta^{(\mathrm{R})}_{\mathrm{biloc}}|$ is very satisfactory (see also the insets in figure 11, that highlight the nice collapse of the data on the solid curves around the first entangling point), except for the regions close the boundaries of the segment, where the support of the unstable behaviour of the data points should vanish for larger values of L. We find it worth remarking that in the regime of large inhomogeneity, the expected plateau given by (3.50) is observed also in B_* for large enough values of λ (see also the bottom left panel of figure 3), as shown e.g. in the top right panel of figure 11 for $\lambda = 15$.

We find it very instructive to also consider the contour functions for the entanglement entropies of the rainbow chain in the entire segment. These quantities have been obtained by using (4.10), (4.21) and (4.22) in A (see figure 8 for the $n = 1$ case), and here we employ the analogous expressions adapted to B in a straightforward way, as previously discussed. In the continuum limit, (3.45) is the natural candidate for these quantities, for a generic value of the Rényi index. In figure 12 we show the contour function for the entanglement entropy in the case of the configurations already considered in figure 11 (also the same colour code has been employed); hence, in A the data points coincide with the ones reported in the bottom panels of figure 8. The agreement between the data points for the rainbow

JHEP02(2026)224

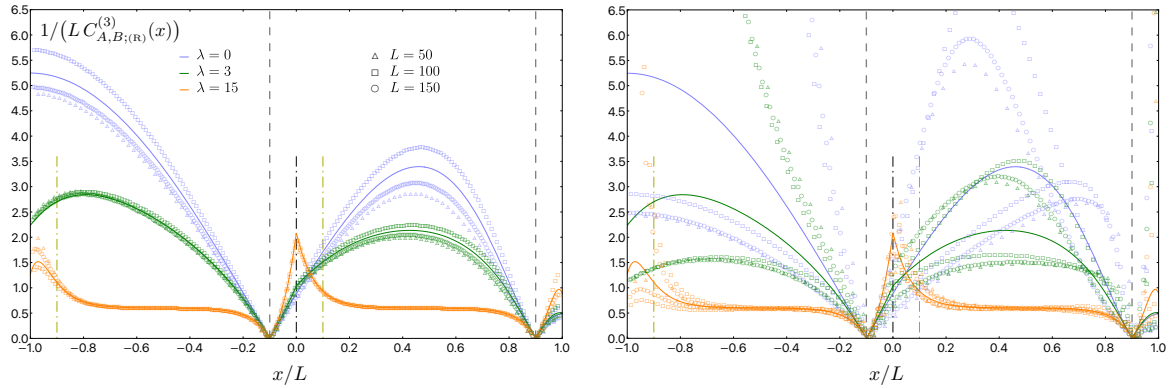

Figure 13. Contour function for the Rényi entropy with $n = 3$ in $A \cup B$ for the rainbow chain, for the same configuration considered in the right panel of figure 12. The quantities $\bar{\mathcal{C}}^{(3)}_A(i)$ (see (4.22)) and $\mathcal{C}^{(3)}_A(i)$ (see (4.10)) for $i \in A \cup B$ are shown in the left and right panel respectively. The solid lines correspond to the analytic expression in (3.45) for $n = 3$.

chain and the analytic expression for $C_{A,B;(\mathrm{R})}(x)$ (i.e. (3.45) for $n = 1$) is excellent along the entire segment. Notice that the oscillations of the data points observed in the top panels of figure 11 close to the endpoints of the segment for the weight function of the local term do not occur for the contour function of the entanglement entropy. We remark that the average (4.21) plays a crucial role in finding such remarkable agreement with the analytic expressions in the continuum. Indeed, in the results for the contour function reported in [10] for the case of a block adjacent to the boundary (where (4.21) was not employed), oscillations are observed in the vicinity of the boundary.

The crucial role of the averaging procedure given by (4.21) and (4.22) is evident when the contour functions of the Rényi entropies are considered. In figure 13 we report our numerical data points for the contour function of the Rényi entropy with $n = 3$. In particular, in the left and right panel of this figure we show $\bar{\mathcal{C}}^{(3)}_A(i)$ (see (4.22)) and $\mathcal{C}^{(3)}_A(i)$ (see (4.10)) respectively, extended to the entire segment in the straightforward way. The bipartition is the same one considered in the right panel of figure 12 to facilitate the comparison with the $n = 1$ case. This gives some insights into the n-dependence of the contour functions for the entanglement entropies. Large oscillations occur in the data points for $\mathcal{C}^{(n)}_A(i)$ with $n \neq 1$, whose amplitude significantly increases with n, especially in the regions close to the boundaries of the segment. This has been observed also in figure 11 of [10] for the case of a block adjacent to the boundary. By comparing the two panels of figure 13, it is evident that the averaging procedure introduced in (4.22) leads to a significant improvement in finding agreement with the analytic expression (3.45). For both $\mathcal{C}^{(n)}_A(i)$ and $\bar{\mathcal{C}}^{(n)}_A(i)$, the oscillations increase towards the boundaries and for increasing values of n, but they are suppressed as the inhomogeneity grows. Indeed, the largest oscillations are observed in the homogeneous case. It would be very insightful to find analytic results for these oscillations.

5 Conclusions

In this paper we studied the entanglement Hamiltonian and the contour functions for the entanglement entropies of an interval A for the massless Dirac field on a segment with an

JHEP02(2026)224

inhomogeneous background and in the ground state. The class of spatially inhomogeneous backgrounds (3.1) was explored, and the same boundary condition was imposed at both endpoints of the segment. The position of the interval A in the segment is generic (see figure 1). The analytic results for these quantities are given in section 2 for the homogeneous case and in section 3.1 for a generic background. The latter expressions have been specialised to the rainbow model in section 3.2, and in section 4 they have been checked against the continuum limit of the corresponding exact numerical results in the rainbow chain (4.2), for the configurations in figure 2. In the limit where A is adjacent to the boundary, the results of [10] are recovered.

The massless Dirac field on a segment is a BCFT with $c = 1$. Since the same boundary condition is imposed at both endpoints, we have employed the entanglement Hamiltonian of an interval in the half line found in [29]. Our results for the homogeneous case are discussed in section 2. Combining the conformal map (2.11) with the weight functions found in [29], we have obtained the entanglement Hamiltonian (2.21) with the weight functions (2.22)–(2.23) and (2.29) (or (2.31) or (2.32) equivalently) for the local and bilocal term respectively. From the weight function of the local term, we have obtained the contour function for the entanglement entropies in A and in the entire segment (see (2.41) and (2.45) respectively). The corresponding entanglement entropies are reported in (2.44).

These analytic results for the homogeneous case have been employed to find the same quantities for the class of inhomogeneous backgrounds defined by (3.1). In particular, the entanglement Hamiltonian of the interval is (3.4), where the weight functions are given by either (3.5) or (3.7) for the local term and by (3.11)–(3.12) for the bilocal term. In the case of these inhomogeneous backgrounds, we have written a candidate expression for the contour functions for the entanglement entropies by employing the weight function of the local term (see (3.17) in A and (3.22) in the entire segment). This provides the expression (3.21) for the entanglement entropies, first found in [15] through the twist fields method.

In the second part of the paper, our analytic results have been specialised to the rainbow model (see section 3.2 and section 4), whose Weyl factor is given by (3.32). In this model, the weight functions for the local and bilocal term become (3.38) (or equivalently (3.39)) and (3.41) respectively. Considering the bipartition in figure 1 of the rainbow chain (4.2) in its ground state, in section 4 we studied the continuum limit of the entanglement Hamiltonian and of the contour functions for the entanglement entropies, finding a remarkable agreement with the analytic expressions obtained in section 3.2. The matrix (4.12) determining the entanglement Hamiltonian (4.11) on the lattice displays the inhomogeneous and the non-local nature of this operator, as shown in figure 4 and figure 5 for A and in figure 10 for the entire segment. The method that we have employed to study the continuum limit is based on the analysis performed in [39] for entanglement Hamiltonians in homogeneous fermionic chains (either on the line or on the half line), which contain also a bilocal term. Our numerical results for the weight function of the local and bilocal term are shown in figure 6 and figure 7 respectively, and those for the contour functions and the corresponding entanglement entropies in figure 8 and figure 9 respectively. These quantities have been explored also in the entire segment, obtaining the results reported in figure 11, figure 12 and figure 13. The agreement between the analytic expressions and the numerical data for these quantities in B provides evidence that the analytic formulas derived in section 2 and section 3 are also valid when

JHEP02(2026)224

$x \in B$. As for the numerical approach to the continuum limit, it would be interesting to further explore the differences between (4.15) and (4.16) for the weight function of the local term in $x \in B$. It would also be insightful to understand why the lattice formula for the contour function for the entanglement entropy captures the CFT prediction in a very nice way, whereas the ones employed for the weight function of the local term display oscillations in B near the boundaries of the segment (see figure 12 and the top panels of figure 11).

Our results confirm the interesting relation between the reduced density matrix of some bipartitions obtained from the ground state of the rainbow chain in the regime of large inhomogeneity and the density matrix of a thermal state in the subsystem [11–13, 15] (see figure 3). Indeed, the weight function of the local term can develop a plateau (3.50) in this regime, as observed in bottom right panels of figure 6 and figure 8, in the top right panel of figure 11, and in the right panels of figure 12 and figure 13. Interestingly, the weight function of the bilocal term can also display a plateau in the regime of large inhomogeneity (see e.g. (3.57) and the top right panel of figure 7), which however does not admit a thermal interpretation, as discussed in section 3.2. In figure 13, where the contour function for the Rényi entropy with $n = 3$ is considered, the improvement provided by the averaging defined in (4.22) is highlighted. The same figure shows the relevant role played by oscillatory terms in the lattice data points, and it would be insightful to describe them analytically. We remark that the numerical methods employed in this work and in [10] are qualitatively different; hence, it could be interesting to perform a systematic comparison between them.

The results discussed in this work suggest various directions for future studies.

It would be interesting to apply the method discussed in [36–39, 83, 84] to study the entanglement Hamiltonians in other inhomogeneous free models [21, 54, 94–115], considering with particular attention the entanglement Hamiltonians that contain also non-local terms [26–30, 116–120] and the limiting regimes where they become local. The extension of these analyses to interacting models would be of great relevance (see e.g. the numerical results in [121]). In the case of free fermionic chains, it is important to explore also the role played by the filling parameter in the entanglement Hamiltonian (see e.g. [39, 50]). In these setups, it would also be worth investigating other interesting quantities related to the entanglement Hamiltonian. These include e.g. the entanglement spectra [9, 35, 77–80, 122–128], important measures of bipartite entanglement in mixed states such as the logarithmic negativity [129–141], and other quantities probing various features of entanglement [25, 50, 142, 143]. The latter class includes also alternative expressions for the spatial density of the entanglement entropy, like e.g. the one discussed in [144]. The aforementioned entanglement Hamiltonians containing non-local terms should be explored also in more complicated models (see e.g. [145–152] for the entanglement entropies). It is important to study entanglement Hamiltonians for inhomogeneous models also in higher dimensions [13, 23, 100, 153–157] and in out of equilibrium scenarios [9, 158–164]. Finally, pivotal insights could arise from the analysis of entanglement Hamiltonians and related quantities in the context of the gauge/gravity correspondence (see e.g. [165–174]).

Acknowledgments

It is our pleasure to thank Viktor Eisler, Mihail Mintchev and Javier Rodríguez-Laguna for useful discussions. We are especially grateful to Sara Pasquetti for insightful conversations

JHEP02(2026)224

and thoughtful mentorship of ST during his master's thesis project. ET acknowledges the Isaac Newton Institute (Cambridge) for hospitality and financial support during the last part of this work, within the program *Quantum field theory with boundaries, impurities, and defects*. This work was funded by the European Union — NextGenerationEU, Mission 4, Component 2, Inv.1.3, in the framework of the PNRR Project National Quantum Science and Technology Institute (NQSTI) PE00023; CUP: G93C22001090006. The project that gave rise to these results received the support of a fellowship from "la Caixa" Foundation (ID 100010434), awarded to ST, with code LCF/BQ/DI24/12070002.

Data Availability Statement. This article has no associated data or the data will not be deposited.

Code Availability Statement. This article has no associated code or the code will not be deposited.

References

[1] R. Haag, *Local Quantum Physics*, Springer Berlin Heidelberg (1996) [DOI:10.1007/978-3-642-61458-3_3].

[2] H. Casini and M. Huerta, *Entanglement entropy in free quantum field theory*, *J. Phys. A* **42** (2009) 504007 [arXiv:0905.2562] [INSPIRE].

[3] V. Eisler and I. Peschel, *Reduced density matrices and entanglement entropy in free lattice models*, *J. Phys. A* **42** (2009) 504003 [arXiv:0906.1663] [INSPIRE].

[4] J.J. Bisognano and E.H. Wichmann, *On the Duality Condition for a Hermitian Scalar Field*, *J. Math. Phys.* **16** (1975) 985 [INSPIRE].

[5] J.J. Bisognano and E.H. Wichmann, *On the Duality Condition for Quantum Fields*, *J. Math. Phys.* **17** (1976) 303 [INSPIRE].

[6] P.D. Hislop and R. Longo, *Modular Structure of the Local Algebras Associated With the Free Massless Scalar Field Theory*, *Commun. Math. Phys.* **84** (1982) 71 [INSPIRE].

[7] H. Casini, M. Huerta and R.C. Myers, *Towards a derivation of holographic entanglement entropy*, *JHEP* **05** (2011) 036 [arXiv:1102.0440] [INSPIRE].

[8] G. Wong, I. Klich, L.A. Pando Zayas and D. Vaman, *Entanglement Temperature and Entanglement Entropy of Excited States*, *JHEP* **12** (2013) 020 [arXiv:1305.3291] [INSPIRE].

[9] J. Cardy and E. Tonni, *Entanglement hamiltonians in two-dimensional conformal field theory*, *J. Stat. Mech.* **1612** (2016) 123103 [arXiv:1608.01283] [INSPIRE].

[10] E. Tonni, J. Rodríguez-Laguna and G. Sierra, *Entanglement hamiltonian and entanglement contour in inhomogeneous 1D critical systems*, *J. Stat. Mech.* **1804** (2018) 043105 [arXiv:1712.03557] [INSPIRE].

[11] G. Vitagliano, A. Riera and J.I. Latorre, *Violation of area-law scaling for the entanglement entropy in spin 1/2 chains*, *New J. Phys.* **12** (2010) 113049 [arXiv:1003.1292] [INSPIRE].

JHEP02(2026)224

[12] G. Ramírez, J. Rodríguez-Laguna and G. Sierra, *From conformal to volume-law for the entanglement entropy in exponentially deformed critical spin 1/2 chains*, arXiv:1407.3456 [DOI:10.1088/1742-5468/2014/10/P10004] [INSPIRE].

[13] G. Ramírez, J. Rodríguez-Laguna and G. Sierra, *Entanglement over the rainbow*, *J. Stat. Mech.* **1506** (2015) P06002 [arXiv:1503.02695] [INSPIRE].

[14] J. Rodríguez-Laguna, S.N. Santalla, G. Ramírez and G. Sierra, *Entanglement in correlated random spin chains, RNA folding and kinetic roughening*, arXiv:1601.03408 [DOI:10.1088/1367-2630/18/7/073025] [INSPIRE].

[15] J. Rodríguez-Laguna et al., *More on the rainbow chain: entanglement, space-time geometry and thermal states*, *J. Phys. A* **50** (2017) 164001 [arXiv:1611.08559] [INSPIRE].

[16] M. Campostrini and E. Vicari, *Critical behavior and scaling in trapped systems*, *Phys. Rev. Lett.* **102** (2009) 240601 [arXiv:0903.5153] [INSPIRE].

[17] M. Campostrini and E. Vicari, *Equilibrium and off-equilibrium trap-size scaling in one-dimensional ultracold bosonic gases*, *Phys. Rev. A* **82** (2010) 063636 [arXiv:1010.0806].

[18] M. Campostrini and E. Vicari, *Quantum critical behavior and trap-size scaling of trapped bosons in a one-dimensional optical lattice*, *Phys. Rev. A* **81** (2010) 063614 [arXiv:1003.3334].

[19] M. Campostrini and E. Vicari, *Scaling of bipartite entanglement in one-dimensional lattice systems with a trapping potential*, *J. Stat. Mech.* **1008** (2010) P08020 [arXiv:1005.3150] [INSPIRE].

[20] J. Dubail, J.-M. Stéphan, J. Viti and P. Calabrese, *Conformal field theory for inhomogeneous one-dimensional quantum systems: the example of non-interacting Fermi gases*, *SciPost Phys.* **2** (2017) 002 [arXiv:1606.04401] [INSPIRE].

[21] V. Eisler and D. Bauernfeind, *Front dynamics and entanglement in the XXZ chain with a gradient*, *Phys. Rev. B* **96** (2017) 174301 [arXiv:1708.05187] [INSPIRE].

[22] M. Lewenstein, A. Sanpera and V. Ahufinger, *Ultracold Atoms in Optical Lattices: Simulating quantum many-body systems*, Oxford University Press (2012) [DOI:10.1093/acprof:oso/9780199573127.001.0001].

[23] O. Boada, A. Celi, J.I. Latorre and M. Lewenstein, *Dirac Equation For Cold Atoms In Artificial Curved Spacetimes*, *New J. Phys.* **13** (2011) 035002 [arXiv:1010.1716] [INSPIRE].

[24] J. Rodríguez-Laguna, L. Tarruell, M. Lewenstein and A. Celi, *Synthetic Unruh effect in cold atoms*, *Phys. Rev. A* **95** (2017) 013627 [arXiv:1606.09505] [INSPIRE].

[25] B. Mula, S.N. Santalla and J. Rodríguez-Laguna, *Casimir forces on deformed fermionic chains*, *Phys. Rev. Res.* **3** (2021) 013062 [arXiv:2004.12456] [INSPIRE].

[26] H. Casini and M. Huerta, *Reduced density matrix and internal dynamics for multicomponent regions*, *Class. Quant. Grav.* **26** (2009) 185005 [arXiv:0903.5284] [INSPIRE].

[27] D. Blanco and G. Pérez-Nadal, *Modular Hamiltonian of a chiral fermion on the torus*, *Phys. Rev. D* **100** (2019) 025003 [arXiv:1905.05210] [INSPIRE].

[28] P. Fries and I.A. Reyes, *Entanglement Spectrum of Chiral Fermions on the Torus*, *Phys. Rev. Lett.* **123** (2019) 211603 [arXiv:1905.05768] [INSPIRE].

[29] M. Mintchev and E. Tonni, *Modular Hamiltonians for the massless Dirac field in the presence of a boundary*, *JHEP* **03** (2021) 204 [arXiv:2012.00703] [INSPIRE].

[30] M. Mintchev and E. Tonni, *Modular Hamiltonians for the massless Dirac field in the presence of a defect*, *JHEP* **03** (2021) 205 [arXiv:2012.01366] [INSPIRE].

JHEP02(2026)224

[31] A. Botero and B. Reznik, *Spatial structures and localization of vacuum entanglement in the linear harmonic chain*, *Phys. Rev. A* **70** (2004) 052329 [quant-ph/0403233] [INSPIRE].

[32] G. Vidal and Y. Chen, *Entanglement contour*, *J. Stat. Mech.* **2014** (2014) P10011 [arXiv:1406.1471] [INSPIRE].

[33] A. Coser, C. De Nobili and E. Tonni, *A contour for the entanglement entropies in harmonic lattices*, *J. Phys. A* **50** (2017) 314001 [arXiv:1701.08427] [INSPIRE].

[34] P. Calabrese and J.L. Cardy, *Entanglement entropy and quantum field theory*, *J. Stat. Mech.* **0406** (2004) P06002 [hep-th/0405152] [INSPIRE].

[35] I. Peschel, *Calculation of reduced density matrices from correlation functions*, *J. Phys. A* **36** (2003) L205 [cond-mat/0212631] [INSPIRE].

[36] R. Arias, D. Blanco, H. Casini and M. Huerta, *Local temperatures and local terms in modular Hamiltonians*, *Phys. Rev. D* **95** (2017) 065005 [arXiv:1611.08517] [INSPIRE].

[37] V. Eisler, E. Tonni and I. Peschel, *On the continuum limit of the entanglement Hamiltonian*, *J. Stat. Mech.* **1907** (2019) 073101 [arXiv:1902.04474] [INSPIRE].

[38] G. Di Giulio and E. Tonni, *On entanglement hamiltonians of an interval in massless harmonic chains*, *J. Stat. Mech.* **2003** (2020) 033102 [arXiv:1911.07188] [INSPIRE].

[39] V. Eisler, E. Tonni and I. Peschel, *Local and non-local properties of the entanglement Hamiltonian for two disjoint intervals*, *J. Stat. Mech.* **2208** (2022) 083101 [arXiv:2204.03966] [INSPIRE].

[40] J.L. Cardy, *Conformal Invariance and Surface Critical Behavior*, *Nucl. Phys. B* **240** (1984) 514 [INSPIRE].

[41] J.L. Cardy, *Effect of Boundary Conditions on the Operator Content of Two-Dimensional Conformally Invariant Theories*, *Nucl. Phys. B* **275** (1986) 200 [INSPIRE].

[42] J.L. Cardy, *Boundary Conditions, Fusion Rules and the Verlinde Formula*, *Nucl. Phys. B* **324** (1989) 581 [INSPIRE].

[43] A. Liguori and M. Mintchev, *Quantum field theory, bosonization and duality on the half line*, *Nucl. Phys. B* **522** (1998) 345 [hep-th/9710092] [INSPIRE].

[44] B. Estienne, Y. Ikhlef, A. Rotaru and E. Tonni, *Entanglement entropies of an interval for the massless scalar field in the presence of a boundary*, *JHEP* **05** (2024) 236 [arXiv:2308.00614] [INSPIRE].

[45] P.H. Ginsparg, *Applied conformal field theory*, in the proceedings of the *Les Houches Summer School in Theoretical Physics: Fields, Strings, Critical Phenomena*, Les Houches, France, June 28 – August 05 (1988) [hep-th/9108028] [INSPIRE].

[46] P. Di Francesco, P. Mathieu and D. Sénéchal, *Conformal Field Theory*, Springer New York (1997) [DOI:10.1007/978-1-4612-2256-9].

[47] K. Ohmori and Y. Tachikawa, *Physics at the entangling surface*, *J. Stat. Mech.* **1504** (2015) P04010 [arXiv:1406.4167] [INSPIRE].

[48] N. Samos Sáenz de Buruaga, S.N. Santalla, J. Rodríguez-Laguna and G. Sierra, *Piercing the rainbow state: Entanglement on an inhomogeneous spin chain with a defect*, *Phys. Rev. B* **101** (2020) 205121 [arXiv:1912.10788] [INSPIRE].

[49] G. Ramírez, J. Rodríguez-Laguna and G. Sierra, *Breaking the Area Law: The Rainbow State*, *Springer Proc. Phys.* **239** (2020) 395 [arXiv:1812.11495] [INSPIRE].

JHEP02(2026)224

[50] B. Mula et al., *Depletion in fermionic chains with inhomogeneous hoppings*, *Phys. Rev. B* **106** (2022) 224204 [arXiv:2209.10624] [INSPIRE].

[51] S.N. Santalla et al., *Entanglement links and the quasiparticle picture*, *Phys. Rev. B* **107** (2023) L121114 [arXiv:2208.03766] [INSPIRE].

[52] L. Byles, G. Sierra and J.K. Pachos, *Q-deformed rainbows: a universal simulator of free entanglement spectra*, *New J. Phys.* **26** (2024) 013055 [arXiv:2302.01950] [INSPIRE].

[53] A. Szabó, *Rainbow chains and numerical renormalisation group for accurate chiral conformal spectra*, *SciPost Phys.* **19** (2025) 075 [arXiv:2412.09685] [INSPIRE].

[54] R. Bonsignori and V. Eisler, *Entanglement Hamiltonian for inhomogeneous free fermions*, *J. Phys. A* **57** (2024) 275001 [arXiv:2403.14766] [INSPIRE].

[55] D. Jaksch et al., *Cold Bosonic Atoms in Optical Lattices*, *Phys. Rev. Lett.* **81** (1998) 3108 [cond-mat/9805329] [INSPIRE].

[56] M. Campostrini and E. Vicari, *Trap-size scaling in confined-particle systems at quantum transitions*, *Phys. Rev. A* **81** (2010) 023606 [arXiv:0906.2640].

[57] E. Vicari, *Entanglement and particle correlations of Fermi gases in harmonic traps*, *Phys. Rev. A* **85** (2012) 062104 [arXiv:1204.2155].

[58] V. Eisler, *Universality in the Full Counting Statistics of Trapped Fermions*, *Phys. Rev. Lett.* **111** (2013) 080402 [arXiv:1304.1413].

[59] R. Marino, S.N. Majumdar, G. Schehr and P. Vivo, *Phase Transitions and Edge Scaling of Number Variance in Gaussian Random Matrices*, *Phys. Rev. Lett.* **112** (2014) 254101 [arXiv:1404.0575].

[60] P. Calabrese, P.L. Doussal and S.N. Majumdar, *Random matrices and entanglement entropy of trapped Fermi gases*, *Phys. Rev. A* **91** (2015) 012303 [arXiv:1411.4421] [INSPIRE].

[61] E.R. Smith, *Isotropic X-Y chain in an inhomogeneous magnetic field*, *Physica* **53** (1971) 289.

[62] M. Saitoh, *Electronic states in a finite linear crystal in an electric field*, *J. Phys. C* **6** (1973) 3255.

[63] V. Eisler, F. Iglói and I. Peschel, *Entanglement in spin chains with gradients*, *J. Stat. Mech.* **2009** (2009) P02011 [arXiv:0810.3788].

[64] N. Allegra, J. Dubail, J.-M. Stéphan and J. Viti, *Inhomogeneous field theory inside the arctic circle*, *J. Stat. Mech.* **1605** (2016) 053108 [arXiv:1512.02872] [INSPIRE].

[65] J. Erdmenger, J. Kastikainen and T. Schuhmann, *Driven inhomogeneous CFT as a theory in curved space-time*, arXiv:2508.18350 [INSPIRE].

[66] H. Katsura, *Sine-square deformation of solvable spin chains and conformal field theories*, *J. Phys. A* **45** (2012) 115003 [arXiv:1110.2459] [INSPIRE].

[67] K. Okunishi, *Sine-square deformation and Möbius quantization of 2D conformal field theory*, *PTEP* **2016** (2016) 063A02 [arXiv:1603.09543] [INSPIRE].

[68] X. Wen, S. Ryu and A.W.W. Ludwig, *Evolution operators in conformal field theories and conformal mappings: Entanglement Hamiltonian, the sine-square deformation, and others*, *Phys. Rev. B* **93** (2016) 235119 [arXiv:1604.01085] [INSPIRE].

[69] P. Moosavi, *Inhomogeneous Conformal Field Theory Out of Equilibrium*, *Annales Henri Poincare* **25** (2024) 1083 [arXiv:1912.04821] [INSPIRE].

JHEP02(2026)224

[70] J. de Boer, V. Godet, J. Kastikainen and E. Keski-Vakkuri, *Quantum information geometry of driven CFTs*, *JHEP* **09** (2023) 087 [arXiv:2306.00099] [INSPIRE].

[71] J. Cardy, *The Ubiquitous 'c': from the Stefan-Boltzmann Law to Quantum Information*, *J. Stat. Mech.* **1010** (2010) P10004 [arXiv:1008.2331] [INSPIRE].

[72] H.W.J. Bloete, J.L. Cardy and M.P. Nightingale, *Conformal Invariance, the Central Charge, and Universal Finite Size Amplitudes at Criticality*, *Phys. Rev. Lett.* **56** (1986) 742 [INSPIRE].

[73] I. Affleck, *Universal Term in the Free Energy at a Critical Point and the Conformal Anomaly*, *Phys. Rev. Lett.* **56** (1986) 746 [INSPIRE].

[74] C. Dasgupta and S.-K. Ma, *Low-temperature properties of the random Heisenberg antiferromagnetic chain*, *Phys. Rev. B* **22** (1980) 1305 [INSPIRE].

[75] D.S. Fisher, *Random antiferromagnetic quantum spin chains*, *Phys. Rev. B* **50** (1994) 3799.

[76] M.B. Hastings, *An area law for one-dimensional quantum systems*, *J. Stat. Mech.* **0708** (2007) P08024 [arXiv:0705.2024] [INSPIRE].

[77] I. Peschel and M.-C. Chung, *Density matrices for a chain of oscillators*, *J. Phys. A* **32** (1999) 8419 [cond-mat/9906224] [INSPIRE].

[78] M.-C. Chung and I. Peschel, *Density-matrix spectra for two-dimensional quantum systems*, *Phys. Rev. B* **62** (2000) 4191 [cond-mat/0004222] [INSPIRE].

[79] M.-C. Chung and I. Peschel, *Density-matrix spectra of solvable fermionic systems*, *Phys. Rev. B* **64** (2001) 064412 [cond-mat/0103301] [INSPIRE].

[80] I. Peschel, *On the reduced density matrix for a chain of free electrons*, *J. Stat. Mech.* **2004** (2004) P06004 [cond-mat/0403048] [INSPIRE].

[81] S.-A. Cheong and C.L. Henley, *Many-body density matrices for free fermions*, *Phys. Rev. B* **69** (2004) 075111 [cond-mat/0206196] [INSPIRE].

[82] I. Frérot and T. Roscilde, *Area law and its violation: A microscopic inspection into the structure of entanglement and fluctuations*, *Phys. Rev. B* **92** (2015) 115129 [arXiv:1506.00545] [INSPIRE].

[83] V. Eisler and I. Peschel, *Analytical results for the entanglement Hamiltonian of a free-fermion chain*, *J. Phys. A* **50** (2017) 284003 [arXiv:1703.08126] [INSPIRE].

[84] V. Eisler and I. Peschel, *Properties of the entanglement Hamiltonian for finite free-fermion chains*, *J. Stat. Mech.* **1810** (2018) 104001 [arXiv:1805.00078] [INSPIRE].

[85] I. Affleck and A.W.W. Ludwig, *Universal noninteger 'ground state degeneracy' in critical quantum systems*, *Phys. Rev. Lett.* **67** (1991) 161 [INSPIRE].

[86] N. Laflorencie, E.S. Sørensen, M.-S. Chang and I. Affleck, *Boundary effects in the critical scaling of entanglement entropy in 1D systems*, *Phys. Rev. Lett.* **96** (2006) 100603 [cond-mat/0512475] [INSPIRE].

[87] E.S. Sørensen, N. Laflorencie and I. Affleck, *Entanglement entropy in quantum impurity systems and systems with boundaries*, *J. Phys. A* **42** (2009) 504009 [arXiv:0906.1809] [INSPIRE].

[88] L. Taddia, J.C. Xavier, F.C. Alcaraz and G. Sierra, *Entanglement entropies in conformal systems with boundaries*, *Phys. Rev. B* **88** (2013) 075112 [arXiv:1302.6222].

[89] B. Estienne, Y. Ikhlef and A. Rotaru, *Rényi entropies for one-dimensional quantum systems with mixed boundary conditions*, *SciPost Phys.* **19** (2025) 119 [arXiv:2301.02124] [INSPIRE].

JHEP02(2026)224

[90] B.-Q. Jin and V.E. Korepin, *Quantum Spin Chain, Toeplitz Determinants and the Fisher — Hartwig Conjecture*, *J. Statist. Phys.* **116** (2004) 79 [quant-ph/0304108] [INSPIRE].

[91] J.P. Keating and F. Mezzadri, *Random Matrix Theory and Entanglement in Quantum Spin Chains*, *Commun. Math. Phys.* **252** (2004) 543 [quant-ph/0407047] [INSPIRE].

[92] P. Calabrese and F.H.L. Essler, *Universal corrections to scaling for block entanglement in spin-1/2 XX chains*, arXiv:1006.3420 [DOI:10.1088/1742-5468/2010/08/P08029] [INSPIRE].

[93] M. Fagotti and P. Calabrese, *Universal parity effects in the entanglement entropy of XX chains with open boundary conditions*, *J. Stat. Mech.* **1101** (2011) P01017 [arXiv:1010.5796] [INSPIRE].

[94] M. Gruber and V. Eisler, *Magnetization and entanglement after a geometric quench in the XXZ chain*, *Phys. Rev. B* **99** (2019) 174403 [arXiv:1902.05834] [INSPIRE].

[95] V. Eisler and F. Maislinger, *Front dynamics in the XY chain after local excitations*, *SciPost Phys.* **8** (2020) 037 [arXiv:1909.02841] [INSPIRE].

[96] M. Gruber and V. Eisler, *Time evolution of entanglement negativity across a defect*, *J. Phys. A* **53** (2020) 205301 [arXiv:2001.06274] [INSPIRE].

[97] V. Eisler, *Entanglement spreading after local and extended excitations in a free-fermion chain*, *J. Phys. A* **54** (2021) 424002 [arXiv:2106.16105] [INSPIRE].

[98] L. Capizzi and V. Eisler, *Entanglement evolution after a global quench across a conformal defect*, *SciPost Phys.* **14** (2023) 070 [arXiv:2209.03297] [INSPIRE].

[99] V. Eisler, *Entanglement negativity in a nonequilibrium steady state*, *Phys. Rev. B* **107** (2023) 075157 [arXiv:2212.08499] [INSPIRE].

[100] V. Eisler, *Entanglement Hamiltonian of a nonrelativistic Fermi gas*, *Phys. Rev. B* **109** (2024) L201113 [arXiv:2311.16348] [INSPIRE].

[101] V. Eisler, *On the Bisognano-Wichmann entanglement Hamiltonian of nonrelativistic fermions*, *J. Stat. Mech.* **2025** (2025) 013101 [arXiv:2410.16433] [INSPIRE].

[102] P.-A. Bernard et al., *Entanglement Hamiltonian and orthogonal polynomials*, *Nucl. Phys. B* **1020** (2025) 117185 [arXiv:2412.12021] [INSPIRE].

[103] N. Crampé, R.I. Nepomechie and L. Vinet, *Free-Fermion entanglement and orthogonal polynomials*, *J. Stat. Mech.* **1909** (2019) 093101 [arXiv:1907.00044] [INSPIRE].

[104] F. Finkel and A. González-López, *Inhomogeneous XX spin chains and quasi-exactly solvable models*, *J. Stat. Mech.* **2009** (2020) 093105 [arXiv:2007.00369] [INSPIRE].

[105] F. Finkel and A. González-López, *Entanglement entropy of inhomogeneous XX spin chains with algebraic interactions*, *JHEP* **12** (2021) 184 [arXiv:2107.12200] [INSPIRE].

[106] N. Crampé, R.I. Nepomechie and L. Vinet, *Entanglement in fermionic chains and bispectrality*, *Rev. Math. Phys.* **33** (2021) 2140001 [arXiv:2001.10576].

[107] P.-A. Bernard et al., *Entanglement of inhomogeneous free fermions on hyperplane lattices*, *Nucl. Phys. B* **984** (2022) 115975 [arXiv:2206.06509] [INSPIRE].

[108] P.-A. Bernard et al., *Entanglement of free-fermion systems, signal processing and algebraic combinatorics*, arXiv:2401.07150 [INSPIRE].

[109] G. Blanchet, G. Parez and L. Vinet, *Fermionic logarithmic negativity in the Krawtchouk chain*, *J. Stat. Mech.* **2024** (2024) 113101 [arXiv:2408.16531] [INSPIRE].

JHEP02(2026)224

[110] P.-A. Bernard, G. Parez and L. Vinet, *Distinctive features of inhomogeneous spin chains*, in the proceedings of the *33rd/35th International Colloquium on Group Theoretical Methods in Physics*, Cotonou, Benin, July 15–19 (2024) [arXiv:2411.09487] [INSPIRE].

[111] P.-A. Bernard et al., *Entanglement of inhomogeneous free bosons and orthogonal polynomials*, *J. Phys. A* **58** (2025) 305001 [arXiv:2505.15610] [INSPIRE].

[112] J. Dubail, J.-M. Stéphan and P. Calabrese, *Emergence of curved light-cones in a class of inhomogeneous Luttinger liquids*, *SciPost Phys.* **3** (2017) 019 [arXiv:1705.00679] [INSPIRE].

[113] Y. Brun and J. Dubail, *One-particle density matrix of trapped one-dimensional impenetrable bosons from conformal invariance*, *SciPost Phys.* **2** (2017) 012 [arXiv:1701.02248] [INSPIRE].

[114] Y. Brun and J. Dubail, *The Inhomogeneous Gaussian Free Field, with application to ground state correlations of trapped 1d Bose gases*, *SciPost Phys.* **4** (2018) 037 [arXiv:1712.05262].

[115] A. Bastianello, J. Dubail and J.-M. Stéphan, *Entanglement entropies of inhomogeneous Luttinger liquids*, *J. Phys. A* **53** (2020) 155001 [arXiv:1910.09967] [INSPIRE].

[116] V. Eisler, G. Di Giulio, E. Tonni and I. Peschel, *Entanglement Hamiltonians for non-critical quantum chains*, *J. Stat. Mech.* **2010** (2020) 103102 [arXiv:2007.01804] [INSPIRE].

[117] H. Bostelmann, D. Cadamuro and C. Minz, *On the Mass Dependence of the Modular Operator for a Double Cone*, *Annales Henri Poincare* **24** (2023) 3031 [arXiv:2209.04681] [INSPIRE].

[118] M.A. Baranov, *Reduced density matrix and entanglement Hamiltonian for a free real scalar field on an interval*, arXiv:2412.13777 [INSPIRE].

[119] F. Gentile, A. Rotaru and E. Tonni, *Entanglement Hamiltonian of two disjoint blocks in the harmonic chain*, *J. Stat. Mech.* **2025** (2025) 073102 [arXiv:2503.19644] [INSPIRE].

[120] F. Rottoli, S. Murciano, E. Tonni and P. Calabrese, *Entanglement and negativity Hamiltonians for the massless Dirac field on the half line*, *J. Stat. Mech.* **2301** (2023) 013103 [arXiv:2210.12109] [INSPIRE].

[121] F. Parisen Toldin and F.F. Assaad, *Entanglement Hamiltonian of Interacting Fermionic Models*, *Phys. Rev. Lett.* **121** (2018) 200602 [arXiv:1804.03163] [INSPIRE].

[122] A.M. Läuchli, *Operator content of real-space entanglement spectra at conformal critical points*, arXiv:1303.0741 [INSPIRE].

[123] D. Poilblanc, *Entanglement spectra of quantum Heisenberg ladders*, *Phys. Rev. Lett.* **105** (2010) 077202 [arXiv:1005.2123] [INSPIRE].

[124] A.M. Läuchli and J. Schliemann, *Entanglement spectra of coupled S=1/2 spin chains in a ladder geometry*, *Phys. Rev. B* **85** (2012) 054403 [arXiv:1106.3419] [INSPIRE].

[125] J. Schliemann and A.M. Läuchli, *Entanglement Spectra of Heisenberg Ladders of higher Spin*, arXiv:1205.0109 [DOI:10.1088/1742-5468/2012/11/P11021] [INSPIRE].

[126] P. Calabrese and A. Lefevre, *Entanglement spectrum in one-dimensional systems*, *Phys. Rev. A* **78** (2008) 032329 [arXiv:0806.3059] [INSPIRE].

[127] V. Alba, P. Calabrese and E. Tonni, *Entanglement spectrum degeneracy and the Cardy formula in 1+1 dimensional conformal field theories*, *J. Phys. A* **51** (2018) 024001 [arXiv:1707.07532] [INSPIRE].

[128] J. Surace, L. Tagliacozzo and E. Tonni, *Operator content of entanglement spectra in the transverse field Ising chain after global quenches*, *Phys. Rev. B* **101** (2020) 241107(R) [arXiv:1909.07381] [INSPIRE].

JHEP02(2026)224

[129] A. Peres, *Separability criterion for density matrices*, *Phys. Rev. Lett.* **77** (1996) 1413 [quant-ph/9604005] [INSPIRE].

[130] G. Vidal and R.F. Werner, *Computable measure of entanglement*, *Phys. Rev. A* **65** (2002) 032314 [quant-ph/0102117] [INSPIRE].

[131] M.B. Plenio, *Logarithmic Negativity: A Full Entanglement Monotone That is not Convex*, *Phys. Rev. Lett.* **95** (2005) 090503 [quant-ph/0505071] [INSPIRE].

[132] P. Calabrese, J. Cardy and E. Tonni, *Entanglement negativity in quantum field theory*, *Phys. Rev. Lett.* **109** (2012) 130502 [arXiv:1206.3092] [INSPIRE].

[133] P. Calabrese, J. Cardy and E. Tonni, *Entanglement negativity in extended systems: A field theoretical approach*, *J. Stat. Mech.* **1302** (2013) P02008 [arXiv:1210.5359] [INSPIRE].

[134] P. Calabrese, J. Cardy and E. Tonni, *Finite temperature entanglement negativity in conformal field theory*, *J. Phys. A* **48** (2015) 015006 [arXiv:1408.3043] [INSPIRE].

[135] P. Calabrese, L. Tagliacozzo and E. Tonni, *Entanglement negativity in the critical Ising chain*, *J. Stat. Mech.* **1305** (2013) P05002 [arXiv:1302.1113] [INSPIRE].

[136] V. Eisler and Z. Zimborás, *On the partial transpose of fermionic Gaussian states*, *New J. Phys.* **17** (2015) 053048 [arXiv:1502.01369] [INSPIRE].

[137] A. Coser, E. Tonni and P. Calabrese, *Towards the entanglement negativity of two disjoint intervals for a one dimensional free fermion*, *J. Stat. Mech.* **1603** (2016) 033116 [arXiv:1508.00811] [INSPIRE].

[138] A. Coser, E. Tonni and P. Calabrese, *Partial transpose of two disjoint blocks in XY spin chains*, *J. Stat. Mech.* **1508** (2015) P08005 [arXiv:1503.09114] [INSPIRE].

[139] H. Shapourian, K. Shiozaki and S. Ryu, *Partial time-reversal transformation and entanglement negativity in fermionic systems*, *Phys. Rev. B* **95** (2017) 165101 [arXiv:1611.07536] [INSPIRE].

[140] V. Eisler and Z. Zimborás, *Entanglement negativity in two-dimensional free lattice models*, *Phys. Rev. B* **93** (2016) 115148 [arXiv:1511.08819] [INSPIRE].

[141] C. De Nobili, A. Coser and E. Tonni, *Entanglement negativity in a two dimensional harmonic lattice: Area law and corner contributions*, *J. Stat. Mech.* **1608** (2016) 083102 [arXiv:1604.02609] [INSPIRE].

[142] B. Mula et al., *Ergotropy and entanglement in critical spin chains*, *Phys. Rev. B* **107** (2023) 075116 [arXiv:2207.13998] [INSPIRE].

[143] C.M. Langlett et al., *Rainbow scars: From area to volume law*, *Phys. Rev. B* **105** (2022) L060301 [arXiv:2107.03416] [INSPIRE].

[144] S. Singha Roy, S.N. Santalla, J. Rodríguez-Laguna and G. Sierra, *Entanglement as geometry and flow*, *Phys. Rev. B* **101** (2020) 195134 [arXiv:1906.05146] [INSPIRE].

[145] M. Caraglio and F. Gliozzi, *Entanglement Entropy and Twist Fields*, *JHEP* **11** (2008) 076 [arXiv:0808.4094] [INSPIRE].

[146] S. Furukawa, V. Pasquier and J. Shiraishi, *Mutual Information and Compactification Radius in a c=1 Critical Phase in One Dimension*, *Phys. Rev. Lett.* **102** (2009) 170602 [arXiv:0809.5113] [INSPIRE].

[147] P. Calabrese, J. Cardy and E. Tonni, *Entanglement entropy of two disjoint intervals in conformal field theory*, *J. Stat. Mech.* **0911** (2009) P11001 [arXiv:0905.2069] [INSPIRE].

JHEP02(2026)224

[148] P. Calabrese, J. Cardy and E. Tonni, *Entanglement entropy of two disjoint intervals in conformal field theory II*, *J. Stat. Mech.* **1101** (2011) P01021 [arXiv:1011.5482] [INSPIRE].

[149] A. Coser, L. Tagliacozzo and E. Tonni, *On Rényi entropies of disjoint intervals in conformal field theory*, *J. Stat. Mech.* **1401** (2014) P01008 [arXiv:1309.2189] [INSPIRE].

[150] T. Grava, A.P. Kels and E. Tonni, *Entanglement of Two Disjoint Intervals in Conformal Field Theory and the 2D Coulomb Gas on a Lattice*, *Phys. Rev. Lett.* **127** (2021) 141605 [arXiv:2104.06994] [INSPIRE].

[151] C.A. Agón, M. Headrick, D.L. Jafferis and S. Kasko, *Disk entanglement entropy for a Maxwell field*, *Phys. Rev. D* **89** (2014) 025018 [arXiv:1310.4886] [INSPIRE].

[152] C. De Nobili, A. Coser and E. Tonni, *Entanglement entropy and negativity of disjoint intervals in CFT: Some numerical extrapolations*, *J. Stat. Mech.* **1506** (2015) P06021 [arXiv:1501.04311] [INSPIRE].

[153] N. Javerzat and E. Tonni, *On the continuum limit of the entanglement Hamiltonian of a sphere for the free massless scalar field*, *JHEP* **02** (2022) 086 [arXiv:2111.05154] [INSPIRE].

[154] M. Huerta and G. van der Velde, *Modular Hamiltonian of the scalar in the semi infinite line: dimensional reduction for spherically symmetric regions*, *JHEP* **06** (2023) 097 [arXiv:2301.00294] [INSPIRE].

[155] M. Huerta and G. van der Velde, *Modular Hamiltonian in the semi infinite line. Part II. Dimensional reduction of Dirac fermions in spherically symmetric regions*, *JHEP* **01** (2024) 062 [arXiv:2307.08755] [INSPIRE].

[156] P.-A. Bernard, Z. Mann, G. Parez and L. Vinet, *Absence of logarithmic enhancement in the entanglement scaling of free fermions on folded cubes*, *J. Phys. A* **57** (2024) 015002 [arXiv:2307.03345] [INSPIRE].

[157] N.S.S. de Buruaga, S.N. Santalla, G. Sierra and J. Rodríguez-Laguna, *Entanglement Halos*, arXiv:2507.20430 [INSPIRE].

[158] X. Wen, S. Ryu and A.W.W. Ludwig, *Entanglement hamiltonian evolution during thermalization in conformal field theory*, *J. Stat. Mech.* **1811** (2018) 113103 [arXiv:1807.04440] [INSPIRE].

[159] X. Wen and J.-Q. Wu, *Quantum dynamics in sine-square deformed conformal field theory: Quench from uniform to nonuniform conformal field theory*, *Phys. Rev. B* **97** (2018) 184309 [arXiv:1802.07765] [INSPIRE].

[160] X. Wen and J.-Q. Wu, *Floquet conformal field theory*, arXiv:1805.00031 [INSPIRE].

[161] G. Di Giulio, R. Arias and E. Tonni, *Entanglement hamiltonians in 1D free lattice models after a global quantum quench*, *J. Stat. Mech.* **1912** (2019) 123103 [arXiv:1905.01144] [INSPIRE].

[162] B. Han and X. Wen, *Classification of SL_2 deformed Floquet conformal field theories*, *Phys. Rev. B* **102** (2020) 205125 [arXiv:2008.01123] [INSPIRE].

[163] F. Rottoli, S. Scopa and P. Calabrese, *Entanglement Hamiltonian during a domain wall melting in the free Fermi chain*, *J. Stat. Mech.* **2206** (2022) 063103 [arXiv:2202.04380] [INSPIRE].

[164] R. Bonsignori and V. Eisler, *Entanglement Hamiltonian after a local quench*, arXiv:2508.19406 [INSPIRE].

[165] S. Ryu and T. Takayanagi, *Holographic derivation of entanglement entropy from AdS/CFT*, *Phys. Rev. Lett.* **96** (2006) 181602 [hep-th/0603001] [INSPIRE].

JHEP02(2026)224

[166] S. Ryu and T. Takayanagi, *Aspects of Holographic Entanglement Entropy*, *JHEP* **08** (2006) 045 [hep-th/0605073] [INSPIRE].

[167] V.E. Hubeny, M. Rangamani and T. Takayanagi, *A covariant holographic entanglement entropy proposal*, *JHEP* **07** (2007) 062 [arXiv:0705.0016] [INSPIRE].

[168] M. Freedman and M. Headrick, *Bit threads and holographic entanglement*, *Commun. Math. Phys.* **352** (2017) 407 [arXiv:1604.00354] [INSPIRE].

[169] C.A. Agón, J. De Boer and J.F. Pedraza, *Geometric Aspects of Holographic Bit Threads*, *JHEP* **05** (2019) 075 [arXiv:1811.08879] [INSPIRE].

[170] I. MacCormack, A. Liu, M. Nozaki and S. Ryu, *Holographic Duals of Inhomogeneous Systems: The Rainbow Chain and the Sine-Square Deformation Model*, *J. Phys. A* **52** (2019) 505401 [arXiv:1812.10023] [INSPIRE].

[171] E. Tonni, *Entanglement Hamiltonians and contours in a segment*, talk at the *It from Qubit workshop*, Centro Atómico Bariloche, Argentina, January 3 (2018).

[172] J. Kudler-Flam, I. MacCormack and S. Ryu, *Holographic entanglement contour, bit threads, and the entanglement tsunami*, *J. Phys. A* **52** (2019) 325401 [arXiv:1902.04654] [INSPIRE].

[173] M. Mintchev and E. Tonni, *Modular conjugations in 2D conformal field theory and holographic bit threads*, *JHEP* **12** (2022) 149 [arXiv:2209.03242] [INSPIRE].

[174] S. Caggioli, F. Gentile, D. Seminara and E. Tonni, *Holographic thermal entropy from geodesic bit threads*, *JHEP* **07** (2024) 088 [arXiv:2403.03930] [INSPIRE].

JHEP02(2026)224